Advanced Functionalities for Highly Reliable Optical Networks

An, Yi

Publication date:
2013

Document Version
Publisher's PDF, also known as Version of record

Advanced Functionalities for Highly Reliable Optical Networks

Ph.D. Thesis
Yi An

2012-12-31

Department of Photonics Engineering
Technical University of Denmark
Building 343
2800 Kgs. Lyngby
DENMARK

To my beloved family

Il y a un spectacle plus grand que la mer, c'est le ciel; il y a un spectacle plus grand que le ciel, c'est l'intérieur de l'âme.

A spectacle greater than the ocean, it's the sky; a spectacle greater than the sky, it's the man's heart.

— "*Les Misérables*", **Victor Hugo** (1802-1885)

Abstract

This thesis covers two research topics concerning optical solutions for networks e.g. avionic systems. One is to identify the applications for silicon photonic devices for cost-effective solutions in short-range optical networks. The other one is to realise advanced functionalities in order to increase the availability of highly reliable optical networks.

A cost-effective transmitter based on a directly modulated laser (DML) using a silicon micro-ring resonator (MRR) to enhance its modulation speed is proposed, analysed and experimentally demonstrated. A modulation speed enhancement from 10 Gbit/s to 40 Gbit/s in a directly modulated distributed feed-back (DFB) laser diode is achieved by using the proposed scheme. Enhancement is also achieved in vertical-cavity surface-emitting lasers (VCSELs). The cascadability of silicon MRRs is experimentally assessed as well for their applications in optical interconnects and network-on-chips.

A novel concept of all-optical protection switching scheme is proposed, where fault detection and protection trigger are all implemented in the optical domain. This scheme can provide ultra-fast establishment of the protection path resulting in a minimum loss of data. It is experimentally demonstrated by using a bistable modulated grating Y-branch (MG-Y) laser structure. The achieved protection switching time is less than 200 ps and the signal switched by the fast establishment of the protection path has good quality at both 10 Gbit/s and 40 Gbit/s. The optically controlled bistable operation of the MG-Y laser with wide wavelength tunable range is also experimentally demonstrated within this thesis. Another protection method using network coding is also introduced. All-optical network coding for phase modulated signals (e.g. differential phase shift keying (DPSK) signals) using two exclusive

OR (XOR) gates realised by four-wave mixing (FWM) in semiconductor optical amplifiers (SOAs) is experimentally demonstrated and very low ($\sim$ 1 dB) total operation penalty is achieved.

Resumé

Denne afhandling behandler to felter indenfor optiske løsninger til netværk i f.eks. luftfartøjer. Det ene felt er fokuseret på at afdække hvilke applikationer der med fordel kan benytte silicium fotoniske komponenter til kost effektive løsninger i netværk med lille rækkevidde. Det andet felt fokuserer på at implementere avancerede løsninger som vil kunne højne driftssikkerheden og dermed brugbarheden af optiske netværk.

En kost effektiv sender baseret på en direkte moduleret laser (DML) kombineret med en silicium mikrorings resonator (MRR) er foreslået, analyseret samt eksperimentelt testet. En forbedring af modulationshastigheden fra 10 Gbit/s til 40 Gbit/s for en direkte moduleret distributed feed-back (DFB) laser blev opnået ved hjælp af det foreslåede princip. Forbedring i modulationshastigheden blev også opnået i vertical-cavity surface-emitting lasers (VCSELs). Kaskadekoblede silicium MRRer blev desuden eksperimentelt evalueret for deres brugbarhed i kontekst af optiske interconnects samt chip integrerede netværk.

Et nyt koncept til fuldstændig optisk beskyttelses kredsløb er foreslået og er baseret på fejl-detektion og kredsløbs skift for beskyttelse udelukkende implementeret i det optiske domæne. Princippet danner en beskyttelses rute ultra-hurtigt hvilket resulterer i et minimum tab af data. Dette er eksperimentelt demonstreret ved benyttelse af en bi-stabil moduleret gitter Y-formet (MG-Y) laser struktur. Den opnåede skifte-tid er mindre end 200 ps og signal kvaliteten af det kredsløbs skiftede signal er høj, både for 10 og 40 Gbit/s. Den optisk kontrollerede bi-stabile operation af MG-Y laseren har et stort bølgelængde operations område hvilket er eksperimentelt demonstreret i denne afhandling. Yderlig en beskyttelses teknik baseret på netværks kodning er introduceret. Netværks kodning baseret på ren optisk modulation af fase modulerede signaler

(f.eks. differentiel fase skiftet kode (DPSK)) ved at benytte to eksklusive OR (XOR) kredsløb implementeret vha. firbølge blanding (FWM) i en halvleder optisk forstærker (SOA) er eksperimentelt eftervist og særdeles lav ($\sim$ 1 dB) forværring af den samlede operations ydeevne er opnået.

Acknowledgements

I would like to acknowledge the DAPHNE (**D**eveloping **A**ircraft **Ph**otonic **Ne**twork) project (Ref. 233709) funded by the 7^{th} framework programme of the European Commission for supporting my Ph.D. study. I would thank my supervisors, Anders Clausen and Michael S. Berger, for giving me the opportunity to pursue my Ph.D at the Technical University of Denmark.

During this project, many of the results would never be obtained without the excellent collaboration and numerous help from other Universities. I would like to express my sincere thanks to Prof. G. Morthier from the Department of Information Technology at Ghent University, Belgium for providing the MG-Y laser samples. Thank you for sharing your knowledge. I would like to thank Prof. M. C. Amann, Dr. M. Müller and Ms. S. Spiga at Walter Schottky Institut of Technische Universität München (TUM), Germany, for providing the VCSEL samples. Thank you very much for helping me along.

I am very grateful to my former and current colleagues: Jiang Zhang, Abel Lorences Riesgo, Oskars Ozolins (Technical University of Riga), Jorge Seoane, Christophe Peucheret, Francesco Da Ros, Zohreh Lali-Dastjerdi, Dragana Vukovic, Jose Manuel Estaran Tolosa, Yunhong Ding, Meng Xiong and Bo Huang for many collaborative work and all the help that I received from them. I also would like to thank all the members of the High-Speed Optical Communications (HSOC) Group for the enjoyable atmosphere. It was a privilege to have worked with you.

Last but not the least, I would like to thank my family for their persistent love, support and encouragement.

Yi An
Copenhagen, 2012

Ph.D. Publications

The following publications have resulted from this Ph.D. project.

A. J. Zhang, Y. An, M. S. Berger, C. Peucheret and A. T. Clausen, "Developing A Generic Optical Avionic Network", *18th International Conference on Telecommunications, ICT'11*, Ayia Napa, Cyprus, May 2011, pp. 278-283.

B. J. Zhang, Y. An, M. S. Berger, and A. T. Clausen, "Wavelength and Fiber Assignment Problems on Avionic Networks", *IEEE Avionics, Fiber-Optics and Photonics Technology Conference, AVFOP'11*, San Diego, USA, October 2011, paper TuB4, pp. 15-16.

C. Y. An, A. Lorences Riesgo, J. Seoane, Y. Ding, H. Ou, and C. Peucheret, "Modulation Speed Enhancement of Directly Modulated Lasers Using a Micro-ring Resonator", *IEEE Optical Interconnects Conference, OIC'12*, Santa Fe, New Mexico, USA, May 20-23, 2012, paper TuB2, pp. 32-33.

D. M. Xiong, O. Ozolins, Y. Ding, B. Huang, Y. An, H. Ou, C. Peucheret and X. Zhang, "41.6 Gb/s RZ-DPSK to NRZ-DPSK Format Conversion in a Microring Resonator", *17th OptoElectronics and Communications Conference, OECC'12*, Busan, S. Korea, July 2-6, 2012, paper 6F1-1, pp. 891-892.

E. Y. An, A. Lorences Riesgo, J. Seoane, Y. Ding, H. Ou, and C. Peucheret, "Transmission Property of Directly Modulated Signals Enhanced by a Micro-ring Resonator", *17th OptoElectronics and Communications Conference, OECC'12*, Busan, S. Korea, July 2-6, 2012, paper 6F3-3, pp. 915-916.

F. Y. An, A. Lorences Riesgo, C. Peucheret and G. Morthier, "Wavelength Tunable Flip-Flop Operation of a Modulated Grating Y-branch Laser", *Photonics in Switching Conference, PS'12*, Ajaccio, Corsica, France, September 11-14, 2012, paper Fr-S18-O21.

G. Z. Lali-Dastjerdi, O. Ozolins, Y. An, V. Cristofori, F. Da Ros, N. Kang, H. Hu; H. C. Mulvad, K. Rottwitt, M. Galili and C. Peucheret, "Demonstration of Cascaded In-Line Single-Pump Fiber Optical Parametric Amplifiers in Recirculating Loop Transmission", *38th European Conference on Optical Communication, ECOC'12*, Amsterdam, Netherland, September 16-20, 2012, paper Mo.2.C.5.

H. C. Peucheret, Y. Ding, H. Ou, M. Xiong, Y. An, A. Lorences Riesgo, J. Xu, O. Ozolins, H. Hu, M. Galili, B. Huang, M. Pu, H. Ji, J. Seoane, L. Liu and X. Zhang, "Linear Signal Processing Using Silicon Micro-Ring Resonators", *Conference on Information Optoelectronics, Nanofabrication and Testing, IONT'12*, Wuhan, China, November 01-02, 2012, paper ITh5B.1, *Invited.*

I. O. Ozolins, Y. An, Z. Lali-Dastjerdi, V. Bobrovs, G. Ivanovs and C. Peucheret, "Cascadability of Silicon Microring Resonators for 40-Gbit/s OOK and DPSK Optical Signals", *Asia Communications and Photonics Conference, ACP'12*, Guangzhou, China, November 7-10, 2012, paper AS1G.1.

J. M. Xiong, O. Ozolins, Y. Ding, B. Huang, Y. An, H. Ou, C. Peucheret and X. Zhang, "Simultaneous RZ-OOK to NRZ-OOK and RZ-DPSK to NRZ-DPSK Format Conversion in a Silicon Microring Resonator", *Optics Express*, vol. 20, no. 25, pp. 27263-27272, 2012.

K. Y. An, F. Da Ros and C. Peucheret, "All-Optical Network Coding for DPSK Signals", *Optical Fiber Communication Conference, OFC/NFOEC'13*, Anaheim, California, USA, March 17-21, 2013, paper JW2A.60.

L. B. Huang, Y. An, N. Chi, M. Xiong, H. Ou, W. Liu and C. Peucheret, "Combining DPSK and duobinary for the downstream in 40-Gb/s long-reach WDM-PONs", accepted for publication in *Fiber Optical Technology*

M. Y. An, D. Vukovic, A. Lorences Riesgo, G. Mortier and C. Peucheret,

"Ultra-fast all-optical self-aware protection switching based on a bistable laser diode", submitted to *IEEE Photonic Technology Letter*.

N. A. Lorences Riesgo, Y. An, J. Seoane, Y. Ding, H. Ou, and C. Peucheret, "Demonstration and Optimization of Micro-ring Resonator-assisted High-speed Directly Modulated Lasers", submitted to *Journal of Lightwave Technology*.

O. Y. An, F. Da Ros and C. Peucheret, "All-optical Network Coding for Phase Modulated Signals", to be submitted

P. Y. An, M. Müller, J. Estaran, S. Spiga, M. Amann and C. Peucheret, "Modulation Speed Enhancement of VCSELs Using Optical Filtering", to be submitted

Contents

Chapter 1

Introduction

1.1 Overview and Objectives

Each communication network has its very own characteristics, which are imposed by user applications and requirements. These requirements on the services provided by the network are in terms of delay, reliability, accuracy, bandwidth and, of course, cost [1].

While implementing a service or designing a network, a successful technical solution will be the one which satisfies the most factors among: technology availability, requirements, cost, regulations, market, compatibility with legacy system and etc. From a technical point of view, three of them are the most important conditions which must be satisfied, in order to find out a solution, as shown as in Fig. 1.1.

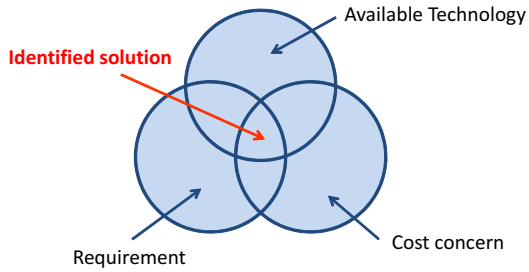

Figure 1.1: Factors for identification of a solution for implementing a service or designing a network.

This Ph.D. study is part of a three-year project called **D**eveloping **A**ircraft **Ph**otonic **Ne**twork (DAPHNE), which is carried out during 09.2009 to 02.2013 and was funded by the 7^{th} framework programme of the European Commission (Ref. 233709). The objective of the European project is to look for the solutions for the next generation of avionic networks on aircrafts [2]. As more and more subsystems and functionalities are added into the avionic networks, the weight, size and energy consumption are increasing continuously. Fibre optical and photonic technologies offer obvious advantages in size, weight, bandwidth and electromagnetic compatibility (EMC), beyond aircraft systems state-of-the-art. Therefore, they are believed to be the future solutions for the next generation of avionics systems.

In terms of requirement, avionic systems have all the characteristics of any ordinary communication networks. Among them, however, network reliability or service availability, without any doubt, is the most important factor. In terms of cost-effectiveness, the identified solution would be better if it can be generalised and used for other networks. As the sizes of avionic systems are short, their technical solutions should also be addressed for all the networks which have similar requirements, i.e. short-range and highly reliable optical networks.

Two research topics were therefore identified within this Ph.D. project:

1. Cost-effective and integratied optical components for short-range optical networks.
2. All-optical network protection methods for highly-reliable optical networks.

1.1.1 Cost-effective and integrative optical components

Silicon photonics has attracted many research attentions thanks to its compatibility with complementary metal-oxide-semiconductor (CMOS) fabrication for massive production and hence can be with low cost. Silicon photonic devices are compact and suitable for high density integration. Therefore they are promising for optical interconnects, network-on-chips, cost-effective telecommunications and they also find their position in varieties of optical sensor areas [3]. In the telecom area, transmitters, modulators, photodetectors and other kinds of basic components based

on silicon photonics are under development and still with tremendous interests.

We are in particular interested in silicon micro-ring resonators (MRRs), as they have great potentials in laser design [4–6], for optical interconnect and network-on-chips [7–11], in modulators [12–14] and in optical switches [15–17]. In this project, we will address some practical issue, e.g. cascadability, and search for their potentials in other applications.

1.1.2 All-optical network protection

As most deployed optical links already carry capacities in excess of 10 Gbit/s, any outage in even just a few milliseconds will cause the loss of tens of megabytes of data, far beyond the tolerance of any reliable networks. Providing resilience against failures is therefore an important requirement.

The only practical way of obtaining very high availability of a connection is to make the network survivable, which is to be able to continue providing services even when failures happen [18]. Protection switching is a key technique to ensure survivability against outages in optical networks by providing some redundant capacity within the network and automatically rerouting traffic around the failure using this redundant capacity [18]. Protection is usually implemented in a localised manner without requiring a central overview of the network status, in contrast to a related term, restoration, which re-distributes the traffic over the current network. Protection is, thus, much faster than restoration.

Fibre cuts is the most likely failure event, which causes link failures. Two fundamental types of protection mechanisms can be summarised as 1+1 protection and 1:1 protection, as shown in Fig. 1.2. In 1+1 protection, the traffic is transmitted simultaneously on two separate paths from the source to the destination, while in 1:1 protection (can also be in a more generalised case 1:N protection), there are still two paths between the source and the destination. However, the traffic is transmitted over only one path at a time, say, the working path. If the link fails due to e.g. fibre-cut, both the source and destination switch operation onto the backup path.

The 1+1 protection is simple and reliable, which is very often used for highly reliable networks [19]. Compared to 1+1 protection, the 1:1

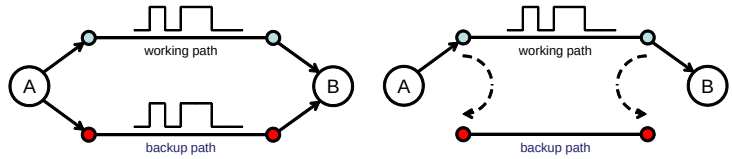

Figure 1.2: 2 types of protection techniques (a) 1+1 protection and (b) 1:1 protection.

protection is more energy-friendly, but requires more complex control system: fault detection, acknowledgement and protection switching trigger. Within this project, we propose and demonstrate a novel concept of all-optical 1:1 protection switching where link failure detection and protection trigger both implemented on the optical layer. Because of the simplicity of 1+1 protection, it is important to also address it for all-optical protection. Network coding was proposed to increase the through put of multicasting networks [20]. It can also be used for network protection [21, 22] by having a copy of the data surviving somewhere in the network under the form of a code generated together with other data to the same destination. Any lost data can therefore be recovered from the code and the successfully delivered data. We addressed the all-optical network coding for phase modulated signals within this project.

1.2 Contributions of this Ph.D. Thesis

The following describes the main results and contributions achieved during this Ph.D. project, listed in the same order as the chapters in which they appear:

- Linear signal processing using silicon micro-ring resonators:
  - Cascadability of silicon MRRs for optical interconnects and network-on-chips [publication I].
  - Cost-effective high-speed directly modulated transmitter design by using a silicon MRR [C, E, N, P].
- Wavelength tunable all-optical wavelength flip-flop (AOWFF) using a single laser structure [F].

- Design and demonstration of all-optical protection scheme for highly reliable optical networks:
  - Novel concept on ultra-fast self-aware all-optical protection switching and experimental demonstration using a single bistable laser structure [M].
  - All-optical protection scheme using all-optical network coding (AONC) for phase modulated signals [K,O].

1.3 Structure of The Thesis

This thesis can be divided into two parts. The first part, including Chapter 2 and Chapter 3, concerns the use of silicon MRRs for short-range networks. The other part concerns the functionalities realised by all-optical techniques in order to increase the availability of optical networks, including Chapter 4 and Chapter 5.

In Chapter 2, numerical models for silicon MRRs with different configurations, together with their amplitude response and dispersion profiles are presented. The cascadability of silicon MRRs used as band-pass filters is experimentally investigated and presented.

A cost-effective transmitter design using a silicon MRR is proposed and comprehensively analysed in Chapter 3. The enhancement on the modulation speed of a directly modulated laser (DML) is numerically analysed and demonstrated in both distributed feed-back (DFB) laser diode and vertical-cavity surface-emitting laser (VCSEL).

Chapter 4 presents a novel concept of all-optical protection switching, where link failure detection and protection trigger are both implemented on the optical layer without the need for upper-layer mechanism. This concept is experimentally demonstrated using a wavelength tunable AOWFF based on a single modulated grating Y-branch (MG-Y) laser structure. The principle and the first experimental demonstration of the flip-flop operation with large wavelength tunable range in a MG-Y laser structure is also presented.

In Chapter 5, all-optical network protection based on network coding is presented. The scheme is experimentally demonstrated for 10 Gbit/s differential phase shift keying (DPSK) signals. The feasibility of multi-

casting the optical network coding and coding implementation for advanced phase modulated signals are discussed.

Finally in Chapter 6 the project will be summarised and an outlook of future work will be given.

Chapter 2

Silicon Micro-Ring Resonators

2.1 Introduction

The silicon-on-insulator (SOI) technology offers the possibility to fabricate waveguides with high-index-contrast between the core and cladding, therefore allowing bending radii on the order of micrometres and enabling high-density integration of photonic devices. In addition, nano-photonic devices based on SOI can be implemented uing the complementary metal-oxide-semiconductor (CMOS) platform, which makes it an attractive solution for integrating photonic components with conventional microelectronic processing. These advantages in fabrication technologies and application-driven demands in telecommunications triggered the rapid development of nano-photonic devices.

Among silicon photonic components, silicon micro-ring resonators (MRRs), are versatile devices with promising applications as optical filters or wavelength selective switches [23]. One straightforward use of MRRs is as optical add-drop multiplexers in wavelength division multiplexing (WDM) systems. Furthermore, thanks to their compactness, integrability, and compatibility with standard microelectronic fabrication processes, they are essential building blocks for future scalable optical interconnect architectures [11], which have recently been the object of increased research interest.

In this chapter, we numerically analyse different configuration of MRRs and compare their transfer function and amplitude-phase relation. Meanwhile, as MRRs have a great potential for high density integration for optical interconnect and on-chip network, cascading them cannot be avoided therefore need to be assessed. We experimentally assess the cascadability of MRRs as drop filters with 40 Gbit/s carrier-suppressed return-to-zero on-off keying (CSRZ-OOK) and carrier-suppressed return-to-zero differential phase shift keying (CSRZ-DPSK) signal up to 5 round-trips using recirculating loop, see Section 2.4.

2.2 Introduction to Micro-Ring Resonators

2.2.1 Basic configuration

The most basic configuration of a MRR consists of unidirectional coupling between a ring waveguide with radius r and a straight waveguide [24, 25], as illustrated in Fig. 2.1.

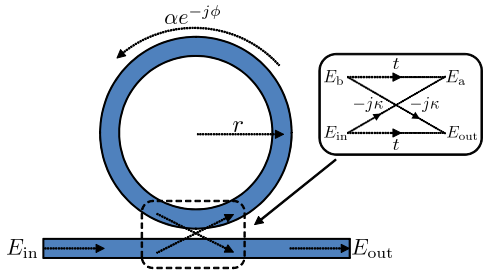

Figure 2.1: Model of basic configuration of MRR: a single ring resonator with one straight waveguide.

The transmission parameter t and coupling parameter κ are used to describe the unidirectional coupler, as described in Fig. 2.1. If we consider waveguide supporting a single mode and a single polarisation, the field transfer characteristics of the MRR can be expressed as:

$$\begin{pmatrix} E_{\mathrm{out}} \\ E_{\mathrm{a}} \end{pmatrix} = \begin{pmatrix} t & -j\kappa \\ -j\kappa & t \end{pmatrix} \begin{pmatrix} E_{\mathrm{in}} \\ E_{\mathrm{b}} \end{pmatrix} . \tag{2.1}$$

When lossless coupling is considered,

$$t = \sqrt{1-\kappa^2} . \tag{2.2}$$

The propagation in the ring can be described by

$$E_{\mathrm{b}} = \alpha \cdot e^{-j\phi} E_{\mathrm{a}} \ . \tag{2.3}$$

where α is the loss coefficient (zero loss: $\alpha = 1$) and the phase shift is $\phi = \omega L/c$. L is the propagation length in the ring which depends on the radius r of the ring according to $L = 2\pi r$. c is the phase velocity of the ring mode, $c = c_0/n_{\mathrm{eff}}$, where c_0 is the speed of light in vacuum and n_{eff} is the effective reflective index of the material.

From Eq. 2.1 and Eq. 2.3, we obtain the transfer function of the MRR,

$$H = \frac{E_{\mathrm{out}}}{E_{\mathrm{in}}} = \frac{E_{\mathrm{t1}}}{E_{\mathrm{i1}}} = \frac{t - \alpha e^{-j\phi}}{1 - t \cdot \alpha e^{-j\phi}} \ . \tag{2.4}$$

Because of the unique properties of its transfer function, such a filter is typically referred to as "notch" filter.

One of the most important characteristics of resonator filters is the separation between adjacent resonance peaks, which is called the free spectral range (FSR). The FSR can be expressed as

$$\Delta\nu_{\mathrm{FSR}} = \Delta\lambda_{\mathrm{FSR}} \simeq \frac{\lambda^2}{n_{\mathrm{eff}} L} \ . \tag{2.5}$$

The quality factor Q is a figure to describe the sharpness of the resonance. It is defined as the ratio of the centre frequency and the full width at half maximum (FWHM) of the resonance

$$Q = \frac{\nu_0}{\Delta\nu_{\mathrm{FSR}}} \ . \tag{2.6}$$

A phase shift is always associated with the loss or gain of a medium, following Kramers-Kronig relations. Therefore the MRR presents dispersion to the signal that passes through the MRR and its group-velocity dispersion (GVD) parameter D can calculated from its phase response.

$$D = \frac{d\tau}{d\lambda} = \frac{d\tau}{d\omega}\frac{d\omega}{d\lambda} = -\frac{2\pi c}{\lambda^2}\frac{d\phi}{d\lambda} \ . \tag{2.7}$$

As an illustration, some amplitude responses and associated dispersion profiles of the basic configuration MRRs with different design parameters can be found in Fig. 2.2. These transfer functions will be used to compare the response difference between different MRR designs in order to choose the right one for the use in the chirp managed laser (CML) transmitter design described in Chapter 3.

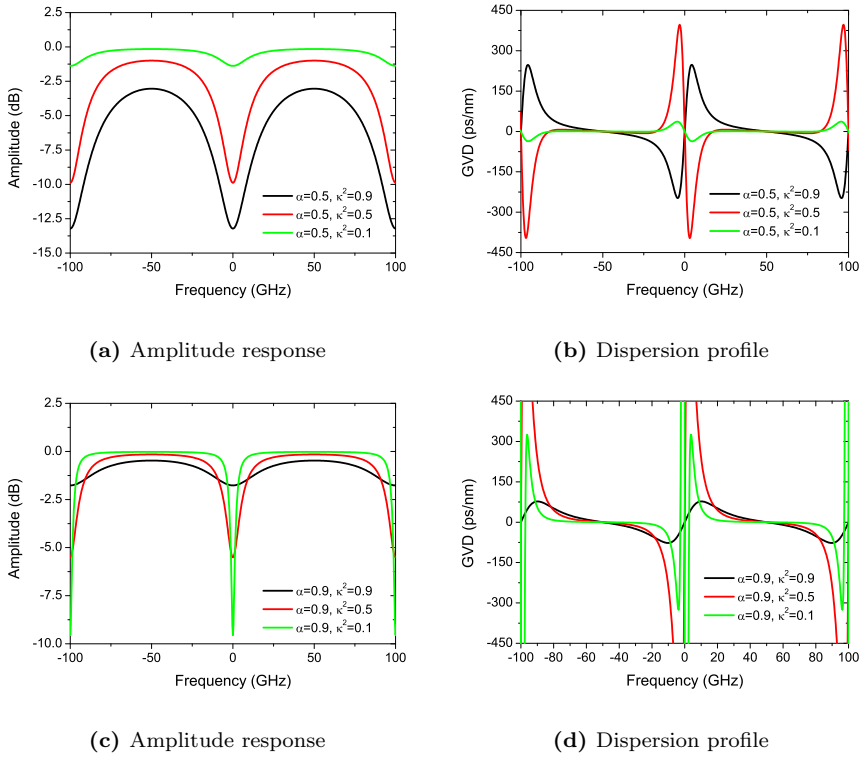

(a) Amplitude response **(b)** Dispersion profile

(c) Amplitude response **(d)** Dispersion profile

Figure 2.2: Transfer functions and dispersion profiles for a basic configuration MRR with FRS=100 GHz. (a)-(b) Round-trip loss coefficient α =0.5 and coupling coefficient κ^2 =0.1, 0.5, 0.9; (c)-(d) Round-trip loss coefficient α =0.9.

2.2.2 Add-drop configuration

Adding one more straight waveguide to the basic configuration, a ring resonator can be made as an add-drop filter, which has four ports as illustrated in Fig. 2.3(a). Let the parameters of the directional coupler on the in-through waveguide $\{t_1, -j\kappa_1\}$ and those on the add-drop waveguide $\{t_2, -j\kappa_2\}$. We assume the total attenuation in the ring is uniform and the ring is much longer than the coupling length of the two couplers. Therefore we can divide the loss and phase shift into two part and one for each half of the ring. The transfer function can be obtained

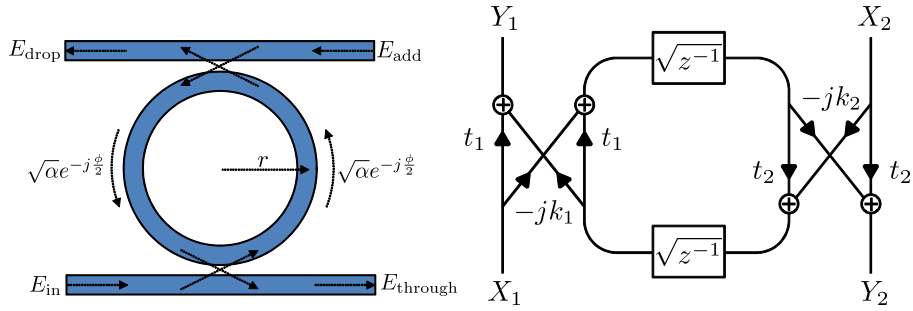

(a) Configuration **(b)** Z-transform layout

Figure 2.3: Model of add-drop configuration of MRR: a single ring resonator with two waveguide.

by extending the equations described in Section 2.2.1, resulting in

$$E_{\text{through}} = \frac{t_1 - t_2\alpha e^{-j\phi}}{1 - t_1 t_2 \alpha e^{-j\phi}} E_{\text{in}} \ , \tag{2.8}$$

$$E_{\text{drop}} = \frac{-\kappa_1\kappa_2\sqrt{\alpha}e^{-j\frac{\phi}{2}}}{1 - t_1 t_2 \alpha e^{-j\phi}} E_{\text{in}} \ . \tag{2.9}$$

As the add-drop type ring resonator is symmetric, another approach using the digital filter concept and Z-transformation can also be used to analyse the ring resonator as well [26]. The advantage of using Z-transformation to model the ring resonator is that it simplifies the model comparing to the field analysis described in Section 2.2.1. We use the same definitions of the parameters, and define the transfer functions are:

$$H_{11} = \frac{E_{\text{through}}}{E_{\text{in}}} \ , \qquad H_{12} = \frac{E_{\text{through}}}{E_{\text{add}}} \ ,$$

$$H_{21} = \frac{E_{\text{drop}}}{E_{\text{in}}} \ , \qquad H_{22} = \frac{E_{\text{drop}}}{E_{\text{add}}} \ .$$

The Z-transform is a discrete-time equivalent of the Laplace transform. It is used to analyse and design digital filters. A digital filter's transfer function, $H(z)$ can be expressed by a ratio between M^{th} and a

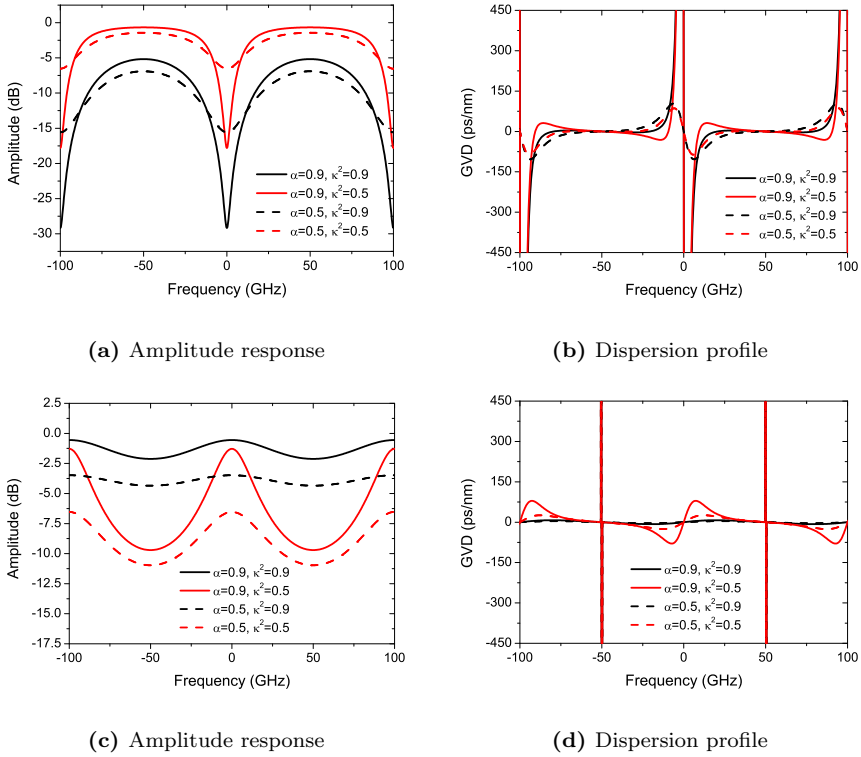

(a) Amplitude response

(b) Dispersion profile

(c) Amplitude response

(d) Dispersion profile

Figure 2.4: Transfer functions and dispersion profiles of an add-drop configuration MRR with FRS=100 GHz. (a)-(b) In to through; (c)-(d) In to Drop response with loss coefficient α =0.9 and $\kappa_1^2 = \kappa_2^2$ =0.5 and 0.9.

N^{th} order polynomials.

$$H(z) = \frac{\Gamma z^{N-M} \prod_{m=1}^{M} (z - z_m)}{\prod_{n=1}^{N} (z - p_n)} \,. \tag{2.10}$$

The zeros of the numerator are represented by z_m, which are also called the zeros of $H(z)$. A zero will result in zero transmission at the frequency. The p_n in the denominator are called poles. For a MRR, a autoregressive (AR) filter, has only poles and one or more feedback paths [26]. Fig. 2.3(b) shows the Z-transform schematic for the add-

drop type MRR shown in Fig. 2.3(a). This type of resonator filter is the simplest filter with only one pole response. Solving the Z-transformation scheme, the transfer functions can be obtained:

$$H_{11} = \frac{t_1 - t_2\alpha z^{-1}}{1 - t_1 t_2 \alpha z^{-1}} \ , \tag{2.11}$$

$$H_{22} = \frac{t_2 - t_1\alpha z^{-1}}{1 - t_1 t_2 \alpha z^{-1}} \ . \tag{2.12}$$

Since we assume the loss in the ring is uniform and the MRR design is symmetric, we will have

$$H_{12} = H_{21} = \frac{-\kappa_1\kappa_2\sqrt{\alpha z^{-1}}}{1 - t_1 t_2 \alpha z^{-1}} \ . \tag{2.13}$$

Fig. 2.4 shows some amplitude responses and associated dispersion profiles of both in-through and in-drop port of an add-drop MRRs with the same design parameters as in Section 2.2.1. Adding one waveguide improves the Q factor but also decreases the transmission in the pass-band. Meanwhile more dispersion is introduced.

2.2.3 Coupled double ring configuration

In the serially coupled configuration, each ring is coupled to one another. Serially coupled ring resonators are also called coupled-resonator optical waveguide (CROW).

Their transfer functions can be described as

$$H_{11} = \frac{t_1 - t_2\alpha_1 e^{-j\phi_1} - t_1 t_2 t_3 \alpha_2 e^{-j\phi_2} + t_3\alpha_1\alpha_2 e^{-j\phi_1} e^{-j\phi_2}}{1 - t_1 t_2 \alpha_1 e^{-j\phi_1} - t_2 t_3 \alpha_2 e^{-j\phi_2} + t_1 t_3 \alpha_1 \alpha_2 e^{-j\phi_1} e^{-j\phi_2}} \ , \tag{2.14}$$

$$H_{22} = \frac{t_3 - t_2\alpha_2 e^{-j\phi_2} - t_1 t_2 t_3 \alpha_1 e^{-j\phi_1} + t_1\alpha_1\alpha_2 e^{-j\phi_1} e^{-j\phi_2}}{1 - t_1 t_2 \alpha_1 e^{-j\phi_1} - t_2 t_3 \alpha_2 e^{-j\phi_2} + t_1 t_3 \alpha_1 \alpha_2 e^{-j\phi_1} e^{-j\phi_2}} \ , \tag{2.15}$$

$$H_{12} = \frac{k_1 k_2 k_3 \sqrt{\alpha_1}\sqrt{\alpha_2} e^{-j\frac{\phi_1}{2}} e^{-j\frac{\phi_2}{2}}}{1 - t_1 t_2 \alpha_1 e^{-j\phi_1} - t_2 t_3 \alpha_2 e^{-j\phi_2} + t_1 t_3 \alpha_1 \alpha_2 e^{-j\phi_1} e^{-j\phi_2}} \ , \tag{2.16}$$

$$H_{21} = H_{12} \ , \tag{2.17}$$

where the parameters describing the coupled MRR are defined in Fig. 2.5.

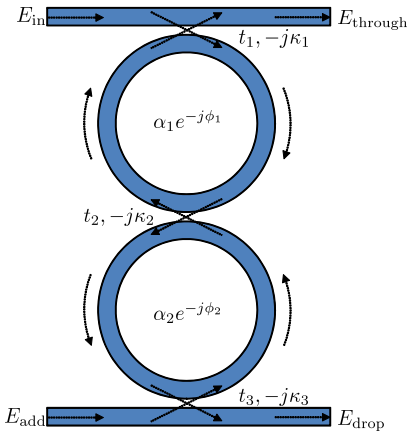

Figure 2.5: Serially coupled double ring resonator

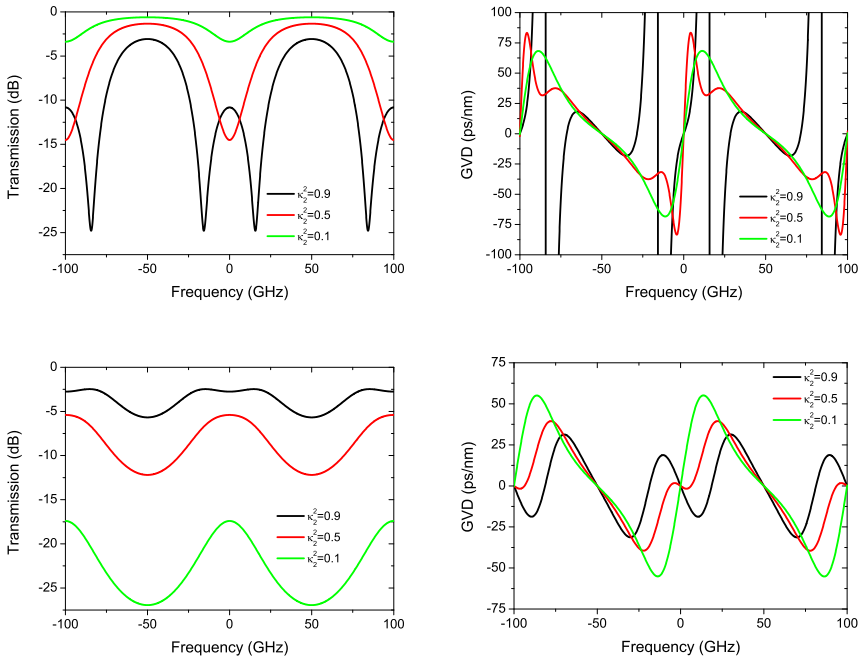

Figure 2.6: Transfer functions and associated dispersion profiles of a coupled double-ring resonator with FSR=100 GHz and different design parameters: κ_2^2 =0.1, 0.5 and 0.9 while $\kappa_1^2 = \kappa_3^2 = 0.9$ and the loss coefficient $\alpha_1 = \alpha_2 = 0.9$.

Compared to the transfer functions of the add-drop type MRR, the coupling MRR has a very different in-through transfer function, where two notch resonances appeared within one FSR when the coupling coefficient κ_2 is high. While with the same κ_2, the in-drop transfer function then has a flat-top response, as shown in Fig. 2.6. The coupled MRR with more than two rings can modify this flat-top response, therefore the coupled MRR has potential for flat-top filter design.

2.3 Fabrication Process

Silicon MRRs were fabricated for our system experiments in DANCHIP clean room by Yunhong Ding. Fig. 2.7(a) shows the SEM image of a MRR with 55 μm radius used in a system experiment described in Section 3.4 of the next chapter. It was fabricated on a silicon-on-insulator (SOI) wafer with top silicon thickness of 250 nm and buried silicon dioxide of 3 μm. First, electron-beam resist ZEP520A was spined to coat the wafer with a ~110 nm thick mask layer. The structure of the MRR device was then defined by electron-beam lithography, then formed on the silicon layer by inductively coupled plasma reactive ion etching (ICP-RIE) etching. A layer of 600 nm thick benzocyclobutene (BCB) is used to cover the waveguide and form the upper cladding layer to protect

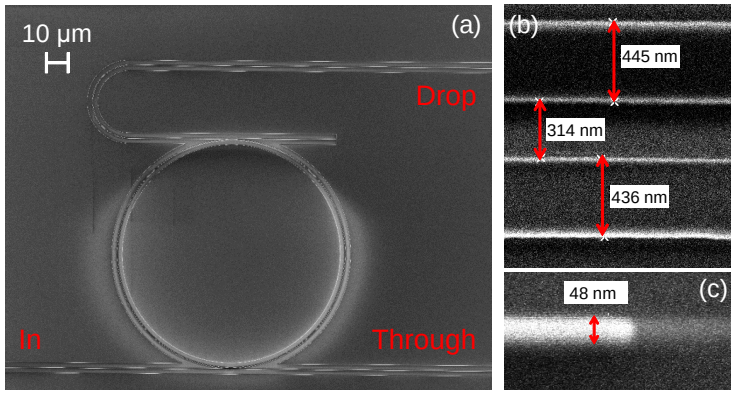

Figure 2.7: SEM image of a 55 μm radius MRR, with a coupling gap of 320 nm. The input and output waveguide were inversely tapered to increase the coupling efficiency. (a) MRR, (b) Coupling gap and (c) Inverse taper

the device. After that, a layer of 3.5 μm thick polymer (SU8-2005) was spin-coated on top of the BCB layer. Nano-couplers were also defined by electron-beam lithography. The radius of the MRR is 55 μm with a waveguide width of 435 nm and coupling gap of 320 nm for both through and drop coupling regions. The silicon waveguide is inversely tapered to 45 nm, covered by a polymer waveguide to form a nano-coupler, resulting in ultra-low coupling loss [27] to the fibre. More details on the fabrication process can be found in [28].

2.4 Cascadability of Micro-Ring Resonator

MRRs are proposed to be integrated in a chip for optical interconnect and network-on-chips [7–10]. Even though they are designed for high-speed networks or interconnect applications in mind, very few studies have so far considered the impact of MRR filtering on high-speed modulated signals. The system penalty induced by one single or double ring resonator structure on 10 Gbit/s non return-to-zero differential on-off keying (NRZ-OOK) signals has been first investigated in [29] and [30]. Very recently, switching of 10 Gbit/s differential phase shift keying (DPSK) signals through a second order silicon micro-ring switch has been demonstrated [31]. Higher order MRRs are used in this context since their wider and flatter passbands prevent the occurrence of phase-to-intensity modulation conversion [31]. The bit error rate (BER) performance of coupled ring resonators has also been given recent consideration [32] for NRZ-OOK signals at 10 Gbit/s. However, for MRR-based scalable high-speed interconnect architectures or WDM add-drop nodes to constitute a practical solution, the cascadability of the MRRs should be ensured for high bit rate signals, which has not been demonstrated so far.

In this section, the cascadability of silicon MRRs used as bandpass filters to their drop port is experimentally investigated for CSRZ-OOK and CSRZ-DPSK signals at 40 Gbit/s. A re-circulating loop platform is used to assess the impact of the MRR transfer function on high-speed modulated signals. Error-free performance is demonstrated for both CSRZ-OOK and CSRZ-DPSK after 5 cascaded silicon MRRs. A higher tolerance to bandwidth reduction is obtained for CSRZ-OOK compared to CSRZ-DPSK due to the partial demodulation of the latter format

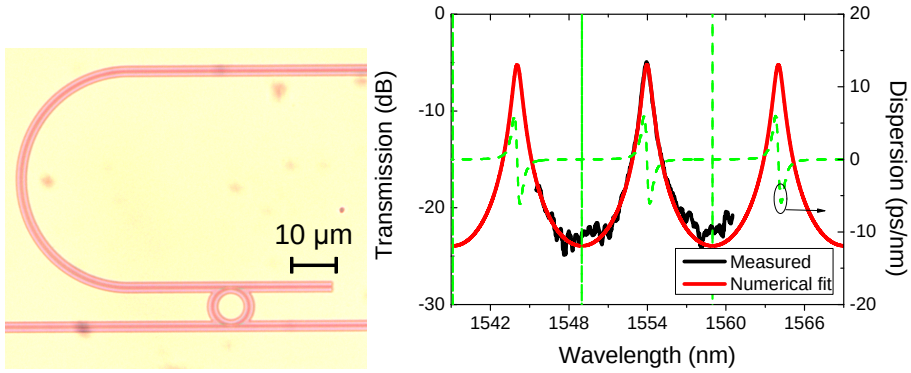

(a) (b)

Figure 2.8: The 9.2 μm radius MRR used for the experiment to assess the cascadability of MRRs. (a) 9.2μm MRR image, (b) its measured and fitted transfer functions

induced by cascaded bandwidth narrowing.

The silicon MRR used in the experiment has a radius 9.2 μm, with 80 nm coupling gap, as shown in Fig. 2.8(a). Fig. 2.8(b) shows the measured transfer function at the drop port of the MRR. The measured FSR is 1235 GHz and the Q factor is 2192, corresponding to a FWHM bandwidth of 88 GHz. The total insertion loss of the device is about 5 dB and the extinction ratio (ER) of the drop transmission is 20 dB. Numerical fitting was performed and the transfer function and dispersion profile are shown in Fig. 2.8(b). The parameter used for the fitting are: FSR = 1240 GHz, power coupling coefficient $\kappa_1^2 = \kappa_2^2 = 0.12$ and loss coefficient $\alpha = 0.9$.

2.4.1 Experimental setup

The experimental recirculating loop setup for investigating the cascadability of a single MRR used as drop filter is illustrated in Fig. 2.9. The optical transmitter consisted of two $LiNbO_3$ Mach-Zehnder modulators (MZMs) generating 40 Gbit/s CSRZ-OOK or CSRZ-DPSK signals. The first MZM, driven by a 20 GHz clock signal, was used as pulse carver while the second one was driven by a 40 Gbit/s pseudo random bit sequence (PRBS) with a pattern length of $2^{31} - 1$. The optical signal was then boosted by an erbium doped fibre amplifier (EDFA) before

being input to the loop.

The loop switch consists of two acousto-optic modulators (AOMs). A dispersion compensated span consisting of 80 km standard single mode fibre (SSMF) and 13 km dispersion compensation fibre (DCF) was used to store the data in the loop and enable the recirculations. After the transmission span, the optical signal was coupled into the MRR via a tapered fiber and collected again at the drop port by another tapered fiber. An EDFA was used for compensating the insertion and coupling loss of the resonator and loop switch. Data was continuously sent, via a 90/10 coupler, to the receiver. Gating of the BER test-set and the oscilloscope enabled the characterisation of the signal after the last round-trip in the loop. The signal was detected in a pre-amplified receiver, comprising a 45 GHz photodiode for on-off keying (OOK) and a 1-bit fiber delay interferometer followed by a balanced detector, also with 45 GHz bandwidth, for DPSK. Since the MRR is polarisation sensitive, it was ensured the signal at its input was properly polarised for each round trip. This was achieved thanks to a polariser at its input, and intra- and extra-loop polarisation controllers (PCs) enabling to find a stable principal state of polarisation for the loop.

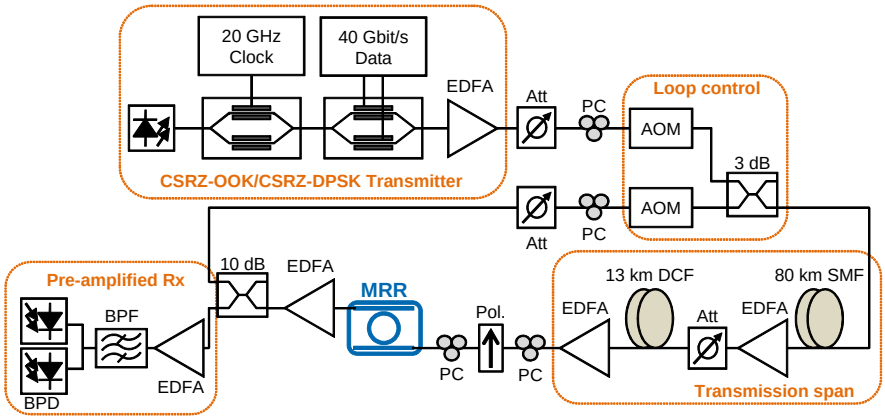

Figure 2.9: Experimental setup for investigation of MRR cascadability

2.4.2 Experimental results

Fig. 2.11 shows the results of BER measurements for the 40 Gbit/s CSRZ-OOK and CSRZ-DPSK signals transmitted through different numbers of round trips in the loop. The penalty when increasing the number of circulations is induced by bandwidth narrowing, resulting in waveform degradation and inter-symbol interference (ISI). The CSRZ-DPSK format can be seen to exhibit larger penalty than CSRZ-OOK. However, dispersion management and noise accumulation are critical at 40 Gbit/s and some of the measured penalty is actually attributed to the necessary transmission span in the loop.

In order to isolate the impact of the MRR on the transmission performance from that of the cascaded transmission spans and loop artifacts, the recirculating loop measurement was repeated with a (broad) 3 nm FWHM thin-film filter (TFF) replacing the MRR. The bandwidth of the TFF was chosen to be wide enough to ensure the signal was not affected by any filtering effect even after 5 round trips. A variable optical attenuator (VOA) was inserted in the loop to emulate the insertion loss of the MRR in order to ensure a fair comparison with respect to noise accumulation. The isolated impact of the MRR is compared for the two modulation formats in Fig. 2.11, where the transmission penalties obtained from the measurements with the wide TFF have been subtracted from the power penalties measured with the MRR in the loop. A power penalty around 1 dB is measured after one single MRR due to

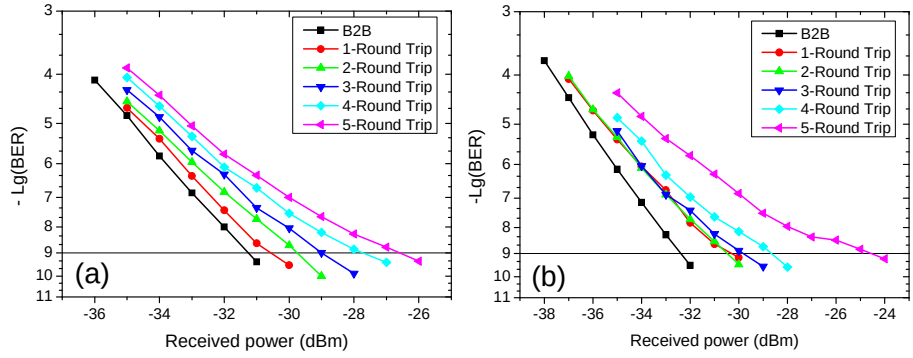

Figure 2.10: BER as a function of received power for different number of round trips in the loop and for (a) CSRZ-OOK and (b) CSRZ-DPSK modulation.

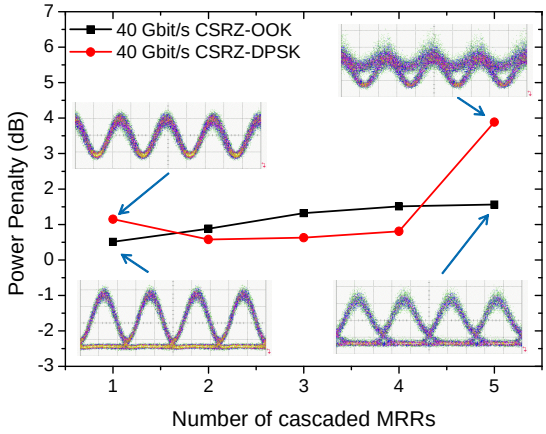

Figure 2.11: Power penalty (at BER = 10^{-9}) induced by cascading a single MRR versus number of cascades for CSRZ-OOK and CSRZ-DPSK signals.

its relatively wide 88 GHz FWHM bandwidth. Similar levels of power penalty are measured for both formats up to 4 cascaded MRRs. After 5 cascaded MRRs, the effective bandwidth of the cascade is reduced to 36 GHz, shown in Fig. 2.12, at which value some DPSK signal demodulation [28] occurs, as can be seen in the corresponding eye diagram in the inset of Fig. 2.11. This results in an increased penalty for CSRZ-DPSK compared to CSRZ-OOK.

2.4.3 Numerical comparisons and discussions

The effective transfer function of cascaded filters is the result of the total product of all the filter transfer functions. The FWHM after cascading will drop down quickly except for those flat-top filters. Fig. 2.12 shows the calculated transfer function of cascading the MRRs using the fitted parameters as in Fig 2.8. The FWHM dropped to 36 GHz, less than half of the bandwidth after 5 cascaded MRRs.

It was also noticed that the eye diagram of the CSRZ-DPSK signal after 5 cascaded MRRs shown in Fig. 2.11 not only has been partially demodulated, but also showed a slight asymmetric distortion. This demodulation distortion was already clearly visible after 3 cascaded MRRs as shown in Fig. 2.13, even though its impact on the receiver sensitivity penalty was hardly noticed.

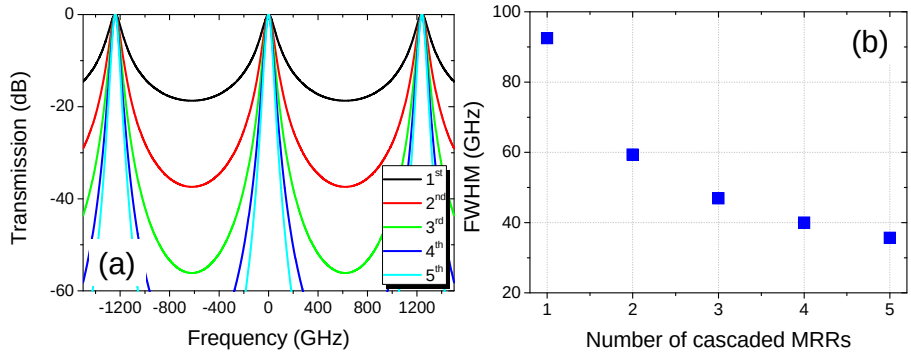

Figure 2.12: Calculated (a) transfer functions and (b) effective bandwidths of cascaded MRRs as drop filters.

In order to understand the asymmetric distortion appearing on the eye diagram as shown in Fig. 2.13, system simulations using 50% return-to-zero differential phase shift keying (RZ-DPSK) at 40 Gbit/s and MRRs described by the parameters obtained from numerical fitting were carried out.

This distortion might come from the misalignment between the filter and the signal. However we measured the BER performance when the CSRZ-DPSK signal was detuned 0 nm to 3.45 nm from the centre wavelength of the MRR drop port transfer function, without cascading. Apart from losing power, no signal quality degradation nor waveform distortion was noticed. This conclusion was confirmed by numerical simulation.

Another possible source for the distortion is chromatic dispersion in the MRR. Therefore, the system was simulated by suppressing the dispersion in the MRR transfer function, H. The dispersion-free trans-

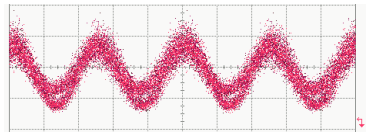

Figure 2.13: Eye diagram of 40 Gbit/s CSRZ-DPSK signal transmitted after 3 round trips. Partial demodulation with asymmetric distortion can be noticed on the eye.

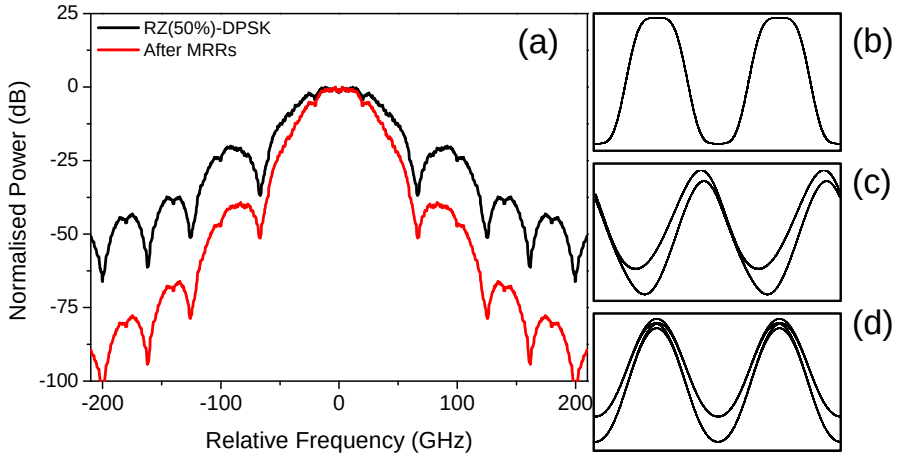

Figure 2.14: Simulated dispersion effect on DPSK signals from 3 cascaded MRRs using the parameter obtained from numerical fitting of the MRR used for experiment. (a) Signal spectra; Eye-diagrams of (b) back-to-back 50% RZ-DPSK signal (c) the signal filtered by cascaded MRRs with dispersion and (d) without dispersion.

fer function H' is related to H by $H' = \sqrt{H \cdot H^*}$. In the simulation, 50% RZ-DPSK at 40 Gbit/s signal with PRBS length of $2^{11} - 1$ was used and 3 MRRs were cascaded. The spectra of the signal before and after MRR are shown in Fig 2.14(a). The eye diagram of the signal after cascaded filtering with dispersion in the MRR (Fig 2.14(c)) is similar to what we have noticed in the experiment: partial demodulated and asymmetric distorted. While the eye simulated without dispersion (Fig 2.14(d)) has no asymmetric distortion. Therefore we attribute the asymmetric distortion to the phase response of the MRR.

2.5 Summary

In this chapter, The silicon MRRs were introduced and the transfer function of different configuration (basic, add-drop and coupled-ring designs) were calculated together with their associated dispersion profiles. The cascadability of silicon MRRs used as bandpass filters to their drop port has been experimentally investigated for CSRZ-OOK and CSRZ-DPSK signals at 40 Gbit/s. A re-circulating loop platform was used to assess the impact of the MRR transfer function on high-speed modulated

signals. Error-free performance was demonstrated for both CSRZ-OOK and CSRZ-DPSK after 5 cascaded silicon MRRs with free spectral range FSR of 1235 GHz and Q factor of 2192. A higher tolerance to bandwidth reduction is obtained for CSRZ-OOK compared to CSRZ-DPSK due to the partial demodulation of the latter format induced by cascaded bandwidth narrowing. The asymmetric distortion on the optical eye-diagram of CSRZ-DPSK signal after cascaded MRRs was attributed to the phase response of the MRRs, according to numerical simulations.

Chapter 3

Modulation Speed Enhancement of Directly Modulated Lasers

3.1 Introduction

Short-range applications such as in local area networks (LANs) or data centres require low cost, compact and low hardware expense solutions. Therefore, directly modulated laser (DML) systems with on-off keying (OOK) modulation are often preferred over schemes based on external modulators and using more sophisticated modulation formats. However, the bandwidth requirements of such applications are constantly increasing at a tremendous pace in order to e.g. reduce the number of parallel interconnects or support new services such as high-definition video. In spite of continuous progress, increasing the bandwidth of directly modulated lasers remains a challenge. Edge emitting DMLs [33–35] as well as vertical-cavity surface-emitting lasers (VCSELs) [36,37] capable of operating at 40 Gbit/s have already been demonstrated. However, generating and transmitting such high-speed directly modulated signals error-free (i.e. with a bit error rate (BER) lower than 10^{-9}) is still challenging due to inter-symbol interference, and ringing artifacts induced by bandwidth limitations and relaxation oscillations.

The use of frequency modulation (FM) to amplitude modulation

(AM) conversion in directly modulated transmitters has attracted much attention for telecommunication applications over the past decade. In chirp managed lasers (CMLs) [38–40], a DML is biased at a high current value and modulated with a relatively low peak-to-peak current, leading to a low extinction ratio (ER) signal whose chirp is dominated by its adiabatic contribution [41]. Subsequent filtering enables to increase the signal extinction ratio, resulting in the generation of a signal with limited distortion, which is furthermore tolerant to group velocity dispersion [42]. CMLs employing different filter technologies, including multi-cavity filters [38], fibre Bragg gratings [43], thin-film filters (TFFs) [44], or fibre delay interferometers (DIs) [45–47] have been demonstrated. Using this technique, 40 Gbit/s error-free transmission over 25 km negative-dispersion fibre (~ -1.7 ps/nm/km) [48] has been demonstrated. With BERs compatible with the forward error correction (FEC) threshold, 42.8 Gbit/s transmission over 20 km single mode fibre (SMF) has been achieved [49] and applied to a wavelength division multiplexing (WDM) passive optical network (PON) system [50]. In addition, the use of a filter with periodic frequency response such as a DI enables the deployment of the CML technology in WDM systems, including WDM-PONs, by only employing one additional element compared to conventional systems, making the technique cost-effective [39, 51].

Even though the main focus of the CML technology has been to improve the dispersion tolerance of directly modulated signals, and in particular to allow transmission over uncompensated spans, the signal quality enhancement associated with the chirp filtering process also enables DMLs to be operated at a bit rate higher than that allowed by their nominal bandwidth, as detailed further in this chapter. For future short range applications operating at 40 Gbit/s and beyond, where cost considerations are of high importance, being able to operate a system error-free without resorting to expensive high-speed FEC circuits is an advantage. It is therefore essential to be able to demonstrate directly modulated transmitters able to reach error-free performance at such bit rates. Furthermore, all the CML solutions presented so far are relatively bulky due to the need for optical filtering and are therefore not suitable for integration, which would present a significant footprint and cost benefit advantage for short-range and interconnect links.

We propose, comprehensively analyse and demonstrate the use of a

silicon micro-ring resonator (MRR) as an ultra-compact filter in a CML transmitter in order to increase the modulation speed of the DML. We analysed numerically the MRR design influence on the system performance. Using the proposed scheme, we experimentally demonstrate a 40 Gbit/s transmitter with error-free (BER $\leq 10^{-9}$) performance based on a commercially available 10 Gbit/s distributed feed-back (DFB) laser. Furthermore, we assess the transmission performance of the proposed transmitter over fibre lengths compatible with short-reach applications. The scheme is directly applicable to other directly modulated sources such as VCSELs, where it could benefit from hybrid integration of the laser on the silicon-on-insulator platform, as proposed in e.g. [52]. In order to verify the modulation enhancement on a VCSEL, a 1530 nm VCSEL, whose maximum 3-dB modulation response is 17.6 GHz, is modulated at 25 Gbit/s, where its performance is not error-free, and filtered using the same scheme. The achieved error-free performance, with space for further improvement, demonstrates experimentally that the scheme can be applied to VCSELs. MRRs are also able to process multiple wavelengths simultaneously thanks to their periodic frequency response. Furthermore, the proposed scheme can be scalable to higher data rates, enabling a potentially low-cost, low-power consumption and ultra-compact high-speed multi-wavelength transmitter.

This chapter is structured as follows:

The operation principle of the proposed method using a MRR to enhance the modulation speed of a DML is presented in Section 3.2. Numerical simulations were carried out using rate equation parameters extracted from a commercial 10 Gbit/s DFB laser diode to study the signal properties after the MRR and its dispersion tolerance for transmission, which are also shown in Section 3.2. In order to find the optimum MRR design, simulations using different MRR design parameters were compared and presented in Section 3.3. In Section 3.4, the experiment, in which a 40 Gbit/s directly modulated transmitter using a 10 Gbit/s commercial DFB laser diode was demonstrated error-free, is presented. The transmission properties of the signal generated with the proposed transmitter were also experimental studied. Finally, an experimental demonstration of the scheme using a VCSEL diode is presented in Section 3.5.

3.2 Principle of Operation and Numerical Simulations

3.2.1 Principle

The transmission distance of directly modulated signals is strongly limited by transient chirp, depending on the sign of the accumulated dispersion [53]. In order to overcome this limitation, DMLs can be biased with a high current so that the adiabatic chirp is dominant over the transient chirp. This presents the additional benefits of enhanced modulation bandwidth and increased damping of the relaxation oscillations, leading to a clear eye diagram, however at the expense of a detrimental reduction of the signal ER. The dominant adiabatic chirp results in the ones being blue-shifted with respect to the zeros. This frequency separation can in turn be exploited using frequency discrimination [38]. If an optical filter is used to suppress the frequency components corresponding to the zeros, the extinction ratio of the signal will be restored. Apart from mitigating the effect of dispersion, this principle can be used to generate good quality signals beyond the nominal bandwidth of the DML and therefore to enhance the modulation speed of directly modulated transmitters.

In our proposed scheme, illustrated in Fig. 3.1, an ultra-compact silicon add-drop type MRR [23] is employed as a periodic notch filter to suppress the frequency components corresponding to the zeros at the output of a DML driven beyond its nominal bit rate. The transfer function, Eq. 2.11, of such a filter is analysed in Chapter 2. It has been assumed that the MRR is geometrically symmetric with equal power coupling coefficient ($\kappa_1^2 = \kappa_2^2$) between the ring and the input/through and add/drop waveguides, respectively. It has also been assumed that the loss in the coupling region can be neglected, the power transmission coefficient t is linked to the coupling coefficient to the ring κ according to $t^2 + \kappa^2 = 1$.

If the MRR is tuned so that one of its resonances matches the signal instantaneous frequency corresponding to the zeros, a signal with good eye quality and improved extinction ratio is obtained at the output of the MRR, as shown in Fig. 3.1.

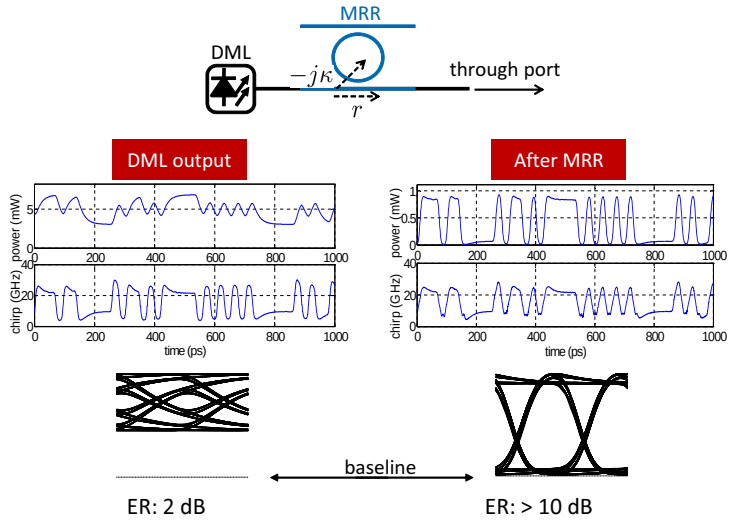

Figure 3.1: Principle of the proposed method. The signal emitted by a DML operated beyond its nominal bit rate is filtered at the through port of a silicon MRR. The suppression of the frequency components corresponding to the modulated zeros results in an increase of the signal extinction ratio and opening of the eye diagram. The method is illustrated with simulated waveforms and eye diagrams corresponding to a 10 Gbit/s DML driven with a 42.8 Gbit/s signal.

3.2.2 Signal properties after the MRR

The properties of the signal generated by the MRR filtering are numerically evaluated by assessing its extinction ratio (ER) and chirp. In this analysis, the laser is modulated by a set of standard rate equations [54]. The parameters used in the rate equation model are listed in Table 3.1. The values of the parameters were extracted from a commercially available DML (NEL model NLK5C5EBKA [55]) that was used later in the experiments presented in Section 3.4. This laser is a standard product designed for 10 Gbit/s operation. The laser was driven at 42.8 Gbit/s by a de Bruijn sequence of length of 2^9. The peak-to-peak modulation was 50 mA and the bias current was 75 mA, resulting in the generation of a signal with about 2 dB ER and 12 GHz adiabatic chirp difference between “0”s and “1”s.

The modulated signal was then input to an add-drop MRR for frequency discrimination. The power transfer functions and dispersion

Name	Symbol	Symbol	Units
Photon lifetime	τ_p	20.2	ps
Carrier lifetime	τ_n	862	ps
Carrier density at transparency	N_0	1.3421×10^{24}	$1/\mathrm{m}^3$
Gain cross section	σ_g	5.09×10^{-20}	m^2
Group effective index	n_g	2.14	
Confinement factor	Γ	0.36	
Active volume	V_a	3.81×10^{-17}	m^3
Gain suppression factor	ϵ_{NL}	1.5×10^{-23}	
Linewidth enhancement factor	α	3.39	
Spontaneous emission factor	β	4.02×10^{-3}	
Differential quantum efficiency	η_0	0.19	

Table 3.1: DML rate equation parameters and values used in the numerical analysis

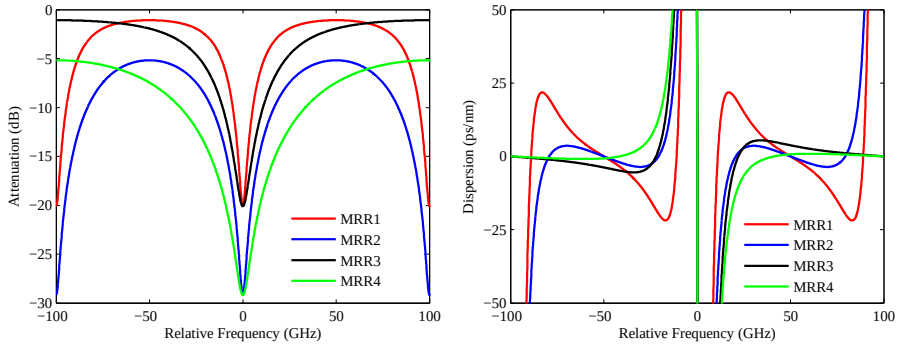

(a) Amplitude response **(b)** Dispersion profile

Figure 3.2: Transfer functions at the through port for four different MRR designs considered in this study.

MRR Name	FSR (GHz)	κ^2	α
MRR1	100	0.6	0.9
MRR2	100	0.9	0.9
MRR3	200	0.6	0.9
MRR4	200	0.9	0.9

Table 3.2: MRR design parameters

profiles of four different MRR designs, whose parameters are listed in Table 3.2, are shown in Fig. 3.2. These designs were chosen as representative examples of the variety of transfer functions achievable by engineering the diameter of the ring, hence its free spectral range (FSR), and the coupling coefficient of the MRR, in order to illustrate the robustness of the proposed scheme to the MRR parameters. Fig. 3.2(a) confirms that the MRR transfer functions have multiple notches spaced by the FSR. This imposes that the FSR should be larger than the spectral width of the directly modulated signal, which depends on the bit rate, modulation bandwidth and adiabatic chirp, in order to only suppress the blue-shifted part of the spectrum. On the other hand the periodicity of the transfer function can be exploited for simultaneously processing a number of wavelength channels spaced by multiples of the FSR. In addition, the dispersion of the different MRR designs is also represented in Fig. 3.2(b). The dispersion around the resonant frequencies reaches maxima of about ±5000 ps/nm for MRR1 and MRR2 and about ±1200 ps/nm for MRR3 and MRR4.

The ER of the signal generated at the output of the through port of the MRR is shown as a function of the detuning with respect to a resonance (defined as $\Delta\lambda = \lambda_{\text{laser}} - \lambda_{\text{resonance}}$, where λ_{laser} is the centre wavelength of the DML spectrum without modulation and $\lambda_{\text{resonance}}$ is the resonance wavelength) in Fig. 3.3. It can be noticed that, even though the signal generated by the DML had a low ER of the order of 2 dB, the ER after MRR filtering was enhanced to values above 15 dB, with an optimum detuning for all the evaluated MRRs. The inset (b) in Fig. 3.3 shows that the red-shifted zero level was suppressed in the eye diagram corresponding to the maximum ER enhancement. When the MRR notch was tuned from the optimum detuning towards the blue, Fig. 3.3(c), the overshoot became higher. On the other hand, when the MRR dip was tuned towards the red, Fig. 3.3(a), the zero level suppression was lower than in the optimum case and the signal overshoot was smaller.

Fig. 3.4 represents the chirp before and after the filtering of the directly modulated signal by the MRR. The adiabatic chirp was not significantly modified by the filtering. Nonetheless, the MRR filtering introduced transient chirp. These results are in agreement with previous analysis of CML systems and their theoretical derivations of the chirp

after filtering [38].

3.2.3 Dispersion tolerance

The transmission properties of the CML signal over dispersive fibres were assessed next. Thermal noise limited detection is assumed in this analysis, which would typically be the case in short-range links that do not resort to optical amplification. Since the modulation speed enhancement by the MRR effectively relies on the mitigation of inter-symbol interference (ISI) introduced by the bandwidth-limited DML, the performance of the system was evaluated through the BER calculated using error-counting. This is in contrast with typical Gaussian approximations of the probability density functions of the zeros and ones, which are known to overestimate the BER under strong ISI conditions. Due to this approach, the sensitivity was evaluated at a BER of 10^{-3} following the detection of a statistically significant number of errors, chosen here equal to 100. As in the previous subsection, the CML signals are generated by filtering DML signals with the four MRR designs described in Table 3.2. They were then transmitted over a variable length of fibre with either positive or negative dispersion. Since the focus is on dispersion tolerance, optical fiber nonlinearities were neglected in this study. The signals were then detected in a photodiode with single sided thermal noise density of 10 pA/Hz$^{1/2}$ and filtered by a third order Bessel low-pass filter with a bandwidth equal to 0.75 times the bit rate.

The dispersion tolerance curve are plotted in Fig. 3.5. In order to determine the dispersion tolerance, the detuning between the DML signal and the MRR was set to the value resulting in the best sensitivity in the back-to-back case and was therefore not optimised for each transmission distance. For the three analysed MRR designs, the best performance corresponds to negative values of the accumulated dispersion. The detuning tolerance is defined as the wavelength detuning range of the MRR for which the receiver sensitivity is better than -20.5 dBm (corresponding to a power penalty of 2 dB compared to the best achievable performance).

The curves corresponding to the MRRs with a coupling factor of $\kappa^2 = 0.6$, MRR1 and MRR3, show higher tolerance to negative dispersion than to positive dispersion. This effect is more perceptible in

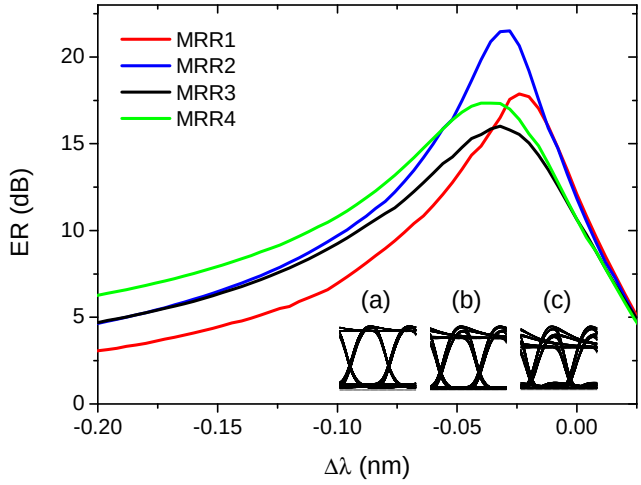

Figure 3.3: Calculated ER of the CML signal as a function of detuning between the centre wavelength of the DML spectrum and the wavelength of an MRR resonance for four different MRR designs. Insets: Eye diagrams of the signal for (a) $\Delta\lambda = -69$ pm, (b) $\Delta\lambda = -37$ pm, and (c) $\Delta\lambda = -0.4$ pm. All three eyes are obtained after filtering by MRR3.

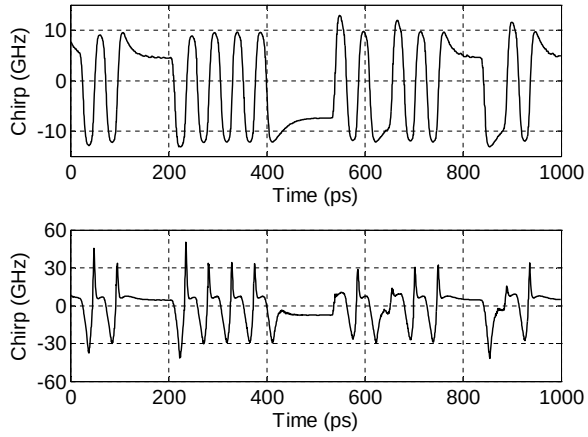

Figure 3.4: Illustration of the impact of the MRR on the modulated signal chirp. Top: Chirp of the DML signal. Bottom: Chirp after MRR3 filtering for a detuning of -85 pm.

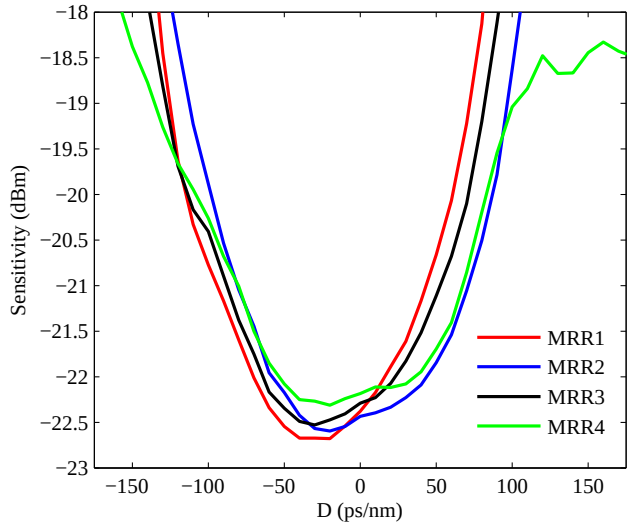

Figure 3.5: Calculated sensitivity (BER= 10^{-3}) versus accumulated fibre dispersion for four different MRR designs.

the curve for MRR1. The dispersion tolerance, as previously defined, is about 160 ps/nm in these two cases. It can also be noticed that MRR1 results in better sensitivity, about −22.7 dBm, at the optimum dispersion value, which corresponds to about −25 ps/nm. MRR2 and MRR4 also have slightly better performance over the negative dispersion range than over the positive one, even though this difference is less pronounced than for MRR1 and MRR3. The dispersion tolerances for both MRRs with coupling coefficient of 0.9 are about 170 ps/nm, with best sensitivity values at −20 ps/nm of about −22.4 and −22.2 dBm for MRR2 and MRR4, respectively. The dispersion tolerance curves are to some extent determined by the MRR dispersion profile itself, in accordance to its design. Signals filtered by the MRRs with the higher coupling coefficient experience lower dispersion with a smoother dispersion profile, as shown in Fig. 3.2. Therefore, in agreement with the simulations, a higher dispersion tolerance is expected when the MRRs with the higher coupling coefficient are used. As already stated, the dispersion tolerance curves of Fig. 3.5 have been plotted for a fixed MRR detuning, regardless of the accumulated dispersion, for each micro-ring design. However, our sim-

ulations also showed that the dispersion tolerance values as previously defined did not change significantly when the detuning of the MRR was optimised for each dispersion value.

3.3 MRR Optimisation

3.3.1 Using single ring MRRs

In order to generalise the study of the impact of the MRR design parameters (FSR and power coupling coefficient to the ring) on the dispersion tolerance of the generated signal, as well as on the detuning tolerance of the MRR, those parameters were systematically swept and the system sensitivity at a BER of 10^{-3} was evaluated using the numerical model described in Section 3.2. For the comparison of the performance over positive and negative dispersion values, the detuning between the MRR and the DML signal centre wavelength was optimised for each value of accumulated dispersion and each MRR design. MRRs with basic configuration were not considered as they do not have resonances with high extinction ratio, as shown in Chapter 2. All MRRs considered in this section are all with add-drop configuration and their round trip field transmission coefficient was taken equal to $\alpha = 0.9$.

As can be seen in Fig. 3.6, the optimum MRR design varies depending on the the dispersion accumulated in the transmission link. Fig. 3.6(a) shows the system sensitivity as a function of the MRR design parameters in the back-to-back configuration. From this graph it can be seen that the MRRs with both low power coupling coefficient and low FSR exhibit the worse performance. Fig. 3.6(b) and (c) show the system performance for accumulated dispersion values of -68 ps/nm and $+68$ ps/nm respectively. In agreement with the previous dispersion tolerance analysis, it can be noticed by comparing these two graphs that the proposed scheme results in better performance over negative dispersion values than over positive dispersion. While a system sensitivity in the range -21.5 dBm to -22.5 dBm is obtained for -68 ps/nm dispersion, the sensitivity is consistently worse than -21.5 dBm when a dispersion of $+68$ ps/nm is introduced. In this latter case, the system sensitivity is in the range -18 dBm to about -21 dBm, and the MRR design has a large impact on the performance and achievable dispersion

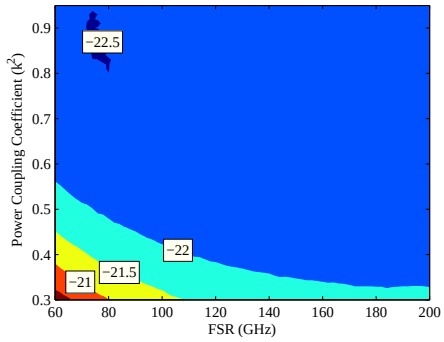

(a) Sensitivity performance (dBm) vs MRR design for D=0 ps/nm.

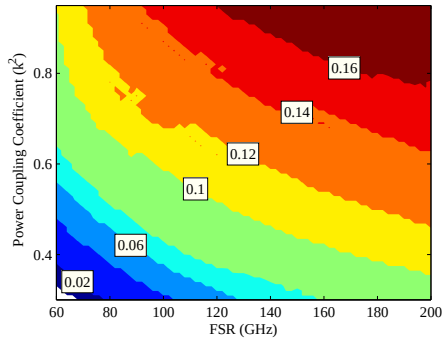

(d) Detuning tolerance (nm) vs MRR design for D=0 ps/nm.

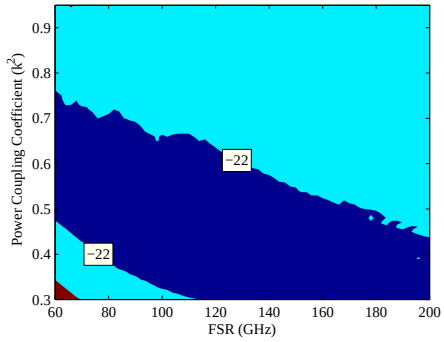

(b) Sensitivity performance (dBm) vs MRR design for D= −68 ps/nm.

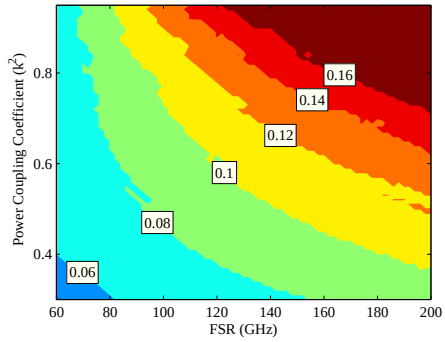

(e) Detuning tolerance (nm) vs MRR design for D= −68 ps/nm.

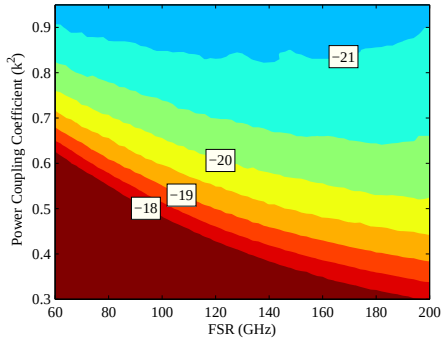

(c) Sensitivity performance (dBm) vs MRR design for D=68 ps/nm.

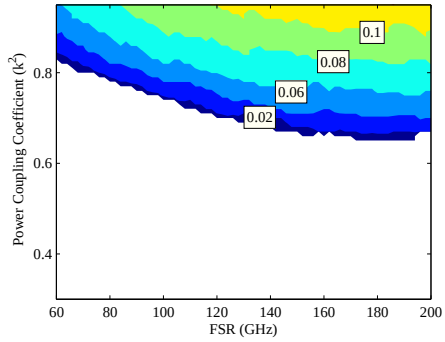

(f) Detuning tolerance (nm) vs MRR design for D=68 ps/nm.

Figure 3.6: MRR optimisation for different accumulated dispersion. Left: Sensitivity performance at a BER of 10^{-3}. Sensitivity values worse than −18 dBm have been clamped to the value of −18 dBm in the contour plots. Right: Detuning tolerance, defined as the MRR detuning range for which the sensitivity remains better than −20.5 dBm (i.e. about 2 dB worse than the best performance). The MRR design parameters space for which the sensitivity is always worse than −20.5 dBm corresponds to the area coloured in white in the contour plots.

tolerance. It can be noticed that a large FSR and a high coupling coefficient are desirable in order to reach longer transmission distances over fibres with positive dispersion.

Regarding the detuning tolerance over different accumulated dispersion values, the three graphs of Fig. 3.6(d)-(f) show similar behaviour. Regardless of the value and sign of the accumulated fiber dispersion, the larger the power coupling coefficient, the larger the detuning tolerance. This may be attributed to the fact that the MRRs with the higher coupling coefficients have a relatively low dispersion excursion, at a fixed FSR, within the detuning range. However, large coupling coefficients result in enhanced insertion loss for the MRR, as shown in Fig. 3.2. Since too high loss is clearly detrimental in short-range applications that do not resort to optical amplification, a trade-off needs to be found between the detuning tolerance and the loss. It can also be observed in Fig. 3.6(d)-(f) that the higher the FSR, the greater the detuning tolerance. However, the optimum performance cannot always be reached with a large FSR, as shown in Fig. 3.6(f). Furthermore, if the proposed scheme is employed in a multi-wavelength source making use of a DML array and a single MRR, the FSR is determined by the channel

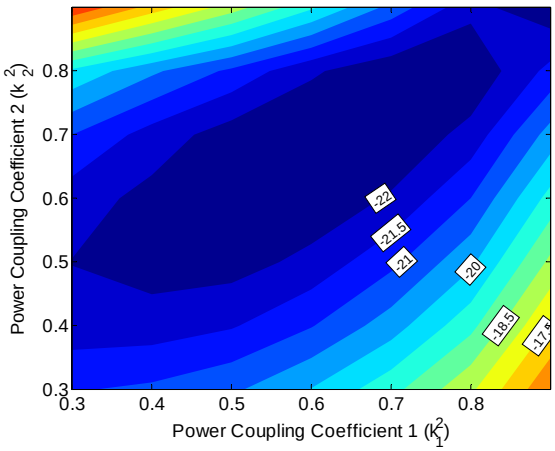

Figure 3.7: Sensitivity performance (dBm) at BER of $= 10^{-3}$ vs MRR asymmetric coupling design for D=0 ps/nm, FSR=100 GHz, round-trip loss α=0.9 and fixed detuning $\Delta\lambda = -20$ pm.

spacing and is therefore no longer a design parameter for performance improvement.

The previous simulation results were obtained with the assumption that the MRR is geometrically symmetric so that the coupling coefficient $k_1 = k_2$. In practice, due to fabrication errors, the two resulted coupling coefficient can be different. Therefore, we simulated a 100 GHz (FSR) MRR to examine the impact of asymmetric coupling coefficient. Fig. 3.7 shows the sensitivity performance as a function of different coupling coefficients. From the graph it can be seen that when the coupling coefficient of the drop waveguide is slightly higher than the one of the through waveguide, the system performance reach the best for this 100 GHz MRR. However this small coupling coefficient difference does not impact much the overall performance, when the coupling coefficient is around 0.6, within difference range of 0.1.

3.3.2 Using coupled double ring MRRs

Simulations on single ring MRR have showed that a strong suppression of the high frequency component of the signal spectra will result in a degradation of the filtered signal. Therefore, a coupled double ring resonator was simulated as a notch filter for studying the modulation enhancement, as the coupled double ring resonator can have an amplitude response as shown as in Fig. 3.8(b) when the coupling coefficient between the two rings κ_2^2 is 0.9. With a similar definition of the MRR design, coupling coefficients to the straight waveguide κ_1^2 and κ_3^2 were assumed equal. MRR1 has 100 GHz FSR, $\kappa_1^2 = \kappa_3^2 = 0.6$ and loss coefficient α =0.9. MRR2-MRR4 have the same parameters as the ones tabulated in Table 3.2 for single ring MRRs.

Fig. 3.8(a) shows the calculated ER of the filtered signal with different detuning using the four double-ring MRR designs. The use of the coupled ring resonator did not show any significant improvement. As the transfer function varies a lot wit different coupling parameters, it is more challenging to control the final outlook. Furthermore, our simulation results do not show any benefit for the case when κ_1^2 and κ_3^2 are different. However it is very difficult to make 2 strictly identical rings in practice. Therefore, single ring MRRs are more promising in practice than the coupled ring MRRs for the proposed transmitter design.

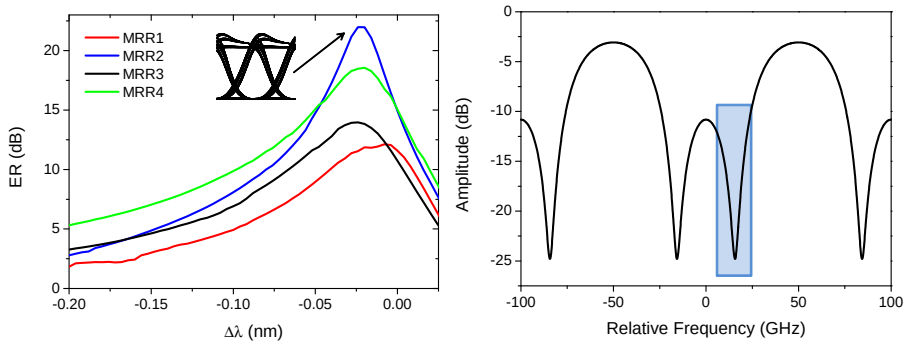

(a) **(b)**

Figure 3.8: (a): Calculated ER of the CML signal as a function of wavelength detuning. Inset: Eye diagram of the signal for −25 pm detuning filtered by MRR2. (b): Transfer function of the coupled double-ring MRR (MRR2) with FRS=100 GHz and κ_2^2 =0.9 used for simulation. The detuning is defined as the difference between the centre wavelength of the DML spectrum without modulation and the wavelength of the notch highlighted on the MRR transfer function

3.4 Experimental Demonstration Using DFB Laser Diode

3.4.1 Experimental setup

In this section, an experimental proof-of-concept demonstration of the scheme using a directly modulated DFB laser and a custom-made silicon MRR is reported. Fig. 3.9 shows the setup used for the experimental demonstration. A commercially available DFB (NEL model NLK5C5EBKA), designed for operating at 10 Gbit/s, was directly modulated at 40 Gbit/s by a non return-to-zero (NRZ) signal with bias at 75 mA and peak-to-peak voltage of 2.5 V. The high bias current allowed the adiabatic chirp to be dominant over the transient chirp. The modulation data was a pseudo-random binary sequence of length $2^{11} - 1$. The modulated signal was then coupled to the MRR and collected again via tapered fibres. An erbium doped fibre amplifier (EDFA) was used to compensate the free-space coupling loss, followed by a 2-nm optical bandpass filter (OBPF) for noise reduction. The filter bandwidth was chosen to be wide enough to avoid introduction of any extra filtering which could impact the result. The amplification requirement would

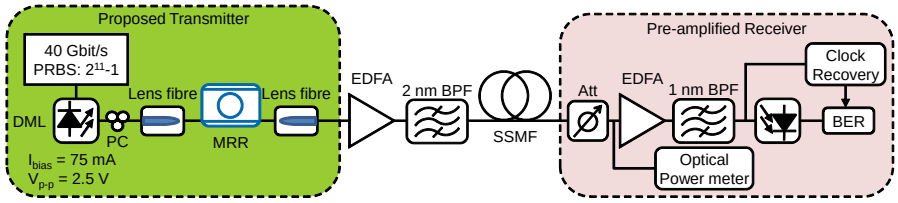

Figure 3.9: Experimental setup for CML generation, transmission and detection.

obviously be waived with hybrid integration of the directly modulated laser source with the silicon-on-insulator chip. As the MRR chip is polarisation sensitive, the polarisation of the signal into the MRR was controlled by a polarisation controller (PC). At the output of the MRR, the signal was boosted and launched into standard SMF of variable lengths prior to detection, or connected directly to the pre-amplified receiver (back-to-back).

Different MRR designs were used in the experimental demonstrations. They were all fabricated on a silicon-on-insulator platform by electron-beam lithography followed by reactive ion etching according to the process described in details in [56].

3.4.2 Experimental results

First, a MRR with 200-GHz FSR and a design Q-factor of 3300 (κ^2 ~0.6), as shown in Fig. 2.7, was used. This MRR will henceforth be referred as 200-GHz MRR1. The DML was then thermally tuned to the short wavelength side of a MRR resonance (detuning of ~ 0.17 nm), as shown in Fig. 3.10. These spectra illustrate how the MRR resonance is used to filter the signal longer wavelengths, i.e. the wavelengths corresponding to the zeros. Corresponding eye diagrams at the output of the DML and after the MRR are also represented in Fig. 3.10. In agreement with the simulations, the eye diagram was significantly opened thanks to the MRR and the zero level was largely suppressed, at the expense of some overshoot on the one level.

Fig. 3.11 shows the BER performance of the back to back DML signal and that of the CML signal at the MRR output as well as after different standard SMF lengths. Fig. 3.11 (a)-(d) shows the eye diagrams after transmission over 1 to 4.5 km SMF respectively. The ISI

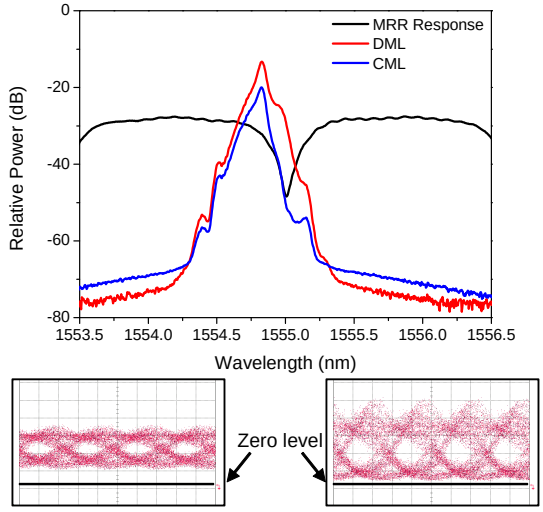

Figure 3.10: Characterisation of the signal generated from a DML modulated at 40 Gbit/s, using a 10 Gbit/s DFB laser diode, followed by an MRR with 200-GHz FSR and design Q-factor of 3300. Top: signal spectra before and after the MRR plotted together with the MRR through port response. Bottom left: eye diagram of the 40-Gbit/s signal at the DML output, taken with -9 dBm received power. Bottom right: eye diagram of the CML signal at the MRR output, taken with -18 dBm received power.

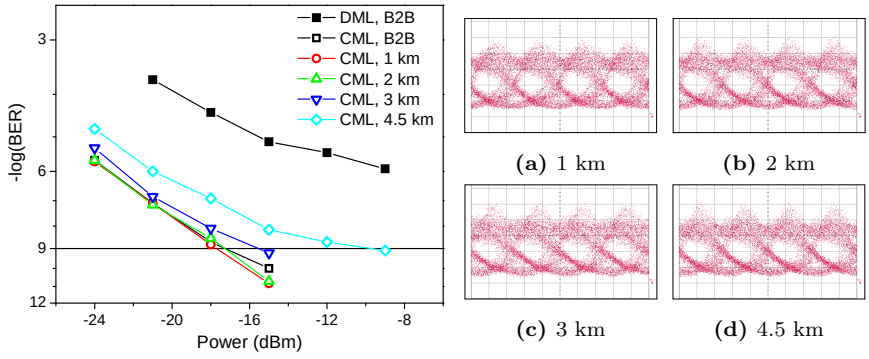

Figure 3.11: Performance of the signal generated by the proposed transmitter using a DFB laser diode. Right: BER performance at the DML output (DML, B2B), after the MRR with 200-GHz FSR and design Q factor of 3300 (CML, B2B), as well as after different lengths of SSMF; Left: optical eye-diagrams after (a) 1 km (b) 2 km (c) 3 km and (d) 4.5 km of SSMF, taken at -18 dBm received power.

introduced by the positive dispersion in the SMF clearly distorted the eyes. The BER improvement due to the MRR filtering is evident. The sensitivity at 10^{-9} of the filtered signal was about -17.2 dBm whereas the DML signal without MRR filtering did not reach error-free performance. An error floor of 1.2×10^{-6} was obtained for an average input power of -9 dBm. The signal was transmitted up to 3 km with a penalty around 1.5 dB. Besides, the filtered signal still remained error-free even after transmission over 4.5 km uncompensated standard SMF. For some short-reach networks, for example in avionic networks, in-building Ethernet networks and interconnect networks, this transmission distance is sufficient.

The dispersion tolerance was also evaluated over negative dispersion values. For this investigation the CML signal was launched into different lengths of dispersion compensation fibre (DCF). The measured dispersion tolerance curve is shown in Fig. 3.12. The range of the dispersion with error-free performance is from -50 to 80 ps/nm. The curve is asymmetric and, unlike in the simulations, a larger positive-dispersion tolerance was obtained. The reason for this difference is still not understood. Fig. 3.12 (a)-(d) also shows the eye-diagrams of the signal transmitting through different lengths of DCF. From the eyes and the BER curve,

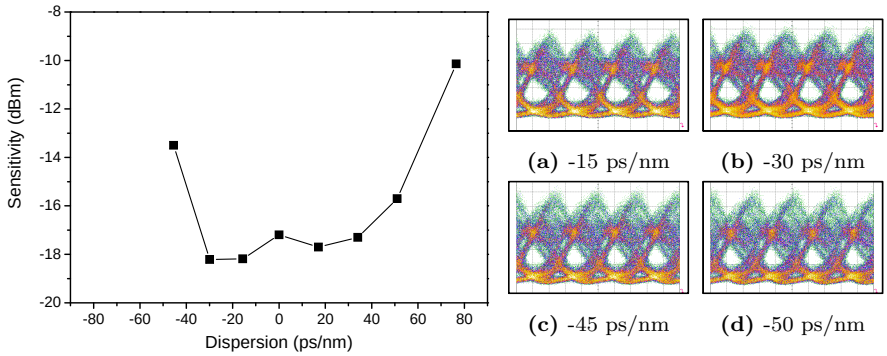

Figure 3.12: Dispersion tolerance. Right: signal dispersion tolerance to both negative and positive dispersion values calculated according the the fibre for transmission. The sensitivity is the received signal power for error-free (BER= 10^{-9}) performance. Left: optical signal eye-diagrams when transmitting with negative dispersion (a) -15 ps/nm (DCF 150 m), (b) -30 ps/nm (DCF 300 m), (c) -45 ps/nm (DCF 450 m) and (d) -50 ps/nm (DCF 500 m)

it did show, not obviously though, that within $0\sim -30$ ps/nm the signal performance was slightly improved by the introduction of negative dispersion, which is similar to the simulation results shown in Fig. 3.5.

The detuning tolerance was also analysed experimentally. It was measured in a back-to-back configuration and after 2 km SMF. In this investigation the laser wavelength was thermally tuned. As mentioned earlier in this section, it was ensured that no additional chirp management originated from the OBPFs present in the set-up. The BER was measured at a fixed average received power of -15 dBm. As shown in Fig. 3.13(a), the optimum detuning was at about -0.17 nm. As mentioned earlier, the detuning was defined as $\Delta\lambda = \lambda_{\text{laser}} - \lambda_{\text{resonance}}$, where λ_{laser} is the centre wavelength of the DML spectrum without modulation. With this detuning value of -0.17 nm, the ER of the CML signal was enhanced since the MRR through port attenuated the red-shifted zeros, as depicted in Fig. 3.13(c). Although the adiabatic chirp of the zeros was further suppressed, as shown in Fig. 3.13(d), when the laser was tuned closer to the resonance, the CML signal had a larger overshoot and smaller eye opening, resulting in poorer BER performance. When the DML signal was detuned further away from the resonance, Fig. 3.13(b), the signal just went through the MRR with weaker chirp suppression and the eye diagram did not show any improvement. The BER performance confirms the existence of an optimum detuning between the DML spectrum and the MRR resonance. The BER performance of the CML signal after 2 km transmission over standard single mode fibre (SSMF) shows similar detuning tolerance, as can be seen in Fig. 3.13(a). These experimental results agree with the simulations where the optimum detuning was seen not to change significantly with the amount of accumulated dispersion.

Two other MRRs, one with an FSR of 200 GHz and a Q-factor of 3900 (referred as 200-GHz MRR2), and another one with an FSR of 100 GHz and a Q-factor of 6800, were also assessed in order to evaluate the flexibility of the proposed scheme. The optimum detuning did not change significantly despite using MRRs with slightly different transfer functions, as shown in Fig. 12. The optimum detuning continued being ~ -0.17 nm for the three analysed MRR, as shown in Fig. 3.14. With the 200-GHz MRR2, error-free transmission over 2 km SSMF was achieved, whereas the signal generated by the 100-GHz MRR achieved error-free

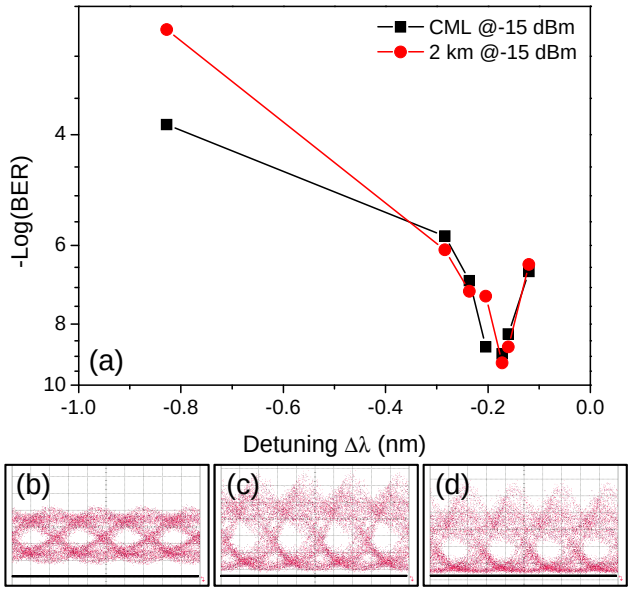

Figure 3.13: Detuning results: (a) Detuning tolerance comparison with and without transmission using 200-GHz MRR1; (b) Eye diagram after the MRR with detuning of −0.3 nm; (c) Eye diagram with detuning of −0.17 nm; (d) Eye diagram with detuning of −0.1 nm.

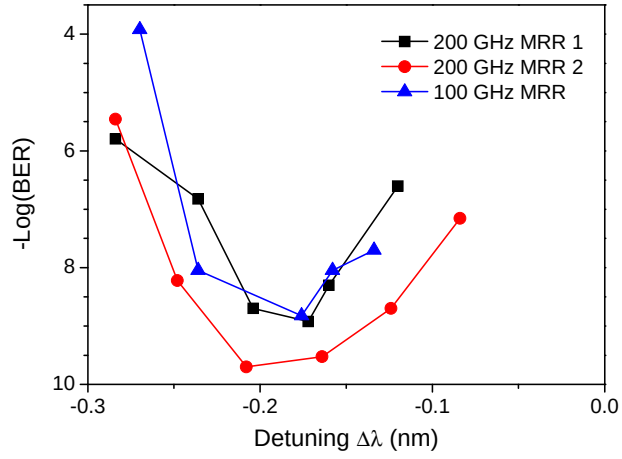

Figure 3.14: Detuning tolerance comparison of three different MRRs.

transmission for less than ∼1 km. This reduced dispersion tolerance of the MRR with the smaller FSR is in agreement with the observations of the numerical study in Section 3.3.

We have experimentally demonstrated the use of a silicon MRR to enhance the modulation speed of DML-based systems for short-range applications. In the next section, the experimental demonstration of modulation speed enhancement in a VCSEL is presented, in order to verify the feasibility of the proposed scheme for VCSEL-based transmitters.

3.5 Experimental Demonstration Using VCSEL Diode

3.5.1 Experimental setup

The experimental setup using VCSEL is very similar to the previous section. The VCSELs used in the experiment were provided by Prof. Amann from the Walter Schottky Institut (WSI) of the Technische Universität München (TUM) [57], and they are not packaged devices. A piece of cleaved SSMF was used to couple the light out. The maximum emitting power was previously characterised at TUM and was about 1-2 dBm. However, if the cleaved SMF was placed close to the VCSEL to increase the coupling efficiency, reflections were also higher resulting in noisy lasing. Therefore, the maximum power coupled out of the VCSELs without the noise arising from reflections, was only about −4 dBm with 9 mA bias current.

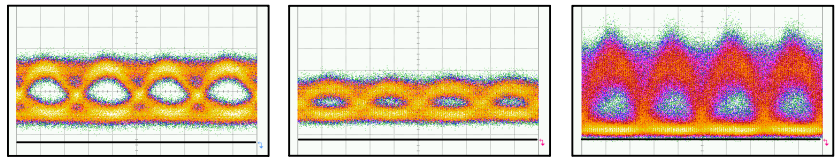

(a) (b) (c)

Figure 3.15: Eye diagrams at the output of a VCSEL modulated at 19.906 Gbit/s and after filtering by a custom-made 100 GHz FSR silicon MRR. (a) The back-to-back output of the VCSEL with −5 dBm and (b) −18 dBm power into the EDFA, (c) Eye after filtering by the MRR, −18 dBm into the EDFA.

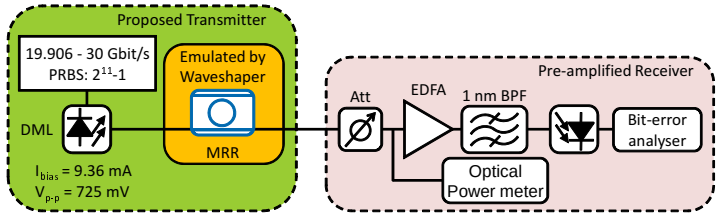

Figure 3.16: Experimental setup for CML generation using VCSEL and direct detection by a pre-amplified receiver.

The VCSELs are emitting around 1525-1530 nm at room temperature, depending on the bias current. In order to perform the proposed transmitter scheme, a high bias current is a requirement in order to allow the adiabatic chirp to dominate over transient chirp. Meanwhile, the custom-designed MRR could not be tuned. Moving the laser spectrum to match the MRR by tuning the bias current was the only way. However the 1530 nm wavelength range is below the operation limit of EDFAs, which offer virtually no gain while adding amplified spontaneous emission (ASE) noise.

Fig. 3.15 (a) and (b) are examples of a back-to-back VCSEL output at different power levels into the EDFA. The EDFA offered a small gain, but when the signal is as weak as −18 dBm, the added ASE noise closed the eye entirely. The reason of checking the EDFA behaviour is that, due to the lossy coupling to the MRR by tapered fibre and other components used in the setup, only −18 dBm of power are left for detection. Fig. 3.15(c) shows the eye after the MRR with maximum received power of −18 dBm. It is obvious that the MRR has been performing as expected to open the eye, but it was too weak to detect.

Therefore, a WaveShaper (a product of Finisar® [58]) was used to emulate the MRR as the MRR response can then be moved to any wavelength. The experimental setup is shown in Fig. 3.16. The VCSEL can then be biased at any current. In the following experiment, the VCSEL was biased at 9.36 mA. The centre emission wavelength of the VCSEL at this bias current was 1530 nm. For this VCSEL, the threshold current is 1.24 mA and the bias current corresponding to maximum emission power before roll-off is 12.25 mA. The maximum 3-dB modulation bandwidth (for a bias of 12.25 mA) was measured to be 17.60 GHz at 20 °C.

3.5.2 Experimental results

The VCSELs are very often modulated with high peak-to-peak voltages (600-800 mV, or even higher up to 1 V), so that the ER can be large. We compared the BER performance of the VCSEL when driving at different peak-to-peak voltages V_{pp}. With a modulation of 19.906 Gbit/s, the sensitivity for error-free operations (BER= 10^{-9}) was -18 dBm with V_{pp} =410 mV and -24.5 dBm with V_{pp} =725 mV. The current of the photodiode was kept constant at 1.5 mA as the measured sensitivities were different when the photodiode current varies. This should not happen in the real receiver because it is due to the discrete bias voltage at the error-analyser. If keeping the photodiode current at 1 mA, the sensitivity with V_{pp} =725 mV will drop 1.5 dB, to -23 dBm. It can be seen in Fig. 3.17 and Fig. 3.18.

Modulation enhancement at 19.906 Gbit/s

First of all, a low modulation index V_{pp} =410 mV was used to modulate the VCSEL at 19.906 Gbit/s. The VCSEL emitted at 1530 nm with only 9.36 mA bias current, as shown as in Fig. 3.17. The side mode was very strong, with only 20 dB side-mode suppression ratio. With 410 mV modulation, the spectrum was shifted towards longer wavelengths. The measured back-to-back sensitivity was -18 dBm.

As a WaveShaper was used to emulate the MRR, we needed to verify first that the WaveShaper did perform as expected. The back-to-back VCSEL output was sent to the WaveShaper and an all-pass type of filter with 0.5 THz bandwidth was used to filter the signal. It was expected that no impact should be introduced by the WaveShaper and the BER measurement confirmed it, as shown in Fig. 3.17. The BERs at different received powers with and without the WaveShaper were exactly the same.

When emulating MRRs, the maximum suppression which can be achieved by the WaveShaper is 35 dB. We used an amplitude response calculated from a 100-GHz FSR MRR with coupling coefficient κ^2 =0.9 (MRR2 in the simulation). As shown in Fig. 3.2(a), the maximum attenuation at the resonance is within 30 dB. As shown in Fig. 3.17, the VCSEL did perform error-free at 19.906 Gbit/s. By applying a MRR response at the output of the VCSEL, the sensitivity can be improved

by 10 dB, to −28 dBm. The eye diagrams in Fig. 3.17 showed a significant improvement. The photodiode current was kept at 1.5 mA for BER measurement.

The peak-to-peak voltage was then increased to 725 mV, the spectrum of the signal changed as in Fig. 3.18(a). Two frequency peaks appeared, with each corresponding to the adiabatic chirp associated with "0"s and "1"s. The higher modulation voltage improved the DML sensitivity to −24.5 dBm, as shown as in Fig. 3.18. However, due to insufficient signal power to obtain the BER of the signal after MRR with low received power, the photodiode current was decreased down to 1 mA. As presented earlier, the back-to-back sensitivity was measured to be −23 dBm, 1.5 dB difference. The back-to-back eye-diagram in Fig. 3.18(c) shows much less zero level power compared to Fig. 3.17(c). Nevertheless, after the MRR with the same parameter, the signal still showed 8 dB sensitivity improvement, to −31 dBm.

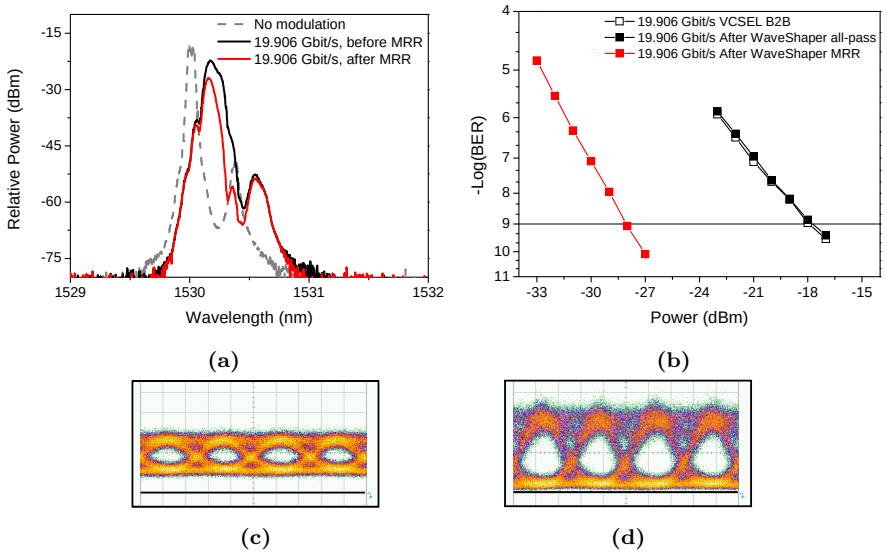

Figure 3.17: VCSEL performance at 19.906 Gbit/s with V_{pp} =410 mV. (a) Signal spectra before and after the MRR, (b) BER measurement, Signal eye-diagram (c) before and (d) after the MRR. Eyes were recorded with a received power of −23 dBm.

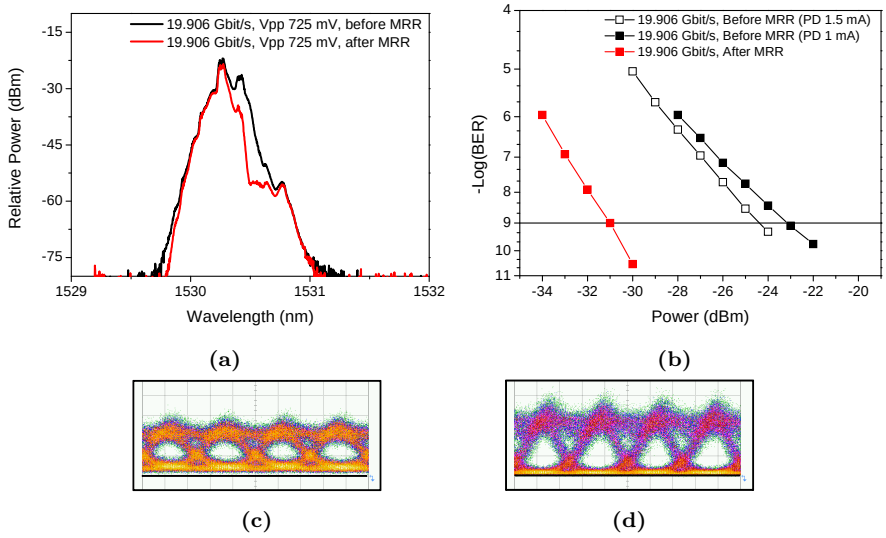

Figure 3.18: VCSEL performance at 19.906 Gbit/s with V_{pp} =725 mV. (a) Signal spectra before and after the MRR, (b) BER measurement, Signal eye-diagram (c) before and (d) after the MRR. Eyes were recorded with a received power of −28 dBm.

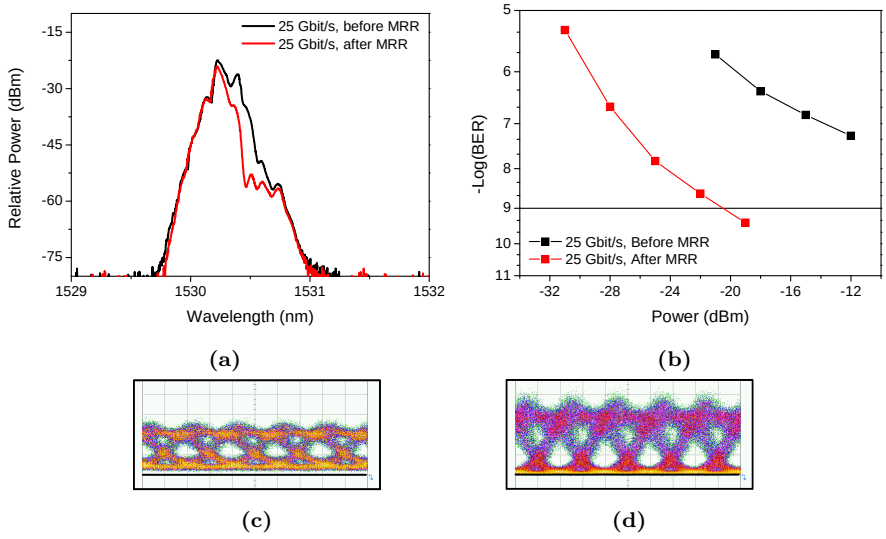

Figure 3.19: VCSEL performance at 25 Gbit/s with V_{pp} =725 mV. (a) Signal spectra before and after the MRR, (b) BER measurement, Signal eye-diagram (c) before and (d) after the MRR. Eyes were recorded with a received power of −18 dBm.

Modulation enhancement at 25 Gbit/s

Modulating the VCSEL at 25 Gbit/s with a peak-to-peak voltage of 725 mV, the VCSEL did not perform error-free, as seen in Fig. 3.19. At -15 dBm received power, the BER was higher than 10^{-7}. By filtering by the same MRR, the performance was improved to be error-free with a sensitivity of < -20 dBm.

The VCSEL was working at room temperature without a temperature controller. Its performance and the performance after the MRR were stable during the entire measurement.

Modulation enhancement at 30 Gbit/s

We tried to push the modulation speed to 30 Gbit/s, nearly doubling the 3-dB modulation bandwidth of the VCSEL, and the bias was still kept at 9.36 mA. The VCSEL could not offer a good eye at all, as can be seen in Fig. 3.20, with a BER of 1.9×10^{-4} at -14.2 dBm received power. With the MRR, the performance was still not error-free, however it has been improved to 2.4×10^{-6}. This result could be improved if MRR detuning is optimised, and higher bias current is used.

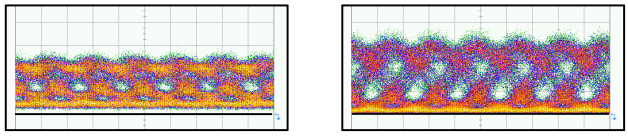

Figure 3.20: Eye diagrams when the VCSEL was modulated at 30 Gbit/s. Left: before the MRR. Right: after the MRR. The received power was -14.2 dBm and the photodiode current was 1 mA.

3.6 Discussion

It was noticed in Section 3.5 that the proposed method enhanced the performance with a relatively high peak-to-peak modulation, i.e. higher modulation index. Having higher modulation index can result in a performance improvement. As presented in Section 3.2, the operation principle of the proposed scheme is to allow the adiabatic chip dominating over the transient chip as long as there is sufficient chirp between "0"s

and “1”s so that off centred filtering can be used. It would be interesting to simulate the DML with higher modulation index and try to find out the the optimum modulation index and optimum amount of adiabatic chirp before filtering to achieve the best CML performance.

The DML model described in Section 3.2 was used to simulate the DML with higher modulation index filtered by the same MRR designs in order to compare with the simulation results obtained previously. Similar to our experiment on VCSELs, the bias current was 75 mA, while the peak-to-peak current was increased from 50 mA to 75 mA, which results in a better ER of 3.3 dB. The back-to-back eye-diagram can be found in Fig. 3.21(a). Compared to the eye in Fig. 3.1, the zero level clearly has been moved down. The signal has 18 GHz adiabatic chirp difference between “0”s and “1”s. We compared the DML spectra resulting from the two peak-to-peak current values, as shown in Fig. 3.21(b). The spectrum associated with 75 mA peak-to-peak current shows similar behaviour compared to the VCSEL spectrum in the experiment, i.e. the presence of two peaks. The same MRR designs, MRR1-4, were used to perform the filtering. Fig. 3.21(a) shows the calculated ER with different MRR designs. For all four MRRs, the ER was improved compared to the one shown in Fig. 3.3. The eye-diagram after the MRR in Fig. 3.21(a) has less overshoot and well-suppressed zero level.

When increasing the peak-to-peak current to 100 mA, no ER improvement was noticed compared to using 50 mA as peak-to-peak current. Therefore, a trade-off between the modulation index and the adiabatic chirp could be found to achieve the optimum performance of the proposed method.

Electrical pre-emphasis pulse shapinp was used to cost effectively increase the modulation bandwidth of a VCSEL [59]. It utilises multiple modulation levels within 1-bit to compensate the relaxation oscillation and transient chirp so that the signal performance can be improved. This method can help to reduce the transient chirp and could be used together with our proposed method. Therefore, it could be interesting to combine these two method to see whether it is possible to achieve even better modulation enhancement.

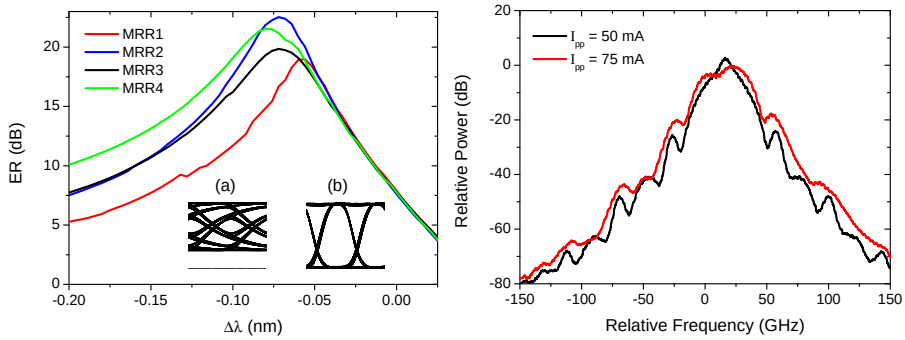

Figure 3.21: Left: Calculated ER of the CML signal as a function of detuning between the centre wavelength of the DML spectrum without modulation and the wavelength of an MRR resonance for four different MRR designs. Inset: Eye diagrams of (a) the back-to-back signal and (b) filtered by MRR3 with 72 pm detuning. Right: laser spectra with 50 mA and 75 mA peak-to-peak modulation current.

3.7 Conclusion

We have comprehensively analysed the use of a silicon MRR in order to enhance the modulation speed of DML-based systems for short-range applications. The influence of the MRR design on the system performance has been assessed numerically. Modulation speed enhancement from 10 Gbit/s to 40 Gbit/s has been demonstrated in a commercial DFB laser. Both dispersion and detuning tolerances have been determined in accordance with the MRR design. Moreover, 40 Gbit/s transmission over 4.5-km SSMF using a DML designed to operate at 10 Gbit/s has been experimentally demonstrated. The detuning tolerance has also been evaluated experimentally.

As the proposed scheme is particularly interesting for its integratability, it is very important to access the feasibility of applying the scheme on a VCSEL. We have also demonstrated experimentally that a VCSEL with less than 17.6 GHz 3-dB modulation bandwidth can be operated at 25 Gbit/s error-free with a sensitivity of −21 dBm, thanks to off-centred filtering by the MRR. There is still room for further improvement if biasing the VCSEL at higher current. Performance improvement of 10 dB with V_{pp} =410 mV and 8 dB with V_{pp} =725 mV has also been demonstrated at 19.906 Gbit/s, which can bring the sensitivity as good as −31 dBm.

Therefore the proposed scheme is a promising solution for short-range applications thanks to its reduced footprint and potential for integration. The proposed transmitter would be a ultra-compact and cost-efficient solution for future short-range applications. For the future, it might be possible to combine this proposed transmitter together with pre-emphasis technology to achieve more modulation enhancement.

Chapter 4

All-Optical Protection Switching

4.1 Motivation

As the bandwidth of most deployed optical links exceeds 10 Gbit/s, any outage in even just a millisecond will cause the loss of tens of megabytes of data, far beyond the tolerance of any reliable network [18]. With wavelength division multiplexing (WDM) technology, as every single optical fibre carries a number of optical channels or wavelengths, the consequent data loss due to any network failure is tremendous. Therefore the network survivability is of particular importance [60].

Protection switching is a key technique to ensure survivability against outages in optical networks by providing an alternative path to carry the traffic in case of link failure, thus providing high reliability and availability of the communications [61, 62]. Traditionally, some fault detection mechanisms are implemented in the network, which detect and report a failure to the network management system. The protection mechanism is then triggered from the control plane of the network management system, possibly resulting in a relatively long delay to establish the protection path. For instance, in widely deployed SONET/SDH networks, the protection switching time is typically of the order of $\sim$50 ms [18, 63] exclusive of an allowed additional time of 10 ms [18] for failure detection. Depending on the type of network and application, failure detection can be achieved by power, bit-error-ratio or polarisation monitoring [64] or

even optical time-domain reflectometry (OTDR) [65].

A wide range of switching mechanisms have been considered for protection applications with various achievable switching time and extinction ratio, as well as different levels of technology maturity and cost [66]. For many practical applications, the switching time is still limited to milliseconds. For example, typical protection switching times reported in WDM passive optical networks (WDM-PONs) experiments are of the order of 1 to 10 ms [67, 68].

Other methods exploit the fast wavelength switching of dedicated semiconductor laser structures followed by wavelength routing to guide the signal to the protection path. Even though fast tuning of advanced lasers has been demonstrated, the control of the currents from the control plane results in still relatively long switching times. For instance, a protection switching time of 8 ms was recently demonstrated in [69]. Therefore the establishment of the protection path is a relatively slow process compared to achievable optical switching speeds. One way to reduce the protection time into the nanosecond scale or below is to enable the establishment of the protection path to be triggered directly in the optical domain.

Therefore a new all-optical protection switching (AOPS) scheme is desired, in which failure detection and protection trigger are all implemented on the optical layer so that no upper layer mechanism is required. For the very first time, this problem is addressed here. We proposed such an all-optical protection switching scheme relying on a bistable laser diode as a continuous wave source at the transmitter. Under normal operation, the laser diode emits at its nominal wavelength and the modulated signal is routed to the fibre link used for normal operation. If a periodic probe pulse originating from the far end of the link does not reach the laser due to a link failure, the bistability will trigger the light emission to the protection wavelength and hence the signal will be routed to the protection path. We experimentally demonstrated the proposed scheme successfully, with reported protection switching time of less than 200 ps. The widely opened eye diagrams show good link performance at both 10 Gbit/s and 40 Gbit/s data modulation. Optical control pulses of 50 ps duration and less than a half pJ pulse energy are used for triggering the establishment of the protection path. Since there is no upper layer mechanism required, the protection can be performed

ultra-fast.

This chapter is structured as follows:

First of all, the bistable laser diode used for realising the proposed protection scheme is described in Section 4.2. We experimentally demonstrated, for the first time, wavelength flip-flop operation with wide wavelength tunable range in a single laser structure. Then, in Section 4.3, the operation principle of the proposed protection switching scheme is illustrated, and the experimental demonstration and system evaluation are presented. Section. 4.4 presents a discussion over the advantages and limitations of the proposed method, as well as the alternative implementations.

4.2 All-Optical Flip-Flop Operation in a MG-Y Laser Diode

4.2.1 Overview on all-optical flip-flops

All-optical flip-flops (AOFFs) are key signal processing building blocks for optical networks in order to implement optical memory and optical logic circuits that may be used to overcome the bandwidth bottleneck of electronics in some switching applications [70]. These AOFFs can be power bistable [71–73], polarisation bistable [74, 75] and wavelength bistable [76–80]. Liu et al. reported a micro-disk laser structure which can emit light clockwise or counter-clockwise depending on the input [81]. In particular, wavelength bistability is attractive in applications where optical wavelength selective components are subsequently used to selectively route signals depending on their wavelength, such as in some proposed packet switch architectures [82].

Being able to achieve wavelength bistability in typical laser structures conventionally used for telecommunication applications would represent a tremendous advantage in view of practical implementations. Huybrechts et al. demonstrated all-optical flip-flop operation using set and reset pulses on the same wavelength in a standard tunable distributed Bragg reflector (DBR) laser diode and predicted that the principle can be extended to other laser diodes with long cavities [79]. All-

optical flip-flop in a DBR with two control pulses on different wavelengths injection locking the laser onto the side-mode was demonstrated and analysed [78, 83]. However, no wavelength flip-flop in a single laser structure with wide wavelength-tunable capability has ever been reported.

In the following sections, the principle of all-optical wavelength flip-flop (AOWFF) operation in DBR laser structures and a brief introduction to modulated grating Y-branch (MG-Y) laser are presented. Static bistable characteristics of MG-Y laser diodes are described. AOWFF operation was experimentally demonstrated on three different wavelengths. As more lasing windows of the laser were found to have the similar behaviour, the AOWFF operation in a MG-Y laser structure is believed to be with wide wavelength tunable range.

4.2.2 Operation principle and MG-Y laser structure

Among many varieties of laser structures, distributed Bragg reflector (DBR) lasers have Bragg reflectors formed along a passive waveguide section outside the active region, which act as wavelength dependent mirrors. Their reflectivities are at maximum for those wavelengths that match the Bragg condition, $\lambda_B = 2n_e\Lambda$, where Λ is the grating period and n_e is the effective refractive index. The longitudinal mode which has the highest gain and sees the largest Bragg reflectivity will dominate and become the primary lasing mode. However this single-mode or single-frequency operation is a relative term, as other modes still exist even though with much less power. Therefore the side-mode suppression ratio is used to evaluate the purity of the single-frequency operation. It is defined as the ratio of the output power in the primary lasing mode comparing to the nearest longitudinal mode.

The tunability is one of the advantages for which the DBR lasers are of great importance. For a most simple two-section tunable DBR laser, apart from the active section and the passive grating section, a passive section in-between the other two sections, allows independent mode phase control. By applying a small current or voltage to the grating section, its refractive index changes and the central wavelength, i.e. the wavelength with maximum reflectivity, of the grating moves. Therefore different longitudinal modes can be selected, which is referred

to as mode hop tuning [84]. By applying a current or voltage to the phase section, the refractive index change will shift all the longitudinal modes of the cavity. The lasing wavelength will therefore move slightly. In this way, the DBR laser can be tuned to a broad range of wavelengths.

If the phase current is tuned so that two modes are both in the reflectivity peak, bistable operation can be obtained. The bistability of the laser can be described by a two-modes coupled lasing. The basic nonlinearity, the gain saturation, is responsible for the wavelength bistability, in which the energy is switched in between two modes. Coupled-mode theory can be used to describe the bistable behaviour [85]. The coupled equations can be expressed as:

$$\frac{dI_1}{dt} = g_1 I_1 \left[1 - S_1 I_1 - C_{12} I_2\right] , \tag{4.1}$$

$$\frac{dI_2}{dt} = g_2 I_2 \left[1 - S_2 I_2 - C_{21} I_1\right] , \tag{4.2}$$

where $I_{1,2}$ refers to the intensity of the two modes, S_1, S_2 are the self-saturation coefficients of the two modes and C_{12}, C_{21} are the cross-saturation coefficients, respectively. The wavelength bistable condition is simply $C_{12}C_{21} > S_1S_2$ [85]. With the presence of a suitable saturable absorption region where the self-saturation coefficients of the gain can cancel with the one of the absorption region to reduce S_1S_2, this bistable condition can be satisfied [85]. The phase region can act as the saturable absorption region. The switching time, because of the gain saturation effect, is believed to be limited by the photon lifetime, which could be ultra-fast.

Meanwhile, when the laser is operating at high intensity radiation ($\geq 10^4 W/cm^2$), nonlinear effects in the semiconductor laser will lead to another asymmetric mode interaction, where the longer wavelength mode of two neighbouring longitudinal modes dominates [86]. This effect is called "Bogatov effect". The Bogatov effect occurs at small spectral distances, no larger than about 10^{11} Hz. This asymmetry around the lasing frequency will introduce a hysteresis in the tuning characteristic, which can be used to achieve bistable lasing. For in-plane DBR lasers, the cavity length is typically a few hundred micrometers. For example, if the gain medium of a 1550 nm laser has an effective refractive index of 3.5, and cavity length of 500 μm, the mode spacing will be about

0.68 nm, within the range of Bogatov effect[1].

MG-Y laser stucture

As an alternative design of a DBR laser, a modulated grating Y-branch (MG-Y) laser, as illustrated in Fig. 4.1, consists of a gain section, a multi-mode interferometer (MMI) section and two Bragg multi-peak reflectors both on the same side of the gain section [87]. The light generated in the gain section will pass through the MMI so that it will be split and coupled into the two multi-peak reflectors. A common phase section between the gain and the MMI section is used to align the cavity mode. A differential phase section can be placed in front of one of the multi-peak reflectors [87].

Similarly to sampled grating distributed Bragg reflector (SG-DBR) lasers, the MG-Y laser uses the Vernier effect to achieve wide wavelength tunability with the two multi-peak reflectors. Compared to the SG-DBR lasers, MG-Y lasers offer advantages in term of output power variation when tuned, since their design avoids the output light passing through the reflectors where free carrier absorption happens. Therefore, they are more commonly used in real transmitters than 2 or 3-section DBR lasers [88].

The MG-Y laser used in our experimental demonstration is a commercially available device manufactured by *Syntune*. In contrast with the design in [87], the laser has no differential phase section. Such a section is indeed not required if no significant asymmetry between the

[1]Mode spacing $\Delta\lambda = \frac{\lambda_0}{2nL\cos\theta}$, where λ_0 is the laser emitting wavelength, n is the effective refractive index of the gain medium, L is the cavity length and consider $\cos\theta = 1$ for a laser cavity.

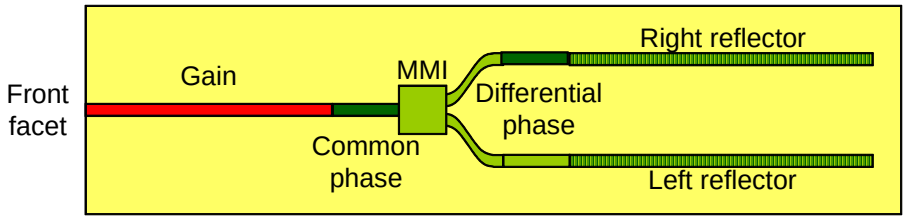

Figure 4.1: Design structure of a MG-Y laser.

2 arms in the Y-branch is introduced due to fabrication [89]. Fig. 4.1 shows the picture taken under microscope of the MG-Y laser chip used in our experiment kindly provided by Prof. G. Morthier from the Department of Information Technology at Ghent University. Different sections were marked in the picture.

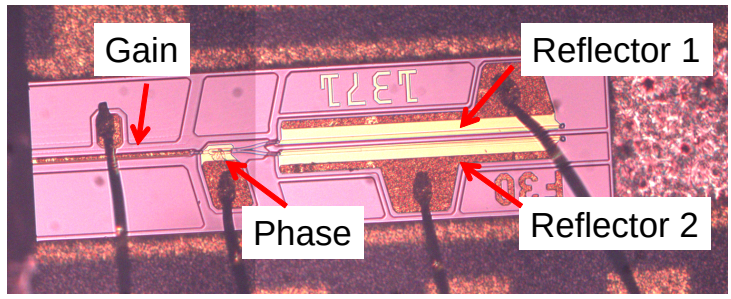

Figure 4.2: A view of the MG-Y laser used in our experiment.

4.2.3 Static hysteresis characterisations

The current injected to the gain section was set to 100 mA throughout this work. Changing the currents applied to the reflectors will change the lasing wavelength of the MG-Y laser. Under some reflector currents operating conditions, wavelength bistability can be obtained by varying the phase current, as shown in Fig. 4.3(a) for a lasing wavelength of about 1554 nm. The bistable window lies between 2 mA and 5.6 mA phase current, values at which the lasing wavelength jumped, as seen in Fig. 4.3. While changing the phase current to the same direction (increase or decrease), the cavity modes were therefore moved relative to the reflector window and the side mode power increased. At the edge of the bistable window, the mode hopped from the primary mode to the side mode, as shown in Fig. 4.3(b). In order to achieve flip-flop operation under optical control, a phase current lying in the middle of the bistable window should be chosen. In our experiment, a phase current of 3.6 mA is chosen.

For the single-mode lasing quality, the lowest side-mode suppression ratio ($>$ 40 dB) was measured just before the laser toggled lasing state. At the phase current of 3.6 mA, the side-mode suppression ratio is better,

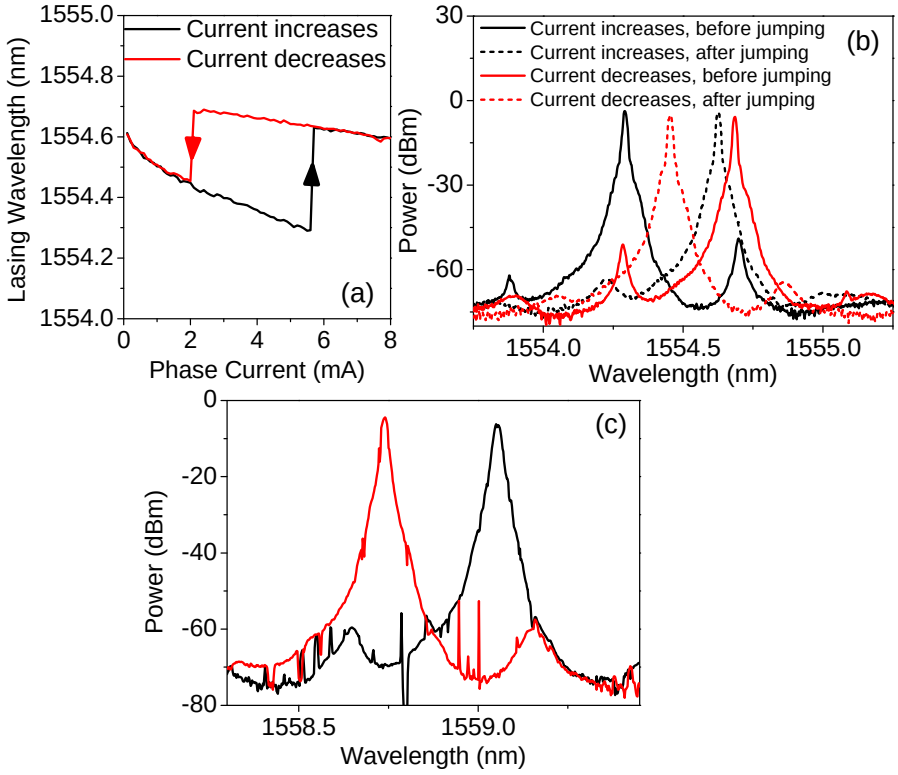

Figure 4.3: Static lasing characteristics of the MG-Y laser. (a) Lasing wavelength as a function of the phase current for the 1554 nm bistable window. (b) Optical spectra of different lasing states in the 1554 nm bistable window. (c) Lasing behaviour at 1559 nm.

∼50 dB, for both lasing wavelengths.

When tuning to other wavelengths by varying the currents applied on the reflectors, such static bistability may not always be obtained. Instead, unstable lasing at certain phase currents was noticed where two competing modes were present, as shown in Fig. 4.3(c). The noisy spectra were due to the unstable lasing. Many lasing windows were found with similar behaviour at high reflector currents. We will show in the following section that several these windows were demonstrated with dynamic bistability.

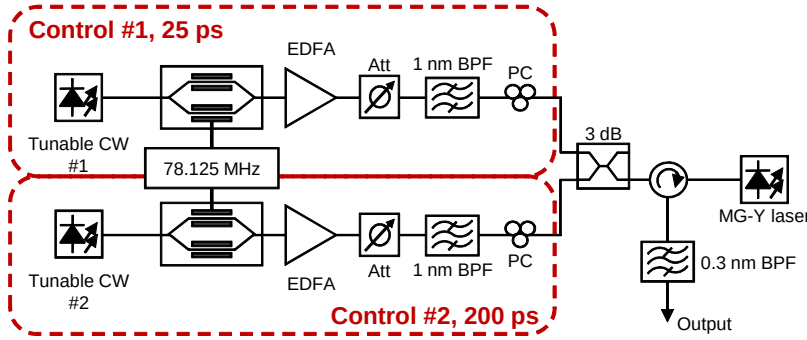

Figure 4.4: Experimental setup for wavelength flip-flop demonstration.

4.2.4 Wavelength tunable AOWFF

Since the MG-Y laser used in the experiment is not packaged, a piece of tapered fibre was used to couple the laser output to a circulator so that the control pulses can be injected into the laser cavity. The measured output power after the circulator was ∼8 dBm. Taking into account the coupling and circulator losses, the output power of the MG-Y laser in normal configuration was estimated to about 11 dBm.

The experimental setup for optically controlled wavelength flip-flop operation is shown in Fig. 4.4. Two tunable continuous wave (CW) sources were separately modulated by Mach-Zehnder modulator (MZM) driven by programmed 40 Gbit/s and 5 Gbit/s data patterns, so that a ∼25 ps (control #1) and a ∼200 ps (control #2) optical control pulses were generated every 12.8 ns. Both control signals were amplified by erbium doped fibre amplifier (EDFA) and filtered by 1 nm optical band-pass filters (OBPFs). The control pulses were combined and fed into the MG-Y laser via a circulator and their polarisation states were controlled individually by polarisation controllers (PCs) to match the MG-Y laser. The laser output was filtered by a 0.3 nm thin-film filter (TFF) and monitored on an oscilloscope following detection.

The waveforms and spectra of the control pulses are shown in detail in Fig. 4.5. The time interval between adjacent control pulses #1 and #2 pulses was about 6-7 ns. The measured pulse widths were 22 ps and 202 ps for control #1 and control #2, respectively.

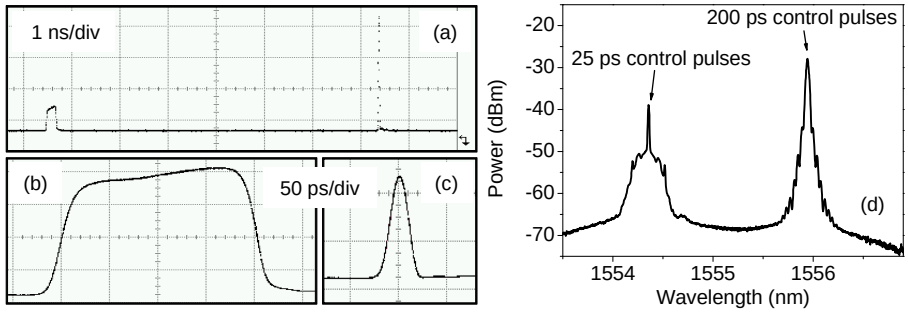

Figure 4.5: Control pulses: (a) both control pulses are present; (b) control #2 pulse; (c) control #1 pulse; (d) spectrum of the combined control signals.

Dynamic flip-flop characteristics in the 1554 nm window

The MG-Y laser was operated with 100 mA gain current and 3.6 mA phase current in order to obtain dynamic bistable operation. Control #1 is placed at 1554.304 nm and has an average power of −16.9 dBm, corresponding to 0.26 pJ/pulse, while control #2 is at 1554.774 nm with −16.1 dBm average power (0.31 pJ/pulse). The flip-flop lasing is at the two wavelengths of 1554.37 nm and 1554.66 nm, as shown in Fig. 4.3 (a) and (b). The switch-on and switch-off time at both wavelengths is less than 200 ps.

It was noticed that, when detuning control #1 by 40 pm to 1554.344 nm, the required control power rose to −12.9 dBm (0.66 pJ/pulse), with a more noisy output. This observation is in agreement with the effect reported in [83]. The bistability could still be obtained in a 180 pm range (1554.214 nm ∼ 1554.394 nm). Due to insufficient control pulse power achievable from the setup, the detuning further than this range could not be examined.

We also checked the flip-flop operation following the same principle as described in [79], which takes advantage of the asymmetric gain effect in favour of longer wavelength mode. When a high energy reset pulse (200 ps, 5.85 pJ/pulse) at an arbitrary wavelength (here 1556 nm) is injected to deplete the carriers, the equilibrium of carrier density is broken. The laser will be set to the state with lower carrier density (lasing at 1554.66 nm). When a weak set pulse (25 ps, 0.39 pJ at 1554.344 nm) is injected, it will set the MG-Y laser to lase at 1554.39 nm. However,

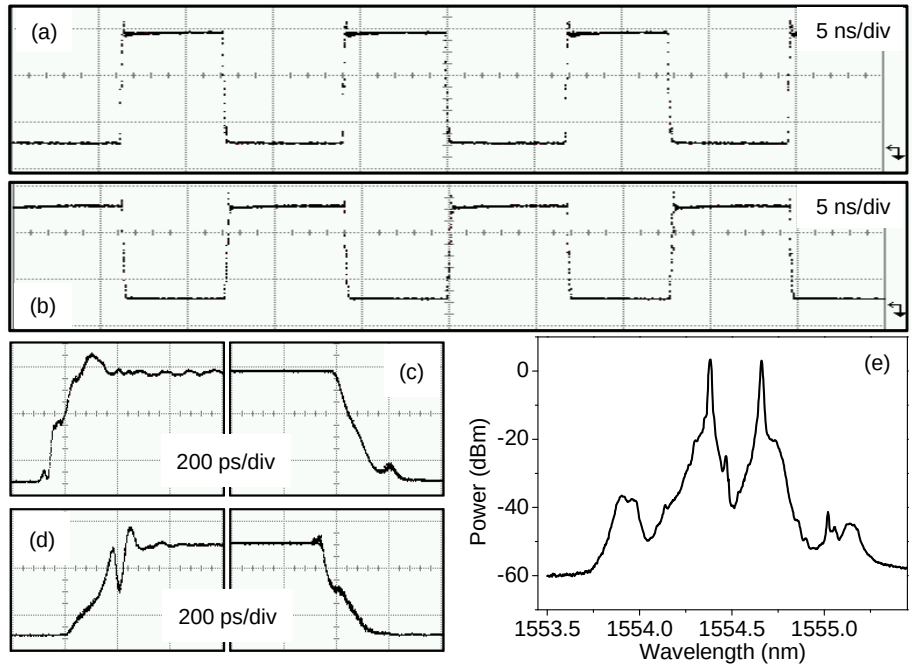

Figure 4.6: Wavelength flip-flop operation in the 1554 nm bistable window. (a) Bistable MG-Y output at 1554.37 nm; (b) output at 1554.66 nm; (c) switch-on/off feature at 1554.37 nm; (d) switch-on/off at 1554.66 nm, and (e) spectrum of the bistable output.

strong overshoots on the flip-flop output were observed at switch-on and switch-off due to the strong control pulse.

Wavelength-tunable flip-flop operation

AOWFF operation was also obtained at 1559 nm and 1560 nm. The corresponding control pulse wavelengths and energies are listed in Table 4.1, and the bistable operations in the two windows are shown in Fig. 4.7.

We may notice that the control pulse energies in the 1559 nm window are higher than at 1560 nm. This is due to that fact that the control pulse wavelength was not placed to the optimum position and also the polarisation was not fully optimised. The flip-flop waveforms in Fig. 4.7(b) are therefore noisier than those in Fig.4.7(a) because of the

MG-Y lasing output (nm)		Control #1		Control #2	
		Wave-length (nm)	Pulse energy (pJ)	Wave-length (nm)	Pulse energy (pJ)
1560.12	1560.42	1560.054	0.34	1560.506	0.16
1558.75	1559.04	1558.780	0.65	1559.146	0.54

Table 4.1: Control pulses properties for flip-flop operation at 1559 nm and 1560 nm.

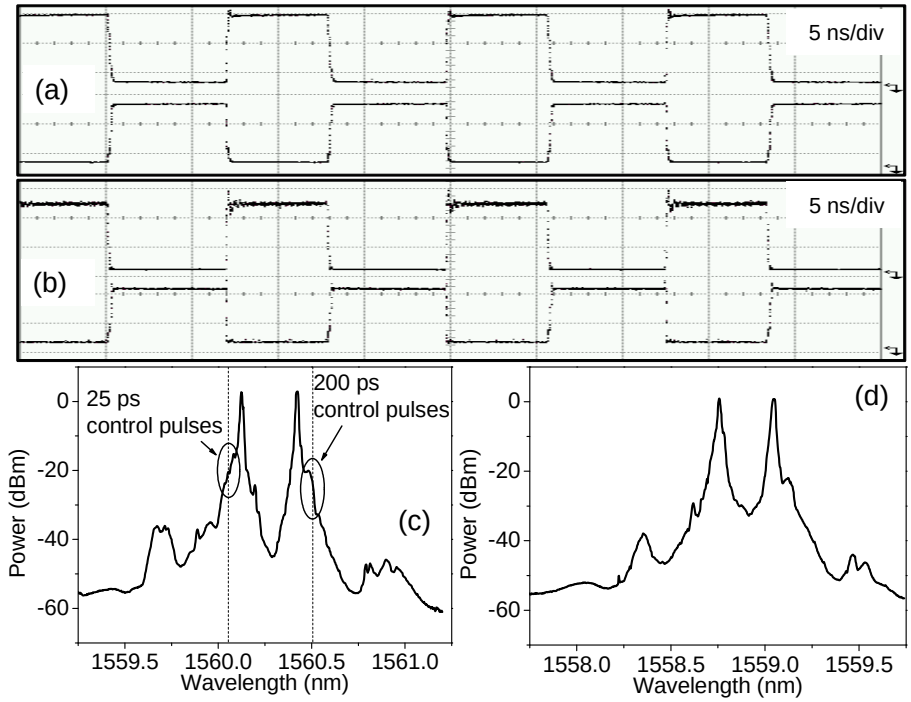

Figure 4.7: All-optical flip-flop operations at other wavelengths: (a) flip-flop in the 1560 nm window; (b) flip-flop in the 1559 nm window; (c) spectrum of the bistable output in the 1560 nm window and (d) spectrum of the bistable output in the 1559 nm window.

higher injection.

Fig. 4.7(c) illustrates the positions of the injection wavelengths with respect to the lasing spectra. The dash lines indicate the central wavelengths of the optical controls. The asymmetries in the spectra of the MG-Y output are due to the presence of the control pulses, which could already be observed in Fig. 4.6(e). It has to be pointed out that the MG-Y lasing wavelengths are different from those of the injected control signals, which indicates that the injection was set on the side-mode, but the lasing was not locked to the injection. It can be understood that the side-mode injection changed the refractive index of the cavity and also change the gain. It also enhanced the interaction including energy exchange between the main mode and the side mode. When the injection is high enough, the lasing balance broke and hence the wavelength jumped. When the new balanced is built, the lasing wavelength will be maintained, and external injection is no longer needed.

Control condition comparison

The AOWFF operation of the laser was also achieved using the same pulse width for both of the set and reset pulses.The control pulse power was examined. The control pulse powers listed in Table 4.2 were obtained when injecting at the wavelengths shown in Table 4.2. As the laser is free space coupled and electronically probed, some conditions are therefore changed, for example the coupling loss. The lasing wavelength was also found shifted 0.1 nm even though the phase current and reflector current were the same. Therefore the control pulse power

Control pulse width (ps)	Control pulse power			
	1554.220 nm		1554.748 nm	
25	−7.56 dBm	2.24 pJ	−18.62 dBm	0.18 pJ
50	−9.98 dBm	1.28 pJ	−20.73 dBm	0.11 pJ
75	−8.41 dBm	1.84 pJ	−22.52 dBm	0.07 pJ
100	−9.13 dBm	1.56 pJ	−22.79 dBm	0.07 pJ

Table 4.2: Comparison of control pulses with different pulse-widths for flip-flop operation at 1554 nm.

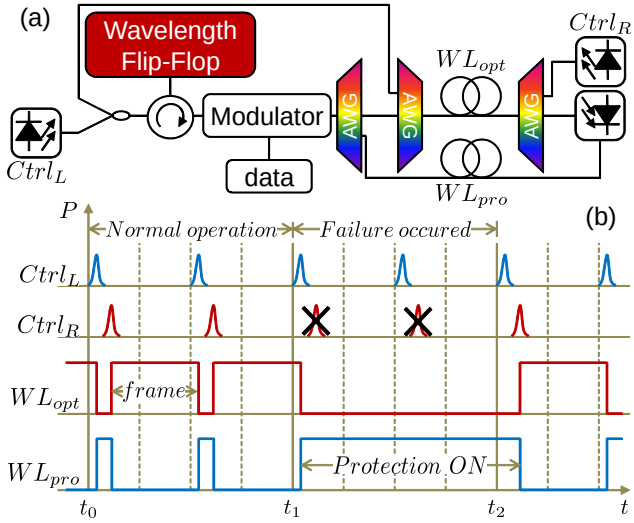

Figure 4.8: Proposed scheme for all-optical self-aware protection switching. (a) Physical configuration. (b) Timing diagram for normal operation in the interval $[t_0, t_1]$ and protection operation in $[t_1, t_2]$.

levels obtained in this part can not be compared with those obtained previously.

However we can compare the control pulse energies obtained within the table. First of all, the control pulse energy can be ultra-low (as low as less than 0.1 pJ), as long as, control pulses with long pulse width are used. These pulse energies are similar to the one achieved in [83], i.e. 0.03 pJ with 1 ns control pulse at optimum injection wavelength. Second, the control power requirement for injection locking to the longer wavelength mode is much lower than for the shorter wavelength. As shown previously, the Bogatov effect was confirmed by experiment. The asymmetrical gain in favour of long wavelength mode could be also responsible for the energy difference between the two control pulses.

4.3 All-Optical Protection Switching Using AOFFs

4.3.1 Operation principle

In order to realise protection switching within a nano-second, an ultra-fast self-aware all-optical protection switching (AOPS) scheme is proposed and demonstrated. The proposed scheme relies on a wavelength-bistable laser (also known as AOWFF) used as a CW light source that is externally modulated at the transmitter, as shown in Fig. 4.8(a). In an AOWFF, light emission can be switched between two stable operating wavelengths by two distinguishable optical control pulses (set and reset). The wavelength of the emitted signal will thus depend on the state of the AOWFF. A wavelength selective component such as an arrayed waveguide grating (AWG) can then be employed to route the signal on the pre-defined operation wavelength WL_{opt} to the working fibre, or on the protection wavelength WL_{pro} to the backup fiber in case an event triggers the protection switching mechanism.

The fault detection and subsequent triggering of the emission wavelength of the AOWFF is implemented as follows. A periodic optical control signal associated with WL_{opt} is generated at the destination side and transmitted via the working path fiber back to the source for controlling the AOWFF. This control is denoted $Ctrl_R$. The other control, associated with WL_{pro}, is locally generated at the source side and denoted $Ctrl_L$. The $Ctrl_R$ and $Ctrl_L$ pulses are generated periodically with the same repetition rate.

The timing diagram of Fig. 4.8(b) illustrates the operation of the scheme. Under normal operation (in the interval $[t_0, t_1]$), $Ctrl_L$ appears first and turns on WL_{pro}. Shortly after, the remote control pulse $Ctrl_R$ arrives and resets the operation back to WL_{opt}. The time interval over which WL_{opt} is switched on, until it is switched off by the next $Ctrl_L$, is therefore a time-frame of fixed duration, which can be used for sending the data traffic.

If $Ctrl_R$ does not reach the AOWFF due to link failure, as indicated in the interval $[t_1, t_2]$ in Fig. 4.8(b), the local control $Ctrl_L$ will enable WL_{pro} as usual, however WL_{opt} will not be reset. This will result in the data being now modulated on the protection wavelength and routed

to the backup fibre by the AWG. Therefore the protection is realised. As soon as $Ctrl_R$ is back, the operation will be changed back to normal automatically, as illustrated from t_2 in Fig. 4.8(b).

In this way, the entire protection procedure, including link failure detection and protection trigger, which are all performed via the optical remote control pulses $Ctrl_R$, are realised on the optical layer. The total protection time will then depend on the switching speed of the AOWFF device, which can be of the order of a few hundred ps as demonstrated further, as well as the propagation delay and the size of the frames. The latter two points are common to all protection schemes, including those relying on the protocol. Even though such an optical layer protection switching scheme does not provide fault location, its main benefit is to allow an ultra-fast set up of the protection link, while the other functionalities such as fault monitoring can still be realised through the protocol.

4.3.2 Experimental setup for demonstrations

Figure 4.9 shows the experimental setup used for the proof-of-concept demonstration of the proposed scheme. The AOWFF used in the exper-

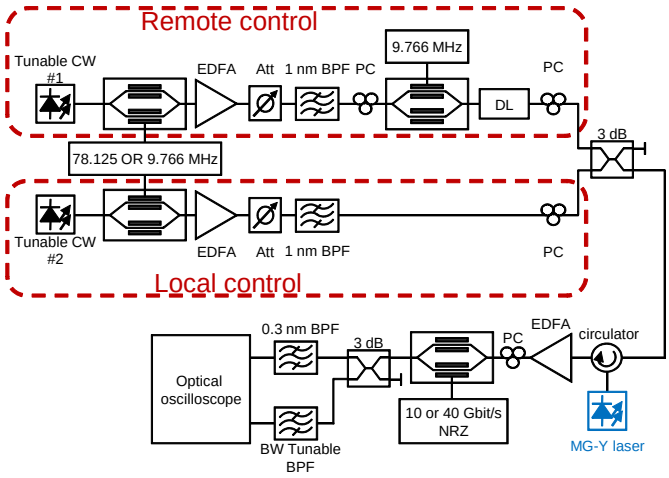

Figure 4.9: Experimental setup for proof-of-concept demonstration of protection switching.

iment is a single MG-Y laser structure, in which flip-flop operation over a large wavelength tunable range has been demonstrated as shown in Section 4.2. In this case the required optical control pulses are carried over different wavelengths. In the experiment, two tunable external cavity CW lasers were externally modulated using two MZMs in order to the generate 50 ps long control pulses with, at first, a low repetition rate of 78.125 MHz. The control signals were amplified in EDFAs, filtered in OBPFs and their relative delay was adjusted using an optical delay line (DL) before they were injected into the MG-Y laser via a circulator.

The state of polarisation of the control signals was beforehand adjusted using PCs. The bistable wavelength window operating on 1554.37 nm or 1554.66 nm was chosen to demonstrate the scheme. The MG-Y laser output was then modulated with 10 Gbit/s or 40 Gbit/s non return-to-zero (NRZ) data with a $2^{31} - 1$ pseudo random bit sequence (PRBS). Two OBPFs were used to emulate an AWG and route the signal to a different port depending on its wavelength. The signals at the operation wavelength and at the protection wavelength were then monitored on an optical sampling oscilloscope.

To emulate the link failure, the remote control pulses were periodically suppressed using another MZM driven at 9.766 MHz, resulting in 3 out of 8 $Ctrl_R$ pulses being suppressed. The dynamic extinction ratio of the modulator was about 10 dB and the gating window generated by the MZM can be seen in Fig. 4.10(a).

4.3.3 Scheme demonstration and link performances

In order to illustrate the scheme, the waveforms on both wavelengths in both normal operation and protection regime are shown in Fig. 4.10(b)-(c). Under normal operation, as indicated in the figure, 5 frames of data traffic on WL_{opt} can be seen. Note that a short frame length of ∼100 bits at 10 Gbit/s was chosen in Fig. 4.10 to ease the visualisation of the process on the oscilloscope traces, but the scheme is obviously highly scalable towards lower repetition rates of the control signals.

The next 3 $Ctrl_R$ pulses were suppressed, emulating a cut in the working path. As shown in Fig. 4.10(c), the data was immediately switched to WL_{pro} while no more data was sent on WL_{opt}, as can be seen in Fig. 4.10(b), apart from some residual out-of-band crosstalk leak-

ing through the 0.3 nm optical bandpass filter used for signal separation in our proof-of-concept implementation. Figure 4.11 shows the eye diagrams of both WL_{opt} in normal operation and WL_{pro} in protection operation with 10 Gbit/s and 40 Gbit/s data modulation. The eyes are both widely open, indicating good signal quality.

The bit error rate (BER) measurements were also performed with 10 Gbit/s NRZ data modulation, as shown in Fig. 4.12(a). When modulating the MG-Y laser output without any control pulses, the sensitivity is about -34 dBm (at BER= 10^{-9}). Unfortunately, due to the lack of a proper burst gating control, BER measurements for both normal and protection operations could only be performed in continuous gating mode.

For error counting, the repetition rate of the control signals was set to 9.766 MHz, allowing 1024 bits of 10 Gbit/s signal in every period. As 10 bits were switched off from WL_{opt} between two adjacent frames, as shown in Fig. 4.12(b), and assuming an equal distribution of marks and spaces when averaging over many frames, 5 bits on average would be erroneously detected even if no error occurs during normal operation,

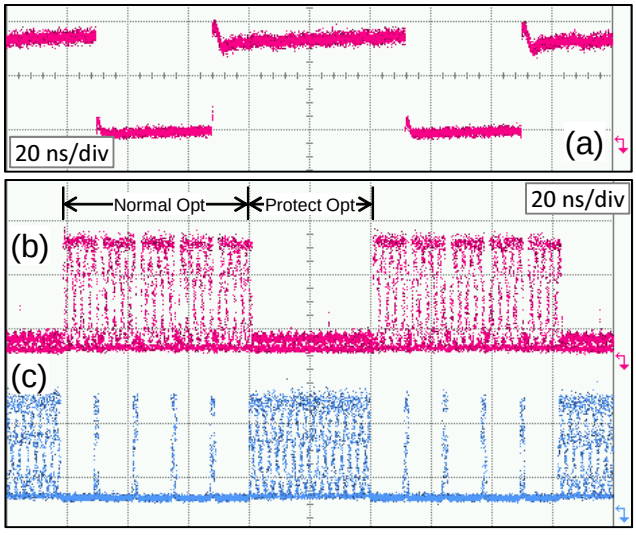

Figure 4.10: All-optical protection switching demonstration: (a) Gating window for emulating the link failure. Waveform on (b) WL_{opt} in normal mode and (c) WL_{pro} in protection mode.

leading to a minimum achievable BER of 4.9×10^{-3}. The measured BER of WL_{opt} with sufficient receiver power was exactly lying on this level, indicating no performance degradation for the bits transmitted over the frame.

On WL_{pro}, some bits were affected by $Ctrl_L$, as shown in Fig. 4.12(c), since it disturbed the carrier density of the MG-Y laser, causing a moderate power penalty compared to CW operation, as shown in Fig. 4.12(a).

4.4 Discussion

Even though the scheme has been demonstrated here by exploiting the wavelength bistability of a widely-tunable MG-Y laser, other bistable laser sources could be employed instead. For instance wavelength flip-flop has been demonstrated in DBR lasers [79, 83], with switching speed of less than 50 ps and pulse energies of a few picojoules being reported in the earlier experiment. Wavelength flip-flop has also been demonstrated based on two semiconductor optical amplifier (SOA)-based coupled ring lasers with a switching speed of 20 ps [90]. Alternatively, flip-flop sources with dual-lasing directions, such as micro-disk lasers [81], could also be used, however at the expense of some redundancy in terms of external modulators.

There is also possibility of using a Fabry Pérot (FP) laser with continuous external light from the far-end in the same scheme to injection lock the FP laser so that the lasing wavelength can also be switched.

The proposed method allows for a quick establishment of the protection path. It therefore does not substitute to other protection mechanisms based on the protocol, where the network management would be informed of the existence and location of a link failure. Such schemes should still be implemented in order to provide the full functionality of protection and restoration. However, the main benefit of our method is to provide an ultra-fast establishment of the protection path resulting in a minimum loss of data, while the failure can still be detected by other slower means (e.g. by monitoring the power and OTDR) resulting in the network management being informed by the protocol and appropriate measures being taken. The method thus provides a speed advantage for some critical applications requiring a faster protection time than what is currently offered.

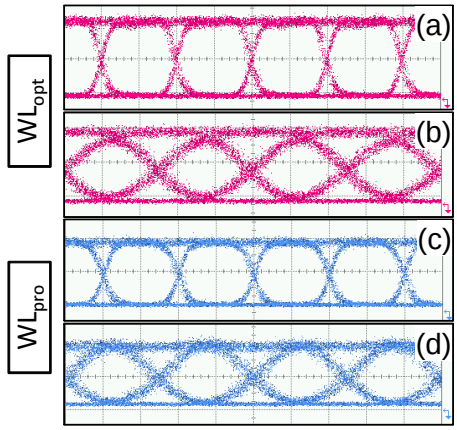

Figure 4.11: Eye diagrams of the data at the transmitter output under normal operation on WL_{opt} at (a) 10 Gbit/s and (b) 40 Gbit/s, as well as under protection operation on WL_{pro} at (c) 10 Gbit/s and (d) 40 Gbit/s.

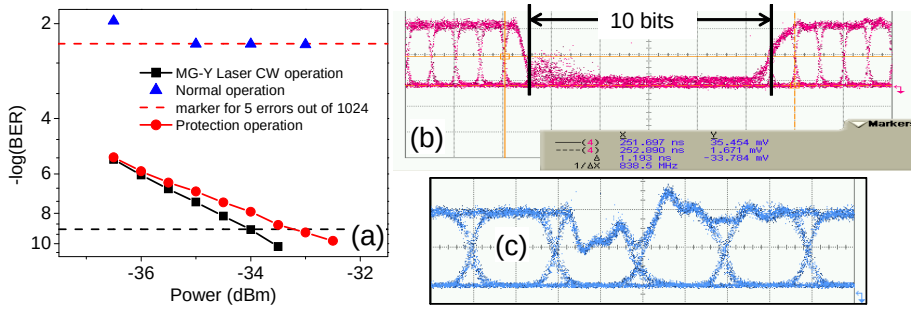

Figure 4.12: Link performance with 10 Gbit/s NRZ data: (a) BER measurement. (b) time interval between two adjacent frames on WL_{opt} in normal operation and (c) bits on WL_{pro} affected by the local control pulses in protection operation.

4.5 Summary

In this chapter, a novel concept of all-optical protection switching was proposed. Link failure detection and protection trigger were both implemented on the optical layer. The concept was experimentally demonstrated using a wavelength tunable AOWFF based on a single MG-Y laser structure. The achieved protection switching time was less than 200 ps. The good quality of the signal following the establishment of the protection path was evaluated at both 10 and 40 Gbit/s. The flip-flop operation in a single MG-Y laser structure was experimentally demonstrated operating at three different wavelengths. The AOWFF operation was believed to be with wide wavelength tunability.

Chapter 5

All-Optical Network Coding

5.1 Introduction

Previously in Chapter 4, an all-optical scheme with automatic fault detection and protection switching all implemented in the physical domain was presented and discussed. In this way, the data is quickly switched on to the protection path. From the bandwidth aspect, this method does not take more bandwidth than what the data requires. However, in order to perform the fault detection and acknowledgement as well as the data switching or re-transmission, we have to pay the price on the complexity of system design. On the other hand, duplicating the data in the network to increase the reliability of the data transmission is the most simple way to protect the data from outage, for example in Avionic networks [19]. Therefore it is also a frequently used protection method.

To implement such a duplex protection scheme, considering a simple four-node network as shown in Fig. 5.1, two nodes (**A** and **B**) both send data to a third node **D**. A protection mechanism can be implemented in which both nodes transmit a copy of the message to **C**, which relays it to the final destination **D** through another path, thus decreasing the odds of being affected by a link failure. At node **D**, a data selecting algorithm needs to be implemented so that one of the two data copies can be selected. In avionic networks, the data transmission and protection is implemented in such way, for example in the avionics full-duplex

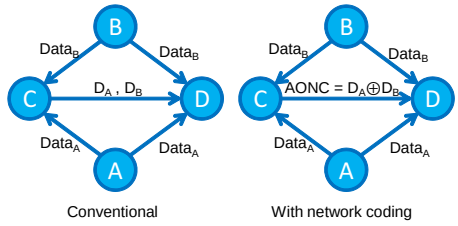

$Data_A$	$Data_B$	AONC	AONC ⊕D_A	AONC⊕D_B
1	0	1	0	1
0	0	0	0	0
1	1	0	1	1
1	0	1	0	1
0	1	1	1	0
0	1	1	1	0
1	1	0	1	1

Figure 5.1: Network protection in duplex networks with operation principle of network coding for protection purpose.

switched ethernet network [19].

Therefore in this conventional networks perspective, the data transmission and protection will push the growth of the bandwidth requirement of the entire network even faster. In order to save bandwidth while protecting the network, a new scheme has been proposed where **C** only sends to **D** an encoded signal *AONC*, which is obtained by exclusive OR (XOR) operation between $Data_A$ and $Data_B$, as illustrated in the truth table of Fig. 5.1. If any of $Data_A$ or $Data_B$ does not reach **D** due to link failure, the lost information can be retrieved from the encoded *AONC* and the successfully transmitted message using a simple XOR operation.

This technique, which is called "Network Coding", can increase the survivability of the data in such duplex networks. Network coding was firstly proposed to increase the throughput of multicast networks [20]. Moreover, it can also be exploited to efficiently protect the network against failures and thus avoid loss of information [21]. It has been intensively studied in both wired and wireless networks in view of increasing the throughput and providing network survivability [91–94]. Manley et al. proposed to employ the network coding in the optical domain to protect all-optical multicast networks [22].

In this thesis, this technique is named as all-optical network coding (AONC). AONC has been reported [95] for optical on-off keying (OOK) signal using all-optical XOR gate based on semiconductor optical amplifiers in a Mach-Zehnder interferometer configuration (SOA-MZI). Liu et al. proposed to use polarisation multiplexing instead of XOR gates to avoid bit-synchronisation [96]. The feasibility of applying AONC schemes for phase modulation formats, such as differential phase shift

keying (DPSK), needs to be evaluated as well, which is the topic of this chapter.

This chapter is structured as follows:

Firstly an overview on all-optical XOR gates is given in Section 5.2. The principles of XOR gates for intensity and phase modulated signals are presented, especially focussing on phase modulated signals. Then, the experimental implementation of the AONC scheme for DPSK signals, is presented in Section 5.3. Successful data recovery and error-free performance of the AONC scheme using SOAs is demonstrated. The total operation penalty can be as low as 1 dB using 10 Gbit/s DPSK signals. In consideration of multicast networks, the feasibility of multicasting the *AONC* signal is evaluated as well. In Section 5.4, phase-halving operation is discussed. The feasibility of applying AONC to more advanced phase modulated signals, multi-level phase shift keying (mPSK) signals, is discussed as well. Synchronisation, including both pattern-synchronisation and bit-synchronisation, is an important issue for AONC operation. It is also discussed in Section 5.4.

5.2 Overview of All-Optical XOR Logic Gates

All-optical logic operations are important for many optical network functions, such as switching [97], signal regeneration [98], header processing [99], data encoding [95, 100], encryption [101] etc. Therefore they are of great importance for optical communication system and they are the potential building blocks for future all-optical computing and interconnect applications.

5.2.1 XOR logic gates for OOK signals

For OOK signals, as the optical intensity is modulated, logic operations should therefore be applied to the intensity. For this purpose, the use of SOA-MZIs was proposed and studied in [102, 103]. They are generally used for logic (ADD, OR and XOR) operation, and XOR gates for 42.6 Gbit/s return-to-zero (RZ)-OOK signal have been demonstrated [104, 105].

However, their performance was limited by the slow gain recovery and phase response of the SOAs, typically 50-200 ps. A scheme including a delay interferometer (DI) after the SOA-MZI was proposed and demonstrated to operate at 80 Gbit/s [106]. An XOR scheme utilising phase shift introduced by SOAs and interferometer based on polarisation maintaining (PM) fibre was also demonstrated to work at 40 Gbit/s [107, 108].

5.2.2 XOR logic gates for phase modulated signals

For phase modulated signals, all-optical logic operations should be performed directly on the phase without O/E/O conversion. They require nonlinear effects, which can operate on the phase.

XOR logic gates for DPSK signals have been demonstrated using degenerate four-wave mixing (FWM) [109] and non-degenerate FWM [110] with SOAs as nonlinear media. FWM-based XOR gates have also been investigated in other nonlinear media such as highly nonlinear fibres (HNLFs) and silicon nanowires [111]. The SOAs, which are active media, have advantages in terms of input power requirements, which are usually much lower compared to passive media. However the data bandwidth is limited intrinsically by the speed of the SOAs.

Four-wave mixing

The response of any dielectric to light becomes nonlinear when an intense electromagnetic field is applied [112]. When a light wave is applied to the dielectric medium, its electric field introduces a polarisation, denoted as P, to the medium, which is related to the electric field by:

$$P = \epsilon_0\big(\chi^{(1)}E + \chi^{(2)}E + \chi^{(3)}E + \dots\big)\ , \tag{5.1}$$

where E denotes the electric field of the incident light wave, ϵ_0 is the vacuum permittivity, $\chi^{(1)}$ is the linear susceptibility and $\chi^{(2)}$, $\chi^{(3)}$, ... are called as the nonlinear susceptibilities of the medium [113]. If three optical fields with carrier frequencies ω_1, ω_2 and ω_3 co-propagate inside the dielectric material simultaneously, $\chi^{(3)}$ generates a fourth field whose frequency ω_4 is related to other frequencies by a relation $\omega_4 = \omega_1 \pm \omega_2 \pm \omega_3$. Several frequencies corresponding to different plus and minus sign

combinations are possible as long as the phase-matching condition

$$\Delta k = k_3 + k_4 - k_2 - k_1 = 0 \ , \tag{5.2}$$

is fulfilled. However in practice, only the form $\omega_4 = \omega_1 + \omega_2 - \omega_3$ is most likely to be generated as the input frequencies are nearly phase-matched, especially near the zero-dispersion wavelength. If two initial photons are degenerate ($\omega_1 = \omega_2$), the FWM process will occur more easily so that $\omega_4 = 2\omega_1 - \omega_3$ is generated, which is normally referred to as degenerated FWM.

In fact, not only the signal frequency will satisfy $\omega_4 = \omega_1 \pm \omega_2 \pm \omega_3$, but the phase of the generated signal will also depend on the phase of the interacting waves. Three input field $E_1(A_1, \omega_1, \phi_1)$, $E_1(A_2, \omega_2, \phi_2)$ and $E_3(A_3, \omega_3, \phi_3)$ will beat and produce a fourth field, E_4, which can be described as:

$$\begin{aligned} E_4 = {} & r(A_1 \cdot A_2 \cdot A_3) \\ & \times exp[j(\omega_1 \pm \omega_2 \pm \omega_3)t + (\phi_1 \pm \phi_2 \pm \phi_3)] \ , \end{aligned} \tag{5.3}$$

where r is the conversion efficiency, which depends on the nonlinearity of the media and the phase matching condition. The phase of the generated field is noted with the relation $\phi_4 = \phi_1 \pm \phi_2 \pm \phi_3$.

The nonlinear gain dynamics, including inter- and intra-band effects in SOAs are both responsible for the process of FWM [114]. The inter-band effects refer to transitions between the conduction band and the valence band, as the carrier is depleted by the stimulated emission, which is also referred to as carrier density pulsation (CDP). The intra-band effects refer to the change of the carrier distribution within one band. The intra-band effects are associated with basically two phenomena. The first is the spectral-hole burning (SHB), where the stimulated emission burns a hole in the carrier distribution. The other one is the carrier heating (CH), where free carriers at low-energy levels are transferred to higher levels due to free carrier absorption. The characteristic time of CDP, which is the effective carrier lifetime, is of the order of several hundred picoseconds. The time constants associated with SHB and CH are much faster, typically several tens of femtoseconds for the former and hundreds of femtoseconds for the latter. Therefore, the data bandwidth for signal processing using SOAs is limited intrinsically by the slow carrier recovery.

In passive media, for example HNLFs, even though the speed of the process is of the order of a few fs, much higher input signal power is required for acquiring the same conversion efficiency r. Moreover, other nonlinear effects arising from $\chi^{(3)}$ [113] will also become stronger as input signal power increase. The stimulated Brillouin scattering (SBS) is one of them, which limits the launched signal power and hence the conversion efficiency to a relative low level because of its low threshold [112]. In order to increase the conversion efficiency, SBS suppression is required, for instance [115].

Principle of XOR gates for DPSK signals

The logic gate for phase modulated signals relies on FWM. When using degenerated FWM, as shown in Fig. 5.2(a), with input beams having angular frequencies ω_{A} and ω_{B}, two new frequencies will be generated, referred as idlers. The phases of the two idlers will satisfy $\phi_{\mathrm{Idler},1} = 2\phi_{\mathrm{A}} - \phi_{\mathrm{B}}$ and $\phi_{\mathrm{Idler},2} = 2\phi_{\mathrm{B}} - \phi_{\mathrm{A}}$, respectively. Considering that the input beams are modulated with binary phase modulation formats (binary phase shift keying (BPSK) or DPSK) where the phase is modulated so that $\phi \in [0, \pi]$, none of the idlers will carry a phase that is the result of logic operation on the inputs. For this to happen requires that one of the two inputs has to be modulated with $\phi \in [0, \frac{\pi}{2}]$. Then the phase of one of the idlers can be the result of XOR operation between ϕ_A and ϕ_B, as illustrated in Table 5.1(a).

In non-degenerated FWM case, three input beams are required. In order to realise a logic gate for the two inputs ω_{A} and ω_{B}, the third input

A	B	2A-B	2B-A
0	0	0	0
0	π	π	0
$\frac{\pi}{2}$	0	π	$-\frac{\pi}{2}$
$\frac{\pi}{2}$	π	0	$-\frac{\pi}{2}$

(a)

A	B	A+B	A-B
0	0	0	0
0	π	π	π
π	0	π	π
π	π	0	0

(b)

Table 5.1: Logic truth table of XOR gate based on FWM for phase modulated signals with phase modulation $\phi \in [0, \pi]$. XOR logic truth table using (a) degenerated FWM, (b) non-degenerated FWM.

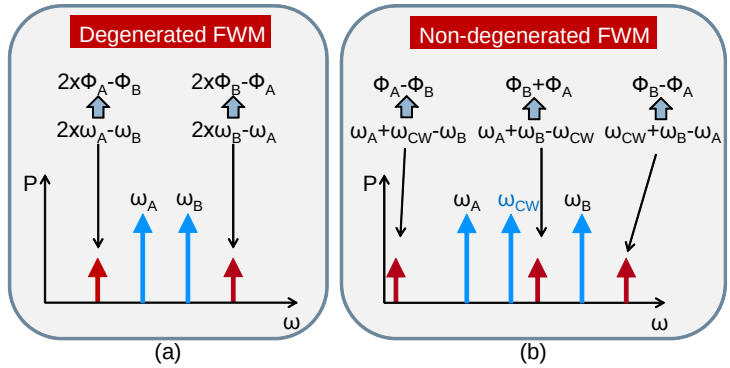

Figure 5.2: Principle of FWM used in as XOR logic gates for DPSK signals.

beam should not carry any phase modulation, therefore it should be a continuous wave (CW) beam. Three new frequencies will be generated and the phase of the idlers will satisfy $\phi_{\mathrm{Idler},1} = \phi_{\mathrm{A}} + \phi_{\mathrm{CW}} - \phi_{\mathrm{B}}$, $\phi_{\mathrm{Idler},2} = \phi_{\mathrm{A}} + \phi_{\mathrm{B}} - \phi_{\mathrm{CW}}$ or $\phi_{\mathrm{Idler},3} = \phi_{\mathrm{CW}} + \phi_{\mathrm{B}} - \phi_{\mathrm{A}}$, as shown in Fig. 5.2(b). Thanks to the 2π periodicity of the phase, the generated idlers will also carry binary phase information, which is the result of XOR operation between ϕ_A and ϕ_B, as illustrated in Table 5.1(b).

If the three input waves are equally spaced in frequencies, as the phase-matching for degenerated FWM is satisfied more easily, new frequencies generated by the degenerated FWM will overlap exactly on top of the non-degenerated FWM products and therefore destroy the phase information. Therefore for the implementation of the XOR gate using non-degenerated FWM, three inputs are spaced unevenly to avoid the overlapping, as shown in Fig.5.2. We can notice that in this way, there will be three FWM products generated with the correct phase information resulting from XOR operation. Furthermore, there is no restriction on how to order of these three inputs.

5.3 All-Optical Network Coding for DPSK Signals

Differential phase shift keying (DPSK) signals are being currently employed in optical networks because of their significantly reduced optical

signal to noise ratio (OSNR) requirements compared to intensity modulation thanks to balanced detection [116]. Therefore AONC schemes need to be applied to DPSK signals as well.

SOAs have advantages in term of input power requirements, which are lower compared to passive media. This is of critical importance, as for implementing an AONC scheme at least two XOR logic operations are required. However the data bandwidth is limited intrinsically by the SOAs as discussed previously in Section 5.2.2.

Even though degenerate FWM can also perform XOR logic operation, it has restrictions that one of the input has to be with phase modulation between $\phi \in [0, \frac{\pi}{2}]$. For network coding application, the signal needs to be recoverable by a second XOR operation. After network coding, the AONC signal is again with phase modulation $\phi \in [0, \pi]$. Data retrieval can only happen if the half-π modulated signal is present. Therefore the data recovery can not be fully achieved, unless phase-halving operation can be performed.

In this section, an AONC scheme using two XOR gates based on non-degenerate FWM in SOAs is experimentally demonstrated. The feasibility of the scheme was evaluated with two 10 Gbit/s non return-to-zero (NRZ)-DPSK signals. Complete recovery of the lost information is demonstrated and error-free operation is achieved with as little as 2 dB of power penalty for the two XOR stages. Furthermore only minor pattern effects are reported, leading to less than 0.4 dB of variations in the power penalty. The feasibility of multicasting the AONC code was also evaluated experimentally.

5.3.1 Experimental setup and logic operation

Considering the network scenario illustrated in Fig. 5.1, the experimental setup for demonstrating AONC for DPSK signals using a non-degenerate FWM process in SOAs is shown in Fig. 5.3. Two 10 Gbit/s NRZ-DPSK signals were generated by modulating two optical CWs at 1552.6 nm (labelled as **Data A**) and 1546.6 nm (labelled as **Data B**) using a common Mach-Zehnder modulator (MZM). The signals were then split by filtering, de-correlated using 1 km of standard single mode fibre (SMF) on one of the paths, amplified together with another CW signal generated by a distributed feed-back (DFB) laser diode at 1551 nm, up to a total

power of 15.5 dBm, and then injected into the first SOA. Both SOAs used in the experiment are commercial devices from CIP [117] (model SOA-NL-OEC-1550), and both of them are biased with a 400 mA current, at which the amplified spontaneous emission (ASE) gain peak is about 1560 nm.

The FWM between Data A, Data B and the CW in the first SOA results in generating idlers, three of which are of particular interest as their phases carry the logical XOR between Data A and Data B. Such idlers can be regarded as an AONC code to be sent to node D, as shown in Fig. 5.4(a). In the work presented in this section, the selected FWM product was the idler at 1548.2 nm, i.e. corresponding to $\{\omega_A + \omega_B - \omega_{CW}\}$, where ω_A, ω_B and ω_{CW} are the angular frequencies of Data A, Data B and the CW signal injected in the first stage SOA, respectively. The spectra measured at the input and output of the SOA are shown in Fig. 5.4 (a).

In the case of a link failure resulting in the loss of **Data A**, the AONC code can be used to retrieve Data A at node D from another XOR operation between the AONC code itself and Data B.

In order to demonstrate the feasibility of such a process, the AONC at the output of the first SOA has been selected by an optical band-pass

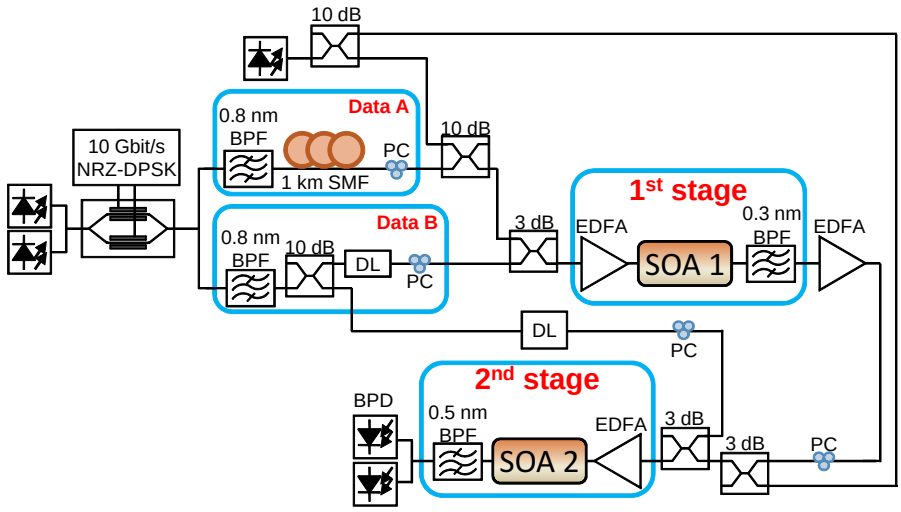

Figure 5.3: Experimental setup for demonstrating AONC for DPSK signals.

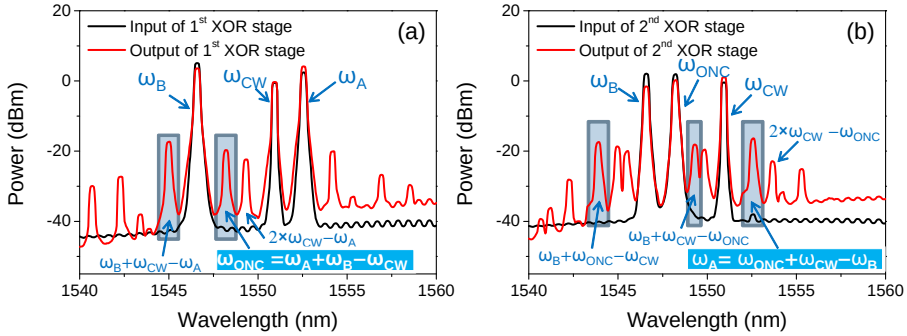

Figure 5.4: Four-wave mixing products generated in (a) the first XOR stage and (b) the second XOR stage.

filter (BPF), amplified and coupled into the second SOA together with a CW signal and Data B. In our experiment, the CW signal at the first XOR stage was reused as the CW beam for the second stage. As shown in Fig. 5.4(b), three of the generated FWM products carry the results of the XOR operation between the AONC and Data B, and thus carry the same phase information as the lost signal Data A. The possibility of selecting any of these three waves allows increasing the flexibility of the system, both in terms of filtering and wavelength allocation. This is demonstrated and analysed in Section 5.3.3. In this section, we selected the product at ω_A thus a fully recovered Data A.

In order to increase the conversion efficiency of both XOR stages, the waves at the input of the SOAs were aligned in polarisation and optimised in term of power levels. Bit-synchronisation is critical to successfully implement the logic operation. This was obtained by the use of optical delay lines. Furthermore, in order to retrieve the original data, pattern-synchronisation is also a requirement at the input of the second stage.

5.3.2 Demonstration and performance

First, the waveforms of the DPSK signals demodulated by a 1-bit Mach-Zehnder (MZ)-DI were checked following single-ended detection, as shown in Fig. 5.5. Data A and Data B were recorded right at the input of the SOA of the first stage. Both signals were phase modulated with a custom

designed pattern (not a classic shift register sequence) to allow recognition of the expected pattern resulting from XOR operation between Data A and B. All the bits of the first stage XOR output were compared to the calculated XOR patterns between Data A and Data B, taking the pattern delay into account. The resulting measured pattern was in full agreement with the expected pattern, as shown in Fig. 5.5 (c), in spite of the fact that the detected pattern was logically inverted, which depends on the phase control of the DI.

By monitoring the waveform at the input of the second stage, the pattern of the AONC signal and that of Data B were carefully synchronised. The pattern carried by the FWM product from the second stage is represented in Fig. 5.5 (d). It is clearly seen to exactly match Data A, fulfilling the expectations of network coding. Consequently, data protection would be achieved in case Data A is lost due to network failure.

The bit error rate (BER) measurements were then performed with conventional pseudo random bit sequence (PRBS) patterns, as shown in Fig. 5.6. The NRZ-DPSK signals before the XOR gates have a sensitivity of -38 dBm at a BER of 10^{-9} when balanced detection is employed. The performance difference between modulation with PRBS lengths of

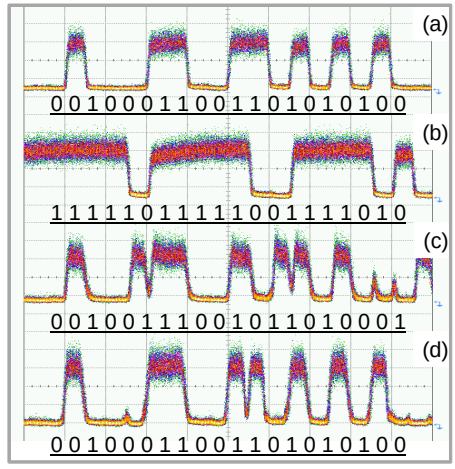

Figure 5.5: Single-ended detected bit patterns for 10 Gbit/s NRZ-DPSK signals: (a) Data A at SOA1 input, (b) Data B at SOA1 input, (c) AONC signal at SOA1 output and (d) recovered Data A at SOA2 output. All the waveforms were recorded with an horizontal scale of 200 ps/div.

$2^7 - 1$ and $2^{31} - 1$ is less than 0.2 dB.

After the first XOR stage, the signal was only degraded by less than 0.5 dB power penalty. The eye diagram after balanced detection is widely open at a received power of −35 dBm. After the second XOR stage, the successfully retrieved NRZ-DPSK signal has a sensitivity of −36.4 dBm with PRBS length of $2^7 - 1$. For the longer PRBS pattern of $2^{31} - 1$, the performance at lower received power is nearly the same as for $2^7 - 1$. The detected eye diagram also shows a very limited impact from pattern effects, which would normally be expected from processing in a SOA. In fact, if we compare the optical eye diagrams (Fig. 5.7), the pattern effect due to cross gain modulation (XGM) in a SOA is quite clear on the AONC output (Fig. 5.7(b)) from the first XOR stage. An overshoot appears after a power dip. For the second XOR stage, the overshoot on the AONC signal is in the reversed pattern compared to Data B, which compensated the pattern effect. It would lead to an optical eye with very little pattern effect at the second XOR stage output.

The power penalty due to the second XOR stage was slightly higher than for the first stage, resulting in a total power penalty of 1.7 dB for

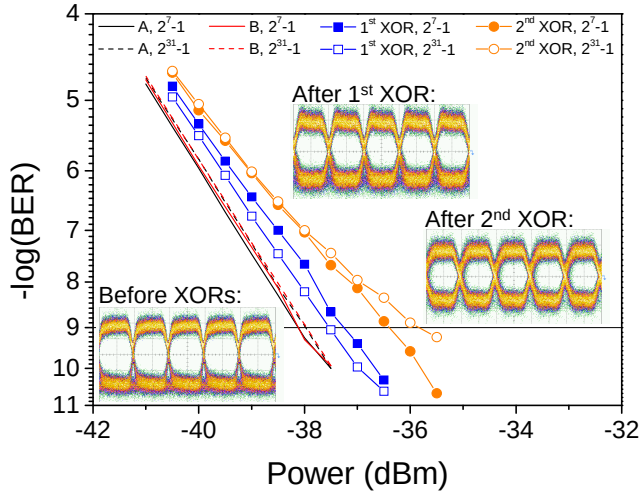

Figure 5.6: Bit-error rate measurements for all the signals and corresponding balanced detected eye-diagrams after the two XOR stages. The eye-diagrams were all recorded with received power of −35 dBm.

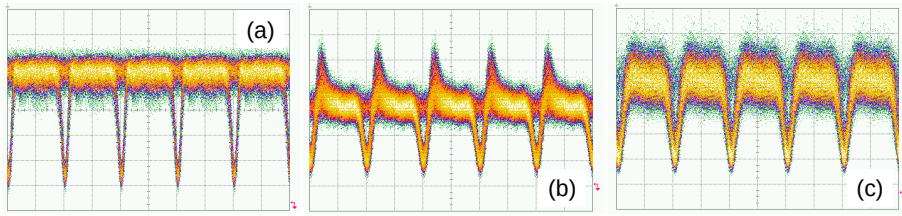

Figure 5.7: Optical eye-diagrams of (a) Back-to-back 10 Gbit/s NRZ-DPSK signal, (b) AONC signal and (c) Retrieved Data A signal

the entire network coding operation with a PRBS of $2^7 - 1$, and 2.1 dB with a PRBS of $2^{31} - 1$. The pattern length only resulted in a negligible power penalty of 0.4 dB.

We have experimentally demonstrated all-optical network coding operation for phase modulated signals using XOR gates based on four-wave mixing in SOAs. The scheme was successfully demonstrated with error-free performance at 10 Gbit/s with the NRZ-DPSK modulation format using two SOAs. The total operation power penalty is about 2 dB with negligible pattern effects.

As discussed in [22], the AONC should be able to apply to multiple inputs. For the demonstrated scheme, it is easy to implement for three inputs when replacing the CW by a data signal. To go beyond three inputs will require to cascade the XOR gates.

5.3.3 Multicasting feasibility of AONC signals

Thanks to the nature of FWM, more than one AONC signal are generated simultaneously standing on different wavelengths, and also more than one retrieved data will be generated by the process. This feature makes multicasting the AONC code and further forwarding the retrieved data possible.

In order to demonstrate the feasibility of multicasting the AONC signals, error-free performance needs to be evaluated for all the AONC signals. The idler generated from the first XOR stage, standing at 1544.92 nm, which was highlighted in Fig. 5.4(a) but not used as AONC in the previous section, was evaluated in this section. Fig. 5.8 shows the BER comparison of the two AONC codes at 1544.92 nm and 1548.36 nm, as well as the two input 10 Gbit/s DPSK signals. It is noticed that the

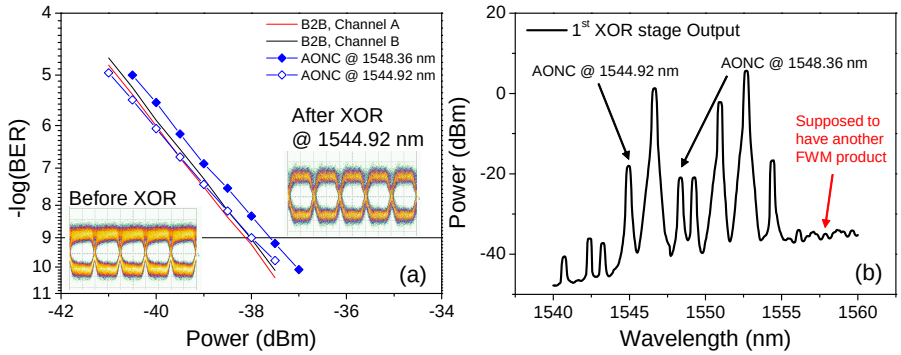

Figure 5.8: Performance of AONC signals: (a) Bit-error rate measurements comparing to the back-to-back signals and corresponding balanced detected eye-diagrams and (b) Spectra at the first XOR stage. The eye-diagrams were all recorded with received power of −35 dBm.

third AONC component generated on the longer wavelength side, which did appear, but had not been highlighted in Fig. 5.4(a), could not be observed as expected. It is due to the lower FWM conversion efficiency compared to previous measurements, which depends on polarisation, input power and also wavelength dependent nonlinear gain of the SOA. Therefore the weak signal was buried in the ASE noise and can not be seen.

As very little pattern effect was found in the previous section, the PRBS length used from now on is $2^{31}-1$. The back-to-back signals and the AONC signal at 1548.36 nm have the same BER performance as the results obtained in Section 5.3.2. The AONC signal at 1544.92 nm, i.e. on the shorter wavelength side, has a better performance compared to the one at 1548.36 nm and no receiver sensitivity penalty was noticed for this product. A very small receiver sensitivity difference, less than 0.5 dB, was noticed between the two AONC codes.

It was still assumed that the Data A was lost and therefore was retrieved by applying XOR operation between the AONC signal and the Data B. The three copies of Data A retrieved from the seconde XOR stage using these two AONC codes were evaluated. Fig. 5.9(a) pointed out the three generated retrieved Data A using the AONC at 1548.36 nm. The three idlers are at 1544.08 nm, 1549.28 nm and 1554.72 nm. The receiver sensitivity of the retrieved Data A at 1552.72 nm (the same idler

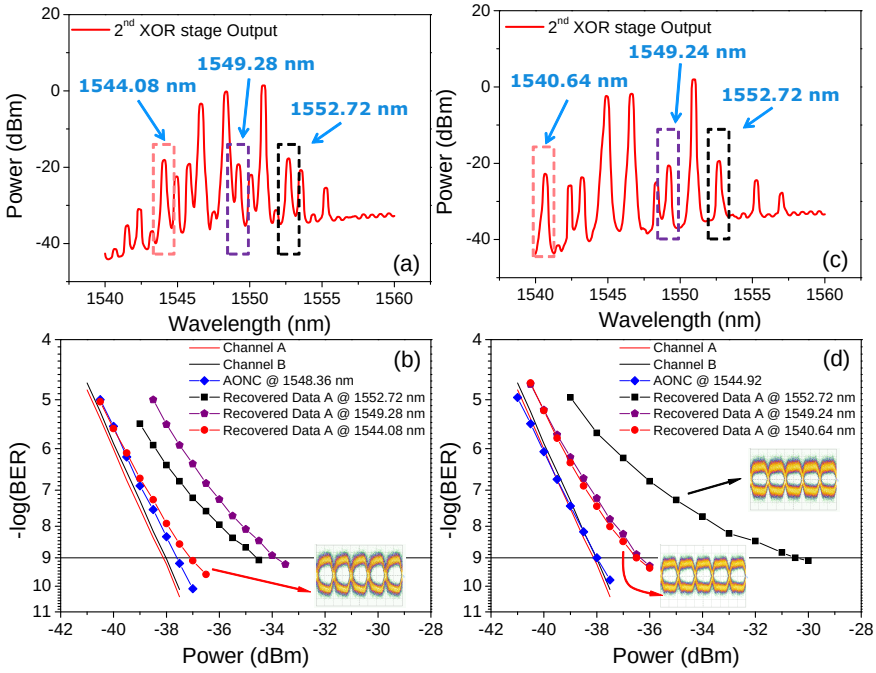

Figure 5.9: Bit-error rate measurements for all the signals and corresponding balanced detected eye-diagrams after the two XOR stages (a) Idler 1540 nm of the 1st stage and consequent idlers generated by the 2nd stage, (b) Idler 1540 nm of the 1st stage and consequent idlers generated by the 2nd stage

evaluated before) is measured to be −35.5 dBm, as shown in Fig. 5.9(b), 2 dB worse than what we have shown in Section 5.3.2. This performance difference is due to multiple reasons. First of all, a transmitter degradation was noticed. The electrical driving signal was found much more noisy than before, even though no BER performance difference was measured. The difference can be noticed when comparing the back-to-back eye diagram shown in Fig. 5.6 and the eye diagram in Fig. 5.8, both of which were recorded with the same signal power. Second is the difference in FWM conversion efficiency.

The retrieved Data A at 1544.08 nm, i.e. on the shorter wavelength side, shows a better sensitivity, −37 dBm, with only 1 dB total operation penalty compare to the back-to-back signal. The recovered Data A with the worst BER performance is the one standing at 1549.28 nm, which is

very close to the strong AONC signal input to the second stage SOA as illustrated in Fig. 5.9(a). Due to relatively low suppression of the strong AONC after filtering, its performance was hence degraded comparing to other products.

When using the AONC at 1544.92 nm as the input to the seconde XOR stage, another set of three recovered Data A at different wavelengths were generated. Fig. 5.9(b) shows the three generated idlers and Fig. 5.9(d) shows the BER performance of these three components comparing the back-to-back and the AONC code. A moderate (less than 2 dB) total operation penalty was measured for two of the three components at shorter wavelengths. The one at the longest wavelength of 1552.72 nm shows the worst performance, with a total penalty of about 7.5 dB and an error-floor starts to appear as well. Nevertheless, error-free performance of the retrieved data at different wavelengths is obtained and therefore it is possible to further distribute them to other destinations.

It can be noticed that all the shorter wavelength idlers generated in the same stage have a better sensitivity. This is related to the fact that the ASE gain peak of the SOAs used in our experiment is at 1560 nm. The idlers at shorter wavelengths will experience less ASE noise from the SOA, therefore will have a better OSNR and better performance.

In this section, multiple AONC signals and recovered data generated at different wavelengths have been evaluated. We have demonstrated the feasibility of multicasting the AONC code and also the data from recovered network coding operation. All the signals are with error-free performance and the network coding operation can be with as low as only 1 dB total penalty, if the retrieved data, at lower wavelength, is retrieved from the AONC signal at lower wavelength. Even for the worst case, 7.5 dB total operation penalty can be tolerated. In practical network, for example, as the protection is static and the performance difference is predictable, the low penalty case can be used for high-priority destinations and the high penalty signal for the low-priority destination.

5.4 Discussion

In the previous section, experimental demonstrations on all-optical network coding operation for DPSK signals using XOR gates based on non-degenerated FWM were presented. If instead of using the CW as in our experiment, a third phase modulated signal can be input to the XOR gates to perform XOR operation in a 3-inputs scenario. The AONC protection consequently can be expanded and adapted to more complicated networks.

As discussed in Section 5.2, if phase halving can be performed, degenerated FWM can then be used to perform the network coding for DPSK signals. In this section, the feasibility of phase halving is discussed. Furthermore, AONC should be applied to other advanced modulated formats. The feasibility of applying the AONC for mPSK signals is also discussed.

5.4.1 Phase halving

Phase modulation with $\frac{\pi}{2}$ can be obtained using $LiNbO_3$ phase modulators, by applying electrical signal with voltage within $[0, \frac{1}{2}V_\pi]$. The modulated signal will be with BPSK format. An optical method of halving the phase of BPSK and DPSK signals has so far never been discussed.

Fiber-based optical parametric amplifiers (OPAs) have been intensively studied for many years [118]. Parametric process refers to the process in which the medium parameter such as refractive index is modulated by the strong incident pump field [113]. Consider using a two-pump OPA, where one pump is phase modulated (e.g. DPSK) and the other one is a CW beam, a small signal, also CW beam, is placed in between of these two pumps and with exactly the same frequency spacing to each of them, as shown in Fig. 5.10. The signal could be amplified by the OPA and the photons transferred from the pumps to the signal have the phase relation $\phi = \frac{1}{2}(\phi_{\mathrm{DPSK}})$. If the transferred photons dominate, the signal would carry the phase which is half of the phase of the DPSK pump.

Simulations using 500 m HNLF show that it is possible to obtain a phase-halving. However the pump-signal relations, for example, power and wavelength spacing, appeared to be random and could not be un-

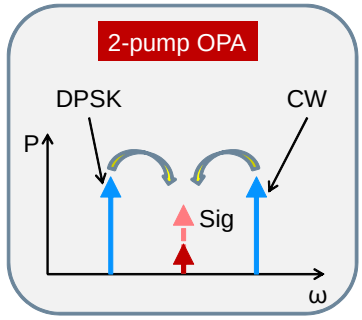

Figure 5.10: Principle of phase-halving operation using 2-pump OPA

derstood currently. It requires further understanding before it can be experimentally demonstrated.

5.4.2 All-optical network coding feasibility for mPSK signals

For phase modulation format, m-PSK is a more general term. The BPSK and DPSK are two-level PSK signals, i.e. $m = 2$. The quadrature phase shift keying (QPSK), also known as four-level PSK signal corresponds to $m = 4$. There can also be more formats, when m increases. In this section, QPSK is taken as an example to discuss the feasibility of applying the AONC operation over m-PSK signals.

The XOR gate using degenerated FWM for QPSK signal has been demonstrated using SOAs [119]. The two QPSK inputs, ω_{A} and ω_{B} will generate two idlers ω_{AB} and ω_{BA} at each side, as shown in in Fig. 5.11(a). The two QPSK input signals are with four phase levels, $(\frac{\pi}{4}, \frac{3\pi}{4}, \frac{-3\pi}{4}, \frac{-\pi}{4})$. Their constellation diagram is shown in Fig. 5.11(b).

It can be derived that the in-phase and quadrature tributaries of the two idlers have the relation with the two inputs as [119]:

$$\omega_{\mathrm{AB}} \Longrightarrow \begin{cases} I_{AB} = I_A \oplus Q_A \oplus Q_B \ , \\ Q_{AB} = I_A \oplus Q_A \oplus I_B \ , \end{cases} \tag{5.4}$$

$$\omega_{\mathrm{BA}} \Longrightarrow \begin{cases} I_{BA} = I_B \oplus Q_B \oplus Q_A \ , \\ Q_{BA} = I_B \oplus Q_B \oplus I_A \ . \end{cases} \tag{5.5}$$

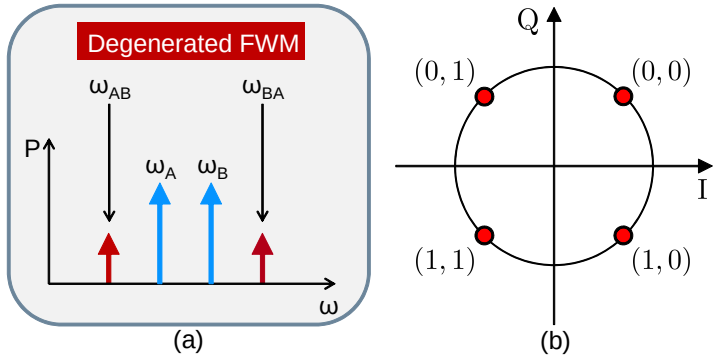

Figure 5.11: XOR gate for QPSK signals using degenerated FWM. (a) FWM spectrum and (b) constellation diagram of the input QPSK signals

Consider ω_{B} is lost, idlers ω_{L} and ω_{R} can be generated from the AONC code ω_{AB} and ω_{A} by a second degenerated FWM and they have the following relations:

$$\omega_{\mathrm{L}} \Longrightarrow \begin{cases} I_{(AB)A} = I_{AB} \oplus Q_{AB} \oplus Q_A \\ Q_{(AB)A} = I_{AB} \oplus Q_{AB} \oplus I_A \end{cases} \neq \omega_{\mathrm{B}} \ , \tag{5.6}$$

$$\omega_{\mathrm{R}} \Longrightarrow \begin{cases} I_{A(AB)} = I_A \oplus Q_A \oplus Q_{AB} = I_B \\ Q_{A(AB)} = I_A \oplus Q_A \oplus I_{AB} = Q_B \end{cases} = \omega_{\mathrm{B}} \ . \tag{5.7}$$

Clearly, the AONC scheme can recover the data but not with random wavelength relation between the AONC code and the received data. It is because, FWM no longer performs as XOR gate for phase modulated signals rather than BPSK or DPSK [120]. Network coding of two inputs with different modulation level, can also work with the same wavelength relation restriction.

5.4.3 Synchronisation

As mentioned in Section 5.1, an AONC scheme for OOK signals using polarisation multiplexing can avoid bit-synchronisation [96]. It was pointed out. The crucial problem with optical network coding in general. Our demonstrated scheme for phase modulated signals does require both pattern-synchronisation and bit-synchronisation. The loss of pattern-synchronisation will not achieve the data recovery, which is, in

general, true for any coding scheme. Bit-synchronisation will introduce penalty, as studied in [110].

5.5 Summary

In this chapter, an all-optical network protection scheme based on network coding was presented. The scheme was experimentally demonstrated for DPSK signals with 10 Gbit/s data modulation using two XOR gates based on non-degenerated FWM process. SOAs were used as the nonlinear media for demonstrating the scheme as low power operation can be achieved, which is of critical importance for network energy consumption and green network, even though the bit rate is limited by the speed of SOAs. Error-free operation for all-optical network coding was obtained and the total operation penalty can be as low as only 1 dB. Pattern effects were also evaluated by comparing the system performance with PRBS lengths of $2^7 - 1$ and $2^{31} - 1$. The different pattern length only resulted in a negligible BER performance difference of 0.4 dB. Thanks to the nature of FWM, multiple idlers carrying the same XOR information can be generated. We have evaluated all the generated idlers, both AONC signals and retrieved data and demonstrated the feasibility of multicasting the AONC signals and further distributing the retrieved data signal so that the network and its protection scheme becomes more flexible.

Using degenerated FWM to operate the XOR calculation in order to realise AONC requires phase-halving operation. An all-optical method to obtain the phase-halving was discussed. It was also discussed the possibility of applying the AONC operation for advanced modulation formats.

Chapter 6

Conclusion

This thesis has addressed some solutions for short-range and highly reliable optical networks.

6.1 Summary

Cost-effective transmitters for short-range networks

We proposed the use of a silicon micro-ring resonator (MRR) as an ultra-compact filter in a chirp managed laser (CML) transmitter in order to increase the modulation speed of its directly modulated laser (DML) for short-range applications. We have comprehensively analysed the modulation enhancement and the influence of the MRR design on the system performance. Compared to coupled ring MRRs, single ring MRRs are easier to fabricate and more robust against fabrication errors, therefore are more promising in practice.

A modulation speed enhancement from 10 Gbit/s to 40 Gbit/s has been demonstrated in a commercial distributed feed-back (DFB) laser. Both dispersion and detuning tolerances have been assessed. Error-free transmission of the generated 40 Gbit/s signal over 4.5-km standard single mode fibre (SSMF) was also demonstrated.

Error-free performance with direct modulation at 25 Gbit/s on a vertical-cavity surface-emitting laser (VCSEL) whose maximum 3-dB modulation bandwidth is 17.6 GHz was achieved, with a sensitivity of -21 dBm, while there is still room for improvement.

Thanks to the small size, the multi-channel processing capability and the integratability and the compatibility with complementary metal-oxide-semiconductor (CMOS) for massive production, of MRRs, they can be integrated with VCSELs. Therefore the proposed transmitter would be a compact and cost-effective solution for future short-range applications.

The cascadability of MRRs for applications like optical interconnet and network-on-chips was also experimentally assessed. Error-free performance was achieved for 5 cascaded MRRs used as drop filters, using a re-circulating loop. This was evaluated using both 40 Gbit/s carrier-suppressed return-to-zero on-off keying (CSRZ-OOK) and carrier-suppressed return-to-zero differential phase shift keying (CSRZ-DPSK) signals. The CSRZ-OOK signal showed a higher tolerance to bandwidth reduction due to cascading.

Wavelength tunable all-optical wavelength flip-flop operation in a single MG-Y laser

Wavelength-tunable all-optical wavelength flip-flop (AOWFF) operation in a single modulated grating Y-branch (MG-Y) laser structure has been experimentally demonstrated. Optically controlled dynamic bistable operation has been experimentally demonstrated on three wavelengths. More bistable regions are believed to be present in the MG-Y laser tuning range. The measured switching energy can be ultra low, 0.07 pJ, when the control pulse wavelength is close to the lasing side-mode and long control pulse width is ued. The measured switching time was about 200 ps.

Ultra-fast self-aware all-optical protection switching using a bistable laser

We proposed a novel concept on all-optical protection switching using a bistable laser. The link failure detection and the protection trigger were both implemented in the optical layer, avoiding the delay due to control mechanisms in higher layers. The concept was experimentally demonstrated using a wavelength tunable AOWFF based on a single MG-Y laser. The achieved protection switching time was less than 200 ps. The system was evaluated at both 10 Gbit/s and 40 Gbit/s. Good sig-

nal quality following successful establishment of the protection path are obtained.

All-optical network protection using network coding

An all-optical network protection scheme based on network coding was experimentally demonstrated for phase modulated signals using exclusive OR (XOR) logic gates realised by four-wave mixing (FWM) in semiconductor optical amplifiers (SOAs). The scheme was evaluated with 10 Gbit/s differential phase shift keying (DPSK) signals and error-free operation and multicasting feasibility were demonstrated. The total operation penalty was only 1 dB and very low (0.4 dB) pattern effects were noticed.

6.2 Future Work

The following gives a brief outlook and some suggestion for future works.

Design for cost-effective transmitters

Designing of a transmitter cost-effectively is the guideline and interesting for all applications. The future of cost-effective transmitter for short-range networks (e.g. passive optical network (PON) networks, optical interconnects, network-on-chips etc.) could be in the silicon photonics.

Here a few points for the future work, on the line of improving the design proposed in this thesis:

- Product verification of integrated CML transmitter based on VCSEL and MRR.
- Further improvement for the proposed cost-effective transmitter design. It would be interesting to combine the electrical pre-emphasis with the proposed method using MRR.

All-optical protection scheme

As the bandwidth of optical networks continuously grows, network protection, especially ultra-fast all-optical protection switching, will become

more and more important, not only for those networks with high reliability requirement, but also for terrestrial optical networks. More optical protection switching scheme should be identified.

All-optical signal processing and logic

As we can see throughout the project, all-optical signal processing and logic are important in nearly all area, especially for the future "optical" computer.

Within this thesis, the phase-halving operation proposed and discussed in Chapter 5, requires more understanding to verify its feasibility for operation. It would be interesting to look at other methods to perform the phase-halving operation.

List of Acronyms

AOFF	all-optical flip-flop
AOM	acousto-optic modulator
AONC	all-optical network coding
AOPS	all-optical protection switching
AOWFF	all-optical wavelength flip-flop
AM	amplitude modulation
ASE	amplified spontaneous emission
AWG	arrayed waveguide grating
BCB	benzocyclobutene
BER	bit error rate
BPF	band-pass filter
BPSK	binary phase shift keying
CDP	carrier density pulsation
CH	carrier heating
CML	chirp managed laser
CMOS	complementary metal-oxide-semiconductor
CROW	coupled-resonator optical waveguide

CSRZ-DPSK	carrier-suppressed return-to-zero differential phase shift keying
CSRZ-OOK	carrier-suppressed return-to-zero on-off keying
CW	continuous wave
DBR	distributed Bragg reflector
DCF	dispersion compensation fibre
DFB	distributed feed-back
DI	delay interferometer
DL	delay line
DML	directly modulated laser
DPSK	differential phase shift keying
EDFA	erbium doped fibre amplifier
EMC	electromagnetic compatibility
ER	extinction ratio
FEC	forward error correction
FM	frequency modulation
FSR	free spectral range
FWHM	full width at half maximum
FWM	four-wave mixing
FP	Fabry Pérot
GVD	group-velocity dispersion
HNLF	highly nonlinear fibre
ICP-RIE	inductively coupled plasma reactive ion etching

ISI	inter-symbol interference
LAN	local area network
MG-Y	modulated grating Y-branch
MMI	multi-mode interferometer
mPSK	multi-level phase shift keying
MZ	Mach-Zehnder
MZI	Mach-Zehnder interferometer
MZM	Mach-Zehnder modulator
MRR	micro-ring resonator
NRZ	non return-to-zero
NRZ-OOK	non return-to-zero differential on-off keying
OBPF	optical bandpass filter
OOK	on-off keying
OPA	optical parametric amplifier
OSNR	optical signal to noise ratio
OTDR	optical time-domain reflectometry
PC	polarisation controller
PON	passive optical network
PM	polarisation maintaining
PRBS	pseudo random bit sequence
QPSK	quadrature phase shift keying
RZ	return-to-zero
RZ-DPSK	return-to-zero differential phase shift keying

SBS	stimulated Brillouin scattering
SG-DBR	sampled grating distributed Bragg reflector
SHB	spectral-hole burning
SMF	single mode fibre
SOA	semiconductor optical amplifier
SOI	silicon-on-insulator
SSMF	standard single mode fibre
TFF	thin-film filter
VCSEL	vertical-cavity surface-emitting laser
VOA	variable optical attenuator
WDM	wavelength division multiplexing
XGM	cross gain modulation
XOR	exclusive OR

References

[1] A. Leon-Garcia and I. Widjaja. *Communication Networks: Fundamental Concepts and Key Architectures*. McGraw-Hill, Second edition, March 2006. ISBN 007-125709-8.

[2] `http://www.fp7daphne.eu/`.

[3] B. Jalali, M. Paniccia, and G. Reed. "Silicon photonics", *IEEE Microwave Magazine*, vol. 7, no. 3, pp. 58–68, June 2006. doi:10.1109/MMW.2006.1638290.

[4] S. Matsuo, S.-H. Jeong, T. Segawa, H. Okamoto, Y. Kawaguchi, Y. Kondo, H. Suzuki, and Y. Yoshikuni. "Digitally tunable ring laser using ladder filter and ring resonator", *IEEE Journal of Selected Topics in Quantum Electronics*, vol. 11, no. 5, pp. 924–930, September 2005. doi:10.1109/JSTQE.2005.853776.

[5] T. Segawa, S. Matsuo, T. Kakitsuka, T. Sato, Y. Kondo, and R. Takahashi. "Semiconductor double-ring-resonator-coupled tunable laser for wavelength routing", *IEEE Journal of Quantum Electronics*, vol. 45, no. 7, pp. 892–899, July 2009. doi:10.1109/JQE.2009.2013126.

[6] T. Matsumoto, A. Suzuki, M. Takahashi, S. Watanabe, S. Ishii, K. Suzuki, T. Kaneko, H. Yamazaki, and N. Sakuma. "Narrow spectral linewidth full band tunable laser based on waveguide ring resonators with low power consumption", in *Technical Digest Optical Fiber Communication Conference, OFC'10,* San Diego, California, U.S.A., pp. 1–3, March 2010.

[7] B. Little and S. Chu. "Microring resonators for very large scale integrated photonics", in *Technical Digest IEEE Lasers and Electro-Optics Society Annual Meeting, LEOS'99,* Orlando, Florida, U.S.A., vol. 2, pp. 487–488, November 1999. doi:10.1109/LEOS.1999.811811.

[8] H. Wassel, D. Dai, M. Tiwari, J. Valamehr, L. Theogarajan, J. Dionne, F. Chong, and T. Sherwood. "Opportunities and challenges of using plasmonic components in nanophotonic architectures", *IEEE Journal on Emerging and Selected Topics in Circuits and Systems*, vol. 2, no. 2, pp. 154–168, June 2012. doi:10.1109/JETCAS.2012.2193934.

[9] X. Tan, M. Yang, L. Zhang, Y. Jiang, and J. Yang. "A generic optical router design for photonic network-on-chips", *Journal of Lightwave Technology*, vol. 30, no. 3, pp. 368–376, February 2012. doi:10.1109/JLT.2011.2178019.

[10] Y. Li, L. Zhang, R. Beausoleil, and A. Willner. "Ring resonator induced data timing skew in on-chip WDM optical interconnects", in *Technical Digest Conference on Lasers and Electro-Optics, CLEO'08,* San Jose, California, U.S.A., pp. 1–2, May 2008.

[11] D. Siracusa, V. Linzalata, G. Maier, A. Pattavina, Y. Ye, and M. Chen. "Hybrid architecture for optical interconnection based on micro ring resonators", in *IEEE Global Telecommunications Conference (GLOBECOM'2011),* pp. 1–5, December 2011. doi:10.1109/GLOCOM.2011.6133632.

[12] I. Young, E. Mohammed, J. Liao, A. Kern, S. Palermo, B. Block, M. Reshotko, and P. Chang. "Optical I/O technology for tera-scale computing", *IEEE Journal of Solid-State Circuits*, vol. 45, no. 1, pp. 235–248, January 2010. doi:10.1109/JSSC.2009.2034444.

[13] S. Srinivasan, D. Liang, M. Fiorentino, R. Beausoleil, and J. Bowers. "Gain-assisted hybrid silicon microring electroabsorption modulators", in *IEEE 9th International Conference on Group IV Photonics, GFP'12,* pp. 99–101, August 2012. doi:10.1109/GROUP4.2012.6324099.

[14] S. Srinivasan, D. Liang, M. Fiorentino, R. Beausoleil, and J. Bowers. "Micro-ring resonator based electro-absorption modulators on the hybrid III-V on silicon platform", in *IEEE Optical Interconnects Conference, OIC'12,* Santa Fe, New Mexico, U.S.A., pp. 22–23, May 2012. doi:10.1109/OIC.2012.6224467.

[15] M. Song, L. Zhang, L. Zou, J.-Y. Yang, R. Beausoleil, and A. Willner. "A three-ring-resonator electro-optical switch with reduced jitter and enhanced speed and extinction ratio", in *Technical Digest IEEE Lasers and Electro-Optics Society Annual Meeting, LEOS'08,* Newport Beach, California, U.S.A., pp. 459 –460, November 2008. doi:10.1109/LEOS.2008.4688689.

[16] G. Nielson, D. Seneviratne, F. Lopez-Royo, P. Rakich, Y. Avrahami, M. Watts, H. Haus, H. Tuller, and G. Barbastathis. "Integrated wavelength-selective optical MEMS switching using ring resonator filters", *Journal of Lightwave Technology*, vol. 17, no. 6, pp. 1190–1192, June 2005. doi:10.1109/LPT.2005.846951.

[17] Y. Tanushi, M. Wake, K. Wakushima, K. Suzuki, and S. Yokoyama. "Technology for ring resonator switches using electro-optic materials", in *IEEE International Conference on Group IV Photonics, GFP'04,* pp. 22–24, September 2004. doi:10.1109/GROUP4.2004.1416640.

[18] R. Ramaswami, K. N. Sivarajan, and G. H. Sasaki. *Network Survivability*, In *Optical Networks: A Practical Perspective,* Chapter 9, pp. 511–572, Morgan Kaufmann, 2010. ISBN 978-0-12-374092-2.

[19] "ARINC Specification 664P7-1", 2009. Aircraft Data Network Part 7, Avionics Full-Duplex Switched Ethernet Network.

[20] R. Ahlswede, N. Cai, S.-Y. Li, and R. Yeung. "Network information flow", *IEEE Transactions on Information Theory*, vol. 46, no. 4, pp. 1204–1216, July 2000. doi:10.1109/18.850663.

[21] A. Kamal. "Using network coding over p-cycles for survivable network operation", in *International Symposium on High Capacity*

Optical Networks and Enabling Technologies, HONET'07., pp. 1–9, November 2007. doi:10.1109/HONET.2007.4600284.

[22] E. D. Manley, J. S. Deogun, L. Xu, and D. R. Alexander. "All-optical network coding", *Journal of Optical Communications and Networking*, vol. 2, no. 4, pp. 175–191, April 2010. doi:10.1364/JOCN.2.000175.

[23] W. Bogaerts, P. De Heyn, T. Van Vaerenbergh, K. DeVos, S. K. Selvaraja, T. Claes, P. Dumon, P. Bienstman, D. Van Thourhout, and R. Baets. "Silicon Microring Resonators", *Laser Photonics Review*, vol. 6, no. 1, pp. 47–73, January 2012. doi:10.1002/LPOR.201100017.

[24] D. G. Rabus. *Integrated Ring Resonators: The Compendium.* Springer, March 2007. ISBN 978-3-540-68788-7.

[25] A. Yariv and P. Yeh. *Photonics: Optical Electronics in Modern Communications.* Oxford University Press, 6th edition, 2007. ISBN 0-10-517946-3.

[26] J. H. Zhao and C. K. Madsen. *Optical Filter Design and Analysis: A Signal Procesing Approach.* Wiley, 1999. ISBN 0-471-18373-3.

[27] T. Shoji, T. Tsuchizawa, T. Watanabe, K. Yamada, and H. Morita. "Low loss mode size converter from 0.3 μm square Si wire waveguides to singlemode fibres", *Electronics Letters*, vol. 38, no. 25, pp. 1669–1670, December 2002. doi:10.1049/el:20021185.

[28] Y. Ding, J. Xu, C. Peucheret, M. Pu, L. Liu, J. Seoane, H. Ou, X. Zhang, and D. Huang. "Multi-channel 40 Gbit/s NRZ-DPSK demodulation using a single silicon microring resonator", *Journal of Lightwave Technology*, vol. 29, no. 5, pp. 677–684, March 2011. doi:10.1109/JLT.2010.2101049.

[29] A. Melloni, M. Martinelli, G. Cusmai, and R. Siano. "Experimental evaluation of ring resonator filters impact on the bit error rate in non return to zero transmission systems", *Optics Communication*, vol. 234, pp. 211–216, 2004. doi:10.1016/j.optcom.2004.02.045.

[30] B. G. Lee, B. A. Small, K. Bergman, Q. Xu, and M. Lipson. "Transmission of high-data-rate optical signals through a micrometer-scale silicon ring resonator", *Optics Letters*, vol. 31, no. 18, pp. 2701–2703, September 2006. doi:10.1364/OL.31.002701.

[31] L. Xu, J. Chan, A. Biberman, H. Lira, M. Lipson, and K. Bergman. "DPSK transmission through silicon microring switch for photonic interconnection networks", *IEEE Photonics Technology Letters*, vol. 23, no. 16, pp. 1103–1105, August 2011. doi:10.1109/LPT.2011.2147300.

[32] C. Ferrari, A. Canciamilla, F. Morichetti, M. Sorel, and A. Melloni. "Penalty-free transmission in a silicon coupled resonator optical waveguide over the full C-band", *Optics Letters*, vol. 36, no. 19, pp. 3948–3950, October 2011. doi:10.1364/OL.36.003948.

[33] K. Sato, S. Kuwahara, Y. Miyamoto, and N. Shimizu. "40 Gbit/s direct modulation of distributed feedback laser for very-short-reach optical links", *Electronics Letters*, vol. 38, no. 15, pp. 816–817, 2002.

[34] B. Huiszoon, R. J. W. Jonker, P. K. van Bennekom, G.-D. Khoe, and H. de Waardt. "Cost-effective up to 40 Gb/s transmission performance of 1310 nm directly modulated lasers for short- to medium-range distances", *Journal of Lightwave Technology*, vol. 23, no. 3, pp. 1116–1125, 2005.

[35] K. Sato, S. Kuwahara, and Y. Miyamoto. "Chirp characteristics of 40 Gb/s directly modulated distributed-feedback laser diodes", *Journal of Lightwave Technology*, vol. 23, no. 11, pp. 3790–3797, 2005.

[36] P. Westbergh, J. S. Gustavsson, B. Ko, A. Larsson, A. Mutig, A. Nadtochiy, D. Bimberg, and A. Joel. "40 Gbit/s error-free operation of oxide-confined 850 nm VCSEL", *Electronics Letters*, vol. 46, no. 14, pp. 1014–1016, 2010.

[37] W. Hofmann, P. Moser, P. Wolf, A. Mutig, M. Kroh, and D. Bimberg. "44 Gb/s VCSEL for optical interconnects", in *Technical Di-*

gest Optical Fiber Communication Conference, OFC'11, Los Angeles, California, U.S.A., Paper PDPC5, March 2011.

[38] Y. Matsui, D. Mahgerefteh, X. Zheng, C. Liao, Z. F. Fan, K. Mccallion, and P. Tayebati. "Chirp-managed directly modulated laser (CML)", *IEEE Photonics Technology Letters*, vol. 18, no. 2, pp. 385–387, 2006.

[39] D. Mahgerefteh, Y. Matsui, X. Zheng, and K. McCallion. "Chirp managed laser and applications", *IEEE Journal of Selected Topics in Quantum Electronics*, vol. 16, no. 5, pp. 1126–1139, 2010.

[40] J. Yu, Z. Jia, M.-F. Huang, M. Haris, P. Ji, T. Wang, and G.-K. Chang. "Applications of 40-Gb/s chirp-managed laser in access and metro networks", *Journal of Lightwave Technology*, vol. 27, no. 3, pp. 253–265, February 2009. doi:10.1109/JLT.2008.2006064.

[41] T. L. Koch and R. A. Linke. "Effect of nonlinear gain reduction on semiconductor laser wavelength chirping", *Applied Physics Letters*, vol. 48, no. 10, pp. 613–615, 1986.

[42] D. Mahgerefteh, Y. Matsui, C. Liao, B. Johnson, D. Walker, X. Zheng, Z. F. Fan, K. Mccallion, and P. Tayebati. "Error-free 250 km transmission in standard fibre using compact 10 Gbit/s chirp-managed directly modulated lasers (CML) at 1550 nm", *Electronics Letters*, vol. 41, no. 9, pp. 9–10, 2005.

[43] A. Siekiera, R. Engelbrecht, and B. Schmauss. "Fiber Bragg grating filter for spectral reshaping of directly modulated laser diode with 10 Gbit/s NRZ-OOK modulation format", in *OSA Technical Digest on Bragg Gratings, Photosensitivity, and Poling in Glass Waveguides,* Paper JThA32, 2010.

[44] L. Yan, Y. Wang, B. Zhang, C. Yu, J. McGeehan, and L. Paraschis. "Reach extension in 10-Gb/s directly modulated transmission systems using asymmetric and narrowband optical filtering", *Optics Express*, vol. 13, no. 13, pp. 5106–5115, 2005.

[45] C. S. Wong and H. K. Tsang. "Improvement of directly modulated diode-laser pulses using an optical delay interferometer", *IEEE Photonics Technology Letters*, vol. 16, no. 2, pp. 632–634, 2004.

[46] S. Chandrasekhar, A. Gnauck, L. Buhl, X. Zheng, D. Mahgerefteh, Y. Matsui, K. McCallion, Z. Fan, and P. Tayebati. "Single channel transmission over 9280 km at 10-Gb/s using small form factor chirp managed laser generating RZ AMI modulation format", in *Proceedings European Conference on Optical Communication, ECOC'05,* Glasgow, Scotland, Paper PD Th.4.2.5, September 2005.

[47] W. Jia and C.-K. Chan. "Generation of return-to-zero optical pulses using directly modulated chirp managed laser", *IEEE Photonics Technology Letters*, vol. 24, no. 14, pp. 1227–1229, 2012.

[48] L.-S. Yan, C. Yu, Y. Wang, T. Luo, L. Paraschis, Y. Shi, and A. Willner. "40-Gb/s transmission over 25 km of negative-dispersion fiber using asymmetric narrow-band filtering of a commercial directly modulated DFB laser", *IEEE Photonics Technology Letters*, vol. 17, no. 6, pp. 1322–1324, 2005.

[49] J. Yu, P. Ji, Z. Jia, T. Wang, X. Zheng, Y. Matsui, D. Mahgerefteh, K. McCallion, Z. Fan, and P. Tayebati. "42.8 Gbit/s chirp-managed signal transmission over 20km standard SMF at 1550nm without DCF", *Electronics Letters*, vol. 43, no. 23, August 2007. doi:10.1049/el:20072713.

[50] J. Yu, Z. Jia, P. N. Ji, and T. Wang. "40-Gb/s wavelength-division-multiplexing passive optical network with centralized lightwave source", in *Technical Digest Optical Fiber Communication Conference, OFC'08,* San Diego, California, U.S.A., Paper OTuH8, February 2008.

[51] Z. Al-Qazwini and H. Kim. "DC-balanced line coding for downlink modulation in bidirectional WDM PONs using remodulation", *IEEE Photonics Technology Letters*, vol. 23, no. 18, pp. 1331–1333, 2011.

[52] I.-S. Chung and J. Mørk. "Silicon-photonics light source realized by III-V/Si-grating-mirror laser", *Applied Physics Letters*, vol. 97, no. 15, 2010.

[53] I. Tomkos, D. Chowdhury, J. Conradi, D. Culverhouse, K. Ennser, C. Giroux, B. Hallock, T. Kennedy, A. Kruse, S. Kumar, N. Lascar, I. Roudas, M. Sharma, R. Vodhanel, and C.-C. Wang. "Demonstration of negative dispersion fibers for DWDM metropolitan area networks", *IEEE Journal of Selected Topics in Quantum Electronics*, vol. 7, no. 3, pp. 439–460, 2001.

[54] J. C. Cartledge and R. C. Srinivasan. "Extraction of DFB laser rate equation parameters for system simulation purposes", *Journal of Lightwave Technology*, vol. 15, no. 5, pp. 852–860, 1997.

[55] `http://www.ntt-electronics.com/en/products/photonics/pdf/NLK5C5EBKA.pdf`.

[56] Y. Ding, J. Xu, C. Peucheret, M. Pu, L. Liu, J. Seoane, and H. Ou. "Multi-channel 40 Gbit/s NRZ-DPSK demodulation using a single silicon microring resonator", *Journal of Lightwave Technology*, vol. 29, no. 5, pp. 677–684, 2011.

[57] W. Hofmann, M. Müller, P. Wölf, A. Mutig, T. Gründl, G. Böhm, D. Bimberg, and M.-C. Amann. "40 Gbit/s modulation of 1550 nm VCSEL", *Electronics Letters*, vol. 47, no. 4, 2011.

[58] `http://www.finisar.com/products/optical-instrumentation/WaveShaper-4000S`.

[59] Y. Tsunoda, M. Sugawara, H. Oku, S. Ide, and K. Tanaka. "25-Gb/s transmitter for optical interconnection with 10-Gb/s VCSEL using dual peak-tunable pre-emphasis", in *Technical Digest Optical Fiber Communication Conference, OFC'11,* Los Angeles, California, U.S.A., pp. 1 –3, March 2011.

[60] J. Zheng and H. T. Mouftah. *Optical Layer Survivability*, In *Optical WDM Networks: A Practical Perspective,* Chapter 6, pp. 165–210, Wiley-IEEE Press, August 2004. ISBN 978-0-471-67170-1.

[61] C.-S. Li and R. Ramaswami. "Automatic fault detection, isolation, and recovery in transparent all-optical networks", *Journal of Lightwave Technology*, vol. 15, no. 10, pp. 1784–1793, October 1997. doi:10.1109/50.633555.

[62] O. Gerstel and R. Ramaswami. "Optical layer survivability: an implementation perspective", *IEEE Journal on Selected Areas in Communications*, vol. 18, no. 10, pp. 1885–1899, October 2000. doi:10.1109/49.887910.

[63] "ITU-T Recommendation G.841", 1998. Available from `http://www.itu.int/rec/T-REC-G.841-199810-I/en`.

[64] S. Bjørnstad, M. Nord, and D. Hjelme. "Transparent optical protection switching scheme based on detection of polarisation fluctuations", in *Technical Digest Optical Fiber Communication Conference, OFC'02,* Anaheim, California, U.S.A., pp. 433–434, Paper ThG6, March 2002. doi:10.1109/OFC.2002.1036466.

[65] J. H. Lee, J.-H. Moon, K.-M. Choi, and C.-H. Lee. "Seamless maintenance and protection scheme for next-generation access networks", *IEEE Photonics Technology Letters*, vol. 21, no. 12, pp. 799–801, June 2009. doi:10.1109/LPT.2009.2018136.

[66] Z. Zalevsky and R. Appelman. "All-optical switching technologies for protection applications", *IEEE Communications Magazine*, vol. 42, no. 11, pp. S35–S40, November 2004. doi:10.1109/MCOM.2004.1362548.

[67] C. H. Yeh and C. W. Chow. "C+L band wavelength division multiplexing access network with distributed-controlled protection architecture", *Optical Engineering*, vol. 50, no. 12, pp. 125006–125006–4, 2011. doi:10.1117/1.3658759.

[68] K. Lee, J. H. Lee, Y.-G. Han, S. B. Lee, S.-G. Mun, S.-M. Lee, and C.-H. Lee. "A self-restorable colorless bidirectional WDM-PON based on ASE-injected FP-LDs", in *Technical Digest Optical Fiber Communication Conference, OFC'07,* Anaheim, California, U.S.A., pp. 1–3, March 2007. doi:10.1109/OFC.2007.4348796.

[69] A. Chowdhury, H.-C. Chien, S.-H. Fan, C. Liu, C. Su, and G.-K. Chang. "A survivable protection and restoration scheme using wavelength switching of integrated tunable optical transmitter for high throughput WDM-PON system", in *Technical Digest Optical*

Fiber Communication Conference, OFC'11, Los Angeles, California, U.S.A., pp. 1–3, March 2011.

[70] A. Bogoni, G. Berrettini, P. Ghelfi, A. Malacarne, G. Melon, L. Poti, and J. Wang. *All-Optical Flip-Flops Based on Semiconductor Technolgies*, In J. Grym, editor, *Semiconductor Technologies,* Chapter 15, pp. 347–372, In-Tech, March 2010. ISBN 978-953-307-080-3. Available from `http://www.intechopen.com/books/semiconductor-technologies`.

[71] K. Huybrechts, W. D'Oosterlinck, G. Morthier, and R. Baets. "Optical flip-flop operation using an AR-coated distributed feedback laser diode", in *Technical Digest Conference on Lasers and Electro-Optics, CLEO'07,* Baltimore, Maryland, U.S.A., pp. 1–2, May 2007. doi:10.1109/CLEO.2007.4453645.

[72] P. Wen, M. Sanchez, M. Gross, and S. Esener. "Observation of bistability in a vertical-cavity semiconductor optical amplifier (vc-soa)", *Optics Express*, vol. 10, no. 22, pp. 1273–1278, November 2002. doi:10.1364/OE.10.001273.

[73] M. Sedghi, H. Kaatuzian, and S. Khatami. "A novel all-optical flip-flop based on single-wavelength SOA-MZI", in *Photonics and Optoelectronics (SOPO), 2012 Symposium on,* pp. 1–4, may 2012. doi:10.1109/SOPO.2012.6271066.

[74] T. Katayama, T. Kitazawa, and H. Kawaguchi. "All-optical flip-flop operation using 1.55 μm polarization bistable VCSELs", in *Technical Digest Conference on Lasers and Electro-Optics, CLEO'08,* San Jose, California, U.S.A., pp. 1–2, May 2008.

[75] J. Sakaguchi, T. Katayama, and H. Kawaguchi. "High switching-speed operation of optical memory based on polarization bistable vertical-cavity surface-emitting laser", *IEEE Journal of Quantum Electronics*, vol. 46, no. 11, pp. 1526–1534, November 2010. doi:10.1109/JQE.2010.2052590.

[76] H. Dorren, D. Lenstra, Y. Liu, M. Hill, and G.-D. Khoe. "Nonlinear polarization rotation in semiconductor optical amplifiers:

theory and application to all-optical flip-flop memories", *IEEE Journal of Quantum Electronics*, vol. 39, no. 1, pp. 141–148, January 2003. doi:10.1109/JQE.2002.806200.

[77] A. Malacarne, J. Wang, Y. Zhang, A. Barman, G. Berrettini, L. Poti, and A. Bogoni. "20 ps transition time all-optical SOA-based flip-flop used for photonic 10 Gb/s switching operation without any bit loss", *IEEE Journal of Selected Topics in Quantum Electronics*, vol. 14, no. 3, pp. 808–815, May 2008. doi:10.1109/JSTQE.2008.918654.

[78] S. Matsuo, T. Kakitsuka, T. Segawa, and H. Suzuki. "Optical flip-flop operation using a DBR laser", in *Technical Digest Conference on Lasers and Electro-Optics, Pacific Rim, CLEO/Pacific Rim'07,* pp. 1–2, August 2007. doi:10.1109/CLEOPR.2007.4391221.

[79] K. Huybrechts, R. Baets, and G. Morthier. "All-optical flip-flop operation in a standard tunable DBR laser diode", *IEEE Photonics Technology Letters*, vol. 21, no. 24, pp. 1873–1875, December 2009. doi:10.1109/LPT.2009.2035169.

[80] M. Feng, S. Cundiff, R. Mirin, and K. Silverman. "Wavelength bistability and switching in two-section quantum-dot diode lasers", *IEEE Journal of Quantum Electronics*, vol. 46, no. 6, pp. 951–958, June 2010. doi:10.1109/JQE.2010.2041432.

[81] L. Liu, R. Kumar, K. Huybrechts, T. Spuesens, G. Roelkens, E.-J. Geluk, T. de Vries, P. Regreny, D. Thourhout, R. Baets, and G. Morthier. "An ultra-small, low-power, all-optical flip-flop memory on a silicon chip", *Nature Photonics*, vol. 4, pp. 182–187, January 2010. doi:10.1038/nphoton.2009.268.

[82] H. Dorren, M. Hill, Y. Liu, N. Calabretta, A. Srivatsa, F. Huijskens, H. de Waardt, and G. Khoe. "Optical packet switching and buffering by using all-optical signal processing methods", *Journal of Lightwave Technology*, vol. 21, no. 1, pp. 2–12, January 2003. doi:10.1109/JLT.2002.803062.

[83] T. Kakitsuka, S. Matsuo, K. Hamamoto, T. Segawa, H. Suzuki, and R. Takahashi. "Injection-locked flip-flop operation of a DBR laser", *IEEE Photonics Technology Letters*, vol. 23, no. 17, pp. 1261–1263, September 2011. doi:10.1109/LPT.2011.2159302.

[84] L. A. Coldren and S. W. Corzine. *Diode Aasers and Photonic Integrated Circuits.* Wiley, 1995. ISBN 0-471-11875-3.

[85] C. L. Tang, A. Schremer, and T. Fujita. "Bistability in two-mode semiconductor lasers via gain saturation", *Appl. Phys. Lett.*, vol. 51, no. 18, pp. 1392–1394, 1987. doi:10.1063/1.98686.

[86] A. Bogatov, P. Eliseev, and B. Sverdlov. "Anomalous interaction of spectral modes in a semiconductor laser", *IEEE Journal of Quantum Electronics*, vol. 11, no. 7, pp. 510–515, July 1975. doi:10.1109/JQE.1975.1068658.

[87] J.-O. Wesstrom, S. Hammerfeldt, J. Buus, R. Siljan, R. Laroy, and H. de Vries. "Design of a widely tunable modulated grating Y-branch laser using the additive Vernier effect for improved super-mode selection", in *Semiconductor Laser Conference, 2002. IEEE 18th International,* pp. 99–100, Paper TuP16, 2002. doi:10.1109/ISLC.2002.1041137.

[88] Based on private conversion with Prof. G. Morthier.

[89] J.-O. Wesstrom, G. Sarlet, S. Hammerfeldt, L. Lundqvist, P. Szabo, and P.-J. Rigole. "State-of-the-art performance of widely tunable modulated grating Y-branch lasers", in *Technical Digest Optical Fiber Communication Conference, OFC'04,* Los Angeles, California, U.S.A., vol. 1, p. 389, February 2004.

[90] A. Malacarne, J. Wang, Y. Zhang, A. Barman, G. Berrettini, L. Poti, and A. Bogoni. "20 ps transition time all-optical SOA-based flip-flop used for photonic 10 Gb/s switching operation without any bit loss", *IEEE Journal of Selected Topics in Quantum Electronics*, vol. 14, no. 3, pp. 808–815, May 2008. doi:10.1109/JSTQE.2008.918654.

[91] S. Lee, A. Chen, and P.-K. Tseng. "Optimal routing and bandwidth provisioning for survivable IPTV multicasting using network coding", in *IEEE Consumer Communications and Networking Conference, CCNC'11,* pp. 771–775, January 2011. doi:10.1109/CCNC.2011.5766596.

[92] R. Rout, S. Ghosh, and S. Chakrabarti. "Co-operative routing for wireless sensor networks using network coding", *Wireless Sensor Systems, IET*, vol. 2, no. 2, pp. 75–85, June 2012. doi:10.1049/iet-wss.2011.0069.

[93] S. Y. Chang and H.-C. Wu. "Statistical analysis for large-scale hierarchical networks using network coding", *IEEE Transactions on Vehicular Technology*, vol. 60, no. 5, pp. 2152–2163, June 2011. doi:10.1109/TVT.2011.2138175.

[94] F. Awad, O. Banimelhem, and N. Al-Rousan. "The potential of using network coding with geographical forwarding routing for wireless multimedia sensor networks", in *IEEE 11th International Conference on Computer and Information Technology, CIT'11,* pp. 9–14, September 2011. doi:10.1109/CIT.2011.71.

[95] T. Kono, A. Maruta, and K. Kitayama. "Input wavelength dependency of all-optical XOR gate using SOA-MZI wavelength converter for all-optical network coding", in *17th Microopics Conference, MOC'11,* pp. 1–2, November 2011.

[96] Z. Liu, M. Li, L. Lu, C.-K. Chan, S.-C. Liew, and L.-K. Chen. "Optical physical-layer network coding", *IEEE Photonics Technology Letters*, vol. 24, no. 16, pp. 1424–1427, August 2012. doi:10.1109/LPT.2012.2204972.

[97] J. M. Martinez, Y. Liu, R. Clavero, A. Koonen, J. Herrera, F. Ramos, H. Dorren, and J. Marti. "All-optical processing based on a logic XOR gate and a flip-flop memory for packet-switched networks", *IEEE Photonics Technology Letters*, vol. 19, no. 17, pp. 1316–1318, September 2007. doi:10.1109/LPT.2007.902378.

[98] E. Kuzin, J. Sancher-Mondragon, V. Vyslouch, J. Andrade-Lucio, and R. Rojas-Laguna. "Regeneration of optical signals by fiber

logic elements operating through stimulated Raman scattering", in *Technical Digest Optical Fiber Communication Conference, OFC'96,* San Jose, California, U.S.A., pp. 153–154, February 1996. doi:10.1109/OFC.1996.907722.

[99] S. Hamilton and B. Robinson. "40-Gb/s all-optical packet synchronization and address comparison for OTDM networks", *IEEE Photonics Technology Letters*, vol. 14, no. 2, pp. 209–211, February 2002. doi:10.1109/68.980524.

[100] Y. An, F. Da Ros, and C. Peucheret. "All-optical network coding for DPSK signals", in *Technical Digest Optical Fiber Communication Conference, OFC'13,* Anaheim, California, U.S.A., Paper JW2A.60, March 2013.

[101] Z. Wang, Y.-K. Huang, Y. Deng, J. Chang, and P. Prucnal. "Optical encryption with OCDMA code swapping using all-optical XOR logic gate", *IEEE Photonics Technology Letters*, vol. 21, no. 7, pp. 411–413, April 2009. doi:10.1109/LPT.2008.2012131.

[102] M. Nielsen, T. Fjelde, J. Buron, and B. Dagens. "All-optical bit-pattern recognition in data segments using logic AND and XOR in a single all-active MZI wavelength converter", in *Proceedings European Conference on Optical Communication, ECOC'02,* Copenhagen, Denmark, vol. 1, pp. 1–2, September 2002.

[103] M. Nielsen, J. Mork, T. Fjelde, and B. Dagens. "Numerical analysis of an all-optical logic XOR gate based on an active MZ interferometer", in *Technical Digest Conference on Lasers and Electro-Optics, CLEO'02,* Long Beach, California, U.S.A., vol. 1, pp. 608–609, May 2002. doi:10.1109/CLEO.2002.1034382.

[104] R. Manning, S. Ibrahim, R. Webb, Y. An, A. Poustie, G. Maxwell, S. Lardenois, and R. Harmon. "Fully integrated 42.6 Gb/s all-optical XOR gate", in *Photonics in Switching, 2009. PS'09. International Conference on,* pp. 1–2, September 2009. doi:10.1109/PS.2009.5307768.

[105] J. Dailey, S. Ibrahim, R. Manning, R. Webb, S. Lardenois, G. Maxwell, and A. Poustie. "42.6 Gbit/s fully integrated all-

optical XOR gate", *Electronics Letters*, vol. 45, no. 20, pp. 1047–1049, September 2009. doi:10.1049/el.2009.2036.

[106] H. Sun, W. Qiang, D. Hao, C. Zhe, N. Dutta, J. Jaques, and A. Piccirilli. "All-optical logic XOR gate at 80 Gb/s using SOA-MZI-DI", *IEEE Journal of Quantum Electronics*, vol. 42, no. 8, pp. 747–751, August 2006. doi:10.1109/JQE.2006.878184.

[107] R. Webb, X. Yang, R. Manning, and R. Giller. "All-optical 40 Gbit/s XOR gate with dual ultrafast nonlinear interferometer", *Electronics Letters*, vol. 41, no. 25, pp. 1396–1397, December 2005. doi:10.1049/el:20052982.

[108] X. Yang, R. Manning, and W. Hu. "Simple 40 Gbit/s all-optical XOR gate", *Electronics Letters*, vol. 46, no. 3, pp. 229–230, April 2010. doi:10.1049/el.2010.3039.

[109] K. Chan, C.-K. Chan, L. Chen, and F. Tong. "Demonstration of 20-Gb/s all-optical XOR gate by four-wave mixing in semiconductor optical amplifier with RZ-DPSK modulated inputs", *IEEE Photonics Technology Letters*, vol. 16, no. 3, pp. 897–899, March 2004. doi:10.1109/LPT.2004.823750.

[110] N. Deng, K. Chan, C.-K. Chan, and L.-K. Chen. "An all-optical XOR logic gate for high-speed RZ-DPSK signals by FWM in semiconductor optical amplifier", *IEEE Journal of Selected Topics in Quantum Electronics*, vol. 12, no. 4, pp. 702–707, July 2006. doi:10.1109/JSTQE.2006.876603.

[111] F. Li, T. D. Vo, C. Husko, M. Pelusi, D.-X. Xu, A. Densmore, R. Ma, S. Janz, B. J. Eggleton, and D. J. Moss. "All-optical XOR logic gate for 40 Gb/s DPSK signals via FWM in a silicon nanowire", *Optics Express*, vol. 19, no. 21, pp. 20364–20371, October 2011. doi:10.1364/OE.19.020364.

[112] G. P. Agrawal. *Fiber-optic communication systems*. Wiley, Second edition, 1997. ISBN 0-471-17540-4.

[113] P. Butcher and D. Cotter. *The elements of nonlinear optics*. Cambridge University Press, 1990. ISBN 0-521-42424-0.

[114] S. Diez, C. Schmidt, R. Ludwig, H. Weber, K. Obermann, S. Kindt, I. Koltchanov, and K. Petermann. "Four-wave mixing in semiconductor optical amplifiers for frequency conversion and fast optical switching", *IEEE Journal of Selected Topics in Quantum Electronics*, vol. 3, no. 5, pp. 1131–1145, October 1997. doi:10.1109/2944.658587.

[115] M. Takahashi, J. Hiroishi, M. Tadakuma, and T. Yagi. "Improvement of FWM conversion efficiency by SBS-suppressed highly nonlinear dispersion-decreasing fiber with a strain distribution", in *Proceedings European Conference on Optical Communication, ECOC'08,* Burssels, Belgium, pp. 1–2, September 2008. doi:10.1109/ECOC.2008.4729208.

[116] P. Winzer and R.-J. Essiambre. "Advanced optical modulation formats", *Proceedings of the IEEE*, vol. 94, no. 5, pp. 952–985, May 2006. doi:10.1109/JPROC.2006.873438.

[117] `http://www.ciphotonics.com/`.

[118] J. Hansryd, P. Andrekson, M. Westlund, J. Li, and P.-O. Hedekvist. "Fiber-based optical parametric amplifiers and their applications", *IEEE Journal of Selected Topics in Quantum Electronics*, vol. 8, no. 3, pp. 506–520, May 2002. doi:10.1109/JSTQE.2002.1016354.

[119] D. Kong, Y. Li, H. Wang, X. Zhang, J. Zhang, J. Wu, and J. Lin. "All-optical XOR gates for QPSK signals based on four-wave mixing in a semiconductor optical amplifier", *IEEE Photonics Technology Letters*, vol. 24, no. 12, pp. 988–990, June 2012. doi:10.1109/LPT.2012.2191771.

[120] J. Wang, S. R. Nuccio, J.-Y. Yang, X. Wu, A. Bogoni, and A. E. Willner. "High-speed addition/subtraction/complement/doubling of quaternary numbers using optical nonlinearities and DQPSK signals", *Optics Letters*, vol. 37, no. 7, pp. 1139–1141, April 2012. doi:10.1364/OL.37.001139.